NASA Technical Memorandum 86403

DESIGN CONSIDERATIONS FOR HIGH-ALTITUDE, LONG-ENDURANCE, MICROWAVE-POWERED AIRCRAFT

HAI QUA NGUYEN

APRIL 1985

National Aeronautics and Space Administration

Langley Research Center
Hampton, Virginia 23665

SUMMARY

The sizing and performance analyses have been conducted in the design of long-endurance, high-altitude airplanes. These airplanes receive power either continuously beamed from a phased array transmitter or intermittently beamed from a dish transmitter.

Results are presented for the cases of flight in zero wind speed and nonzero wind speed. Sensitivity studies indicate that the vehicle size was relatively insensitive to changes in the transmitter size. The cost estimates were made using models that excluded the airplane cost. Using a reference payload, results obtained from array and dish configurations were compared. Comparisons showed savings in cost as well as smaller vehicle sizes when an array transmitter was used.

TABLE OF CONTENTS

SYMBOLS

a	antenna unit cost
A_t	area of transmitter
Ag	chemical symbol of Silver
AR	aspect ratio
b	number of hours in life cycle
c	unit cost of electrical energy
C_D	total drag coefficient
C_{D_o}	profile drag coefficient
C_L	total lift coefficient
Cd	chemical symbol of Cadmium
d	slope of the curve of ground track offset angle versus altitude
D	drag force
D_t	diameter of transmitter
D_t^*	optimum diameter of transmitter
d_{max}	maximum radial distance
e	Oswald efficiency factor
E	electric field
E_r	resultant electric field
F	percent of the wing covered by rectenna elements
F_{rd}	percent of redundant rectenna elements
F_{st}	percent of available power dedicated to storage
G_1	antenna gain
G_2	rectenna gain

GHz	units of frequency (in 10^9 cycles per second)
g	gravity acceleration constant
h	altitude of airplane
H	magnetic field
H_2	chemical symbol of Hydrogen
L/D	the lift-drag ratio
m	cost of generating equipment per KW of power
Ni	chemical symbol of Nickel
P	power
ROC	rate of climb
R_o	zero-wind turn radius of vehicle
S_{wing}	the wing area
T	battery endurance
t_g	glide time
V	speed
W/S_{wing}	wing loading
W	aircraft weight
WFT	structural weight fraction
W_1	combined weight of payload, battery, propulsion, power-control devices
(x,y)	ground coordinates of vehicle positions
(x_o,y_o)	ground coordinates of initial vehicle position
Zn	chemical symbol of Zinc
α	the y-intercept of the curve of altitude versus wind speed
γ	flight path angle

θ_o	beam deflection angle
λ	wavelength
ϕ	aircraft roll angle
ψ	angle between vehicle air speed and wind speed
Φ	angle between vehicle air speed and ground track
ρ	density of air
ρ_o	sea-level density of air
π	constant Pi
σ	ratio of densities
ω	angular speed
μ	angle the wind direction makes with the ground track
ψ^*	value of angle ψ at which the radial distance is maximum
η_l	conversion efficiency
η_{prop}	propulsive efficiency
η_{rect}	rectenna efficiency
η	illumination efficiency

CHAPTER 1

INTRODUCTION

Technical advances made in recent years have made it feasible to expand the endurance limit of High-Altitude Powered Platforms (HAPPs). These platforms may achieve almost unlimited endurance by using power from either the sun's radiation or the microwave beams generated by a station located on the ground as the power supply. Communications-relay and observation are examples of proposed missions for HAPPs.

The HAPP system presents several unique advantages over existing aircraft and artificial satellites. A nominal 70,000-foot altitude of operation (ref. 1) gives the prospective users a maximum coverage diameter of more than 600 miles. While the area covered by the HAPPs is limited compared to Geosynchronous or Low-Earth-Orbit Satellites, the ground resolution provided by HAPPs is at least ten times better than even Low-Earth-Orbit Satellites can provide. The frequency of coverage is another consideration. The orbits designed for greater frequency of coverage of certain locations on the Earth's surface necessitate omissions of coverage of other points. The frequency of coverage depends on the intended purpose of the vehicle or satellite. HAPPs have greater coverage frequency if one should decide to make use of it. The very need to provide high-coverage frequency often exceeds the endurance limit of human pilots. Human endurance limit aside, the amount of fuel

carried by a conventionally manned aircraft dictates its endurance. By contrast, system reliability restricts the endurance of remotely powered HAPPs.

One of the first attempts at providing a long-endurance, high-altitude platform was associated with lighter-than-air vehicles. The Naval Electronics Systems Command initiated this effort in 1973. The program objective included design and fabrication of four basic vehicles (ref. 2). These vehicles were designed for flight durations from 30 hours to 30 days, depending on the primary power supplies. Figure 1 illustrates the configuration of an aerodynamically efficient, buoyant body as envisioned by the High-Altitude Superpressured Powered Aerostat (HASPA) Program. Wessel and Petrone expected the performance of the vehicles to be diminished by high wind speeds and inaccurate drag estimates compared to the design values.

The HAPP designs during the 1970's were not limited to lighter-than-air vehicles. Project "SUNRISE" (ref. 3) produced the world's first sun-powered aircraft. These aircraft weighed a little more than 20 pounds and were powered by an electric motor driving a propeller with electricity drawn from solar arrays mounted to upper-wing surfaces. The vehicle was to climb to a high altitude during daytime hours, start to glide during night hours, and remain above cloud cover as daylight hours approached. While SUNRISE demonstrated the feasiblity of solar-powered flight for limited duration, human-sized payload was also flown by Paul MacCready's Solar Challenger (ref. 4). This vehicle combined the light-weight electric motor-propeller system with lightweight structure.

Reference 5 presented another HAPP conceptually designed for long endurance. According to this report, in order to achieve mission requirements, such solar-powered vehicles must have large wing area and span. The authors predicted the availability of a solar HAPP by the early 1990's.

The 1970's also saw chemically-fueled, remotely piloted versions of HAPP designed for the United States Air Force. The "Compass Dwell" Program produced two aircraft, one with a single-piston engine, the other with a gas-turbine engine (ref. 6). An endurance level of about 28 hours was obtained. Before being cancelled in 1977, the "Compass Cope" Program produced some prototypes that were capable of flying at 70,000 feet on missions requiring endurances of up to 30 hours. These prototypes also took off and landed using normal runways constructed for conventional airplanes. Reference 6 states that one of the reasons for cancelling the "Compass Dwell" was that its proposed operational altitude was also being used by passenger airliners. "Compass Cope" was terminated for reasons that were not related to its performance.

A more recent, analytical study evaluated the performance of a remotely piloted, turboprop airplane powered by chemical or cryogenic fuels (ref. 7). The report concluded that maximum endurance based on wind constraints (about 70 hours) was almost the same for all candidate fuels considered for the 3000-pound vehicle. The report also showed that endurance limit was affected the most by changes in structural weight.

The microwave-powered HAPP provided the opportunity to remove the endurance restriction on chemically-fueled HAPPs. As opposed to solar-powered HAPPs, there would be no altitude loss during the night because the vehicle itself would continue to receive power from a ground station. Sufficient thrust could be generated by microwave-powered HAPPs to counter wind that decreased performance of lighter-than-air vehicles as stated earlier. Microwave-powered vehicles would be confined to operate within range of a ground station.

In all microwave-powered concepts, a ground station converts 60-cycle power into microwave power. The microwave beam is focused at a "rectenna" (combination rectifier and antenna) built into the vehicle. The intercepted microwave power would be rectified to on-board electrical power.

The National Aeronautics and Space Administration (NASA) has been assessing the capabilities of microwave-powered HAPPs since the late 1970's. In one of the studies funded by NASA Headquarters, James Sinko (ref. 8) identified two feasible HAPP concepts: blimp and airplane (fig 2). Sinko stated that the blimp concept would be at a disadvantage in high winds (being blown out of range of the ground station). The airplane concept was capable of attaining the altitudes and speeds beyond those of the blimp but offered less surface area for mounting the rectenna. The transmitting antenna could be one of two different types: parabolic dish or phased array.

The studies of references 9 and 10 addressed a "boost-glide" mode of flight for microwave-powered HAPP. Using such a mode, the airplane

would climb while receiving transmitted power, then glide to reach the next power station to intercept another microwave power beam to climb again. This ooost-glide flight path was seen as simplifying the designs of the transmitter antenna, since that antenna would be required to track only in a plane containing the flight path. A boost-gliae flight path also takes advantage of the airplane's forward speed to extend the area of coverage. The performance of a microwave-powered, boost-glide airplane was further studied in reference 10. Study results showed that decreased wing loading and increased lift coefficient, two ways to increase performance, were both limited by wind effects.

Graves (ref. 11) conducted a feasibility study into different HAPP concepts (nuclear, solar, and microwave) and found no feasible solar-powered airplane configuration. However, nuclear-powered or microwave-powered aircraft and conventionally shaped, microwave-powered blimps were feasible using technologies expected to be developed within the next 5 years. Both the airplane and the blimp were designed to carry a 100-pound payload.

Limits on feasibility as well as design guidelines for microwave-powered aircraft were presented in reference 12. Sizing results were obtained for airplanes designed to fly in zero-wind conditions, using circular flight paths. This study also linked aircraft design parameters to system performance but did not consider system costs.

While providing design guidelines and methods, references 9-12 did not provide a systemmatic way to estimate costs of future designs. Also

lacking was a vehicle-sizing analysis that accounted for a nonzero-wind environment and vehicle flight mechanics.

This study of a high-altitude, long-endurance, unmanned airplane, powered by microwave beams, has three objectives: First, it will describe by analytical expressions the relationship between the aircraft design parameters and the power source to minimize vehicle size. Secondly, the study will investigate the wind effects on zero-wind solutions (offered by the initial study phase). Third, the study will provide a means of estimating the annual cost of the ground station based on mission requirements.

CHAPTER 2

MICROWAVE POWER TRANSMISSION

Power transmission by microwave beam through free space combines several unique technologies. In this chapter, the components of the transmission systems are briefly described. Specific system performances such as tracking accuracy, cost, and transmission efficiency will also be discussed.

2.1 Free-Space Power Transmission

Free-space power transmission is defined as the point-to-point transfer of energy through free space by a microwave beam (ref. 13). Free space, however, is defined to include all the natural elements of the environment such as gases and liquids, excluding the presence of any solid objects like reflectors between the transmitting and receiving points. The primary motive to explore this transmission system is obvious when the proposed vehicles are to be powered by microwave energy in an efficient manner.

Historically, Tesla first explored the concept of power transmission by radio waves around the early 1900's (ref. 13). It was not until the early 1960's that the advent of highly efficient tubes (called "amplitron" or "klystron" tubes) permitted the transmission of large amounts of power (several hundred kilowatts). Conventional wires are

not practical for carrying microwaves because the microwaves radiate too much energy into space as they travel along the wires. The amount of radiated energy increases with frequency, and the frequency of microwaves is so high that all of the energy is lost from the wires very rapidly. It has been discovered that a "waveguide" is analogous to a very efficient form of transmission line for microwaves. A waveguide can be either a rectangular or circular hollow tube. Every study conducted to date has used 2.45 GHz as the frequency of transmission. The corresponding wavelength is about 0.12 cm. This frequency is at the center of a frequency band reserved exclusively for noncommunication purposes (ref. 11) such as microwave ovens. It is also a good choice considering the attenuation in power transmission caused by atmospheric conditions such as rainfall. Reference 14 presented the theoretical attenuations caused by cloud, rain, and thunderstorm. There is virtually no effect up to 3-GHz frequency. By increasing the frequency of transmission, one reduces the wavelength and decreases the size of the antenna. The beneficial effects of increased frequency of transmission (reduced size, hence cost of transmitter) must therefore be balanced against atmospheric attenuation factors.

2.2 Microwave Power Transmission System

W. Brown (ref. 13) divided the microwave-power transmission into three subsystems (fig. 3): power conversion, power transmission, and power reception.

2.2.1 Power Conversion: The conversion of electrical power into microwave power is done regularly by broadcasting stations and common

household ovens. A device (ref. 13) transforming direct-current power into microwave power is called a "magnetron" in its microwave oven configuration or an "amplitron" in oscillator form (fig. 4). This device offers high efficiency by virtue of its high-speed, low-mass rotor. High efficiency is particularly desirable since it is responsible for minimizing heat dissipation problems or minimizing the size of the prime power source. The magnetron output is then radiated by a combination of waveguide and radiating module. A large number of these modules can be combined in a planar fashion to construct the desired geometry of an array antenna for a ground station.

Figure 5 shows a sketch of the front view of the individual module with slots and the circular array composed of all modules being arranged in a horizontal plane. In reference 13, Brown evaluated several methods of distributing the phase and amplitude of the microwave beam. He concluded that active phased array was the best way.

Another method of channeling the output of the magnetron is one that employs a paraboloidal reflector. A "source" of microwave energy (magnetron's output) is placed at the focal point of the reflector, creating parallel wavefronts (fig. 6). This is typical of many radar dish configurations.

2.2.2 Power Transmission: The power transmission link guides the microwave energy from the output of the generator to the receiving point. It is very important here to consider the attenuation factors affecting the amount of radiated power. Goubau (ref. 15) presented a theoretical relationship between the transmission efficiency and the

aperture areas of both the receiving and transmitting antenna, the transmission pathlength, and wavelength (fig. 7). Overall transmission efficiency must also account for the losses along the transmission path, the aperture illumination efficiency, and the percentage of beam intercepted by the receiving aperture. Goubau also considered the energy density distributions in a beam for increasing efficiencies (fig. 8). For efficiencies approaching 100 percent, the distribution is a "truncated Gaussian".

Also, Goubau calculated the aperture area required for given values of efficiency and amount of power (see table 1). Calculations show extremely large aperture areas required for high efficiency. For airplane platforms, large aperture areas obviously are impractical, since large wing areas must be provided as well. Experiment in the lab has verified an efficiency factor of better than 99 percent using the Gaussian illumination distribution at both the transmitter and receiver surfaces. However, Brown stated in reference 13 that no such situation exists in a practical sense. This study, therefore, assumes a uniform illumination distribution, in both phase and amplitude, over the face of the array.

The primary objective of the transmitter antenna is to shape the transmitted beam so that the radiated power is concentrated in a particular direction in free space (ref. 16). A measurement of the effectiveness of the antenna's ability to concentrate radiation in a given direction is called the "antenna gain" (see Appendix A for analytical expressions of gain). The larger the aperture, the larger the

gain. For the same aperture, maximum gain can be achieved by a uniform illumination.

Figure 9, reproduced from reference 16, is a transmission pattern of the antenna plotted in polar coordinates. Zero db on this plot represents the maximum power. As this plot indicates, there is a favored direction of propagation. The largest "lobe" in the figure is called the "main lobe;" other smaller lobes are "sidelobes." Sidelobes are caused by the discontinuity presented by the edge of the antenna being at a point of high intensity. If it is desirable to reduce the sidelobe, alternative illumination distributions can be employed (fig. 10 taken from ref. 17). As seen by figure 10, techniques to combat sidelobes often lead to a wider main lobe as well as an increase in the beam width. In trying to select an optimum illumination pattern, the system designers, therefore, must evaluate tradeoffs involving maximum gain with some sidelobes (i.e., uniform illumination) versus reduced gain and a reduction in sidelobe levels (tapered illumination). Such a tradeoff study is beyond the scope of this study.

Using the uniform phase and amplitude distributions, the far-field power density distributions are derived mathematically for both circular aperture and highly one-dimensional, rectangular aperture (refs. 18-19). For the circular aperture (normalized with respect to its maximum value), the power density distribution for off-boresight measurements is the square of the first-order, first-kind Bessel function (fig. 11). Figure 12 shows the distribution for a rectangular aperture in a plane containing dimension a. This is also the

distribution of an aperture whose dimension b is small compared to a. The behavior is that of the square of the function sin x/x, where x is a dimension measuring the off-boresight deflection. Far-field pattern for a rectangular aperture whose b dimension is not small compared to dimension a is more complex. The expression for power-density distribution can be found in reference 17. Figure 13 compares the distributions of a circular transmitter and a rectangular array (whose maximum dimension is equal to the diameter of the circular array). As can be seen from this figure, a circular aperture is more efficient in the sense that it has lower sidelobe levels; thus, it concentrates more energy in the main lobe than is the case for the rectangular aperture. This study will, therefore, employ a circular aperture in the analysis to follow.

The far-field pattern for a parabolic disk is reduced by approximately 30 percent in intensity because of the phenomenon called "aperture blockage". The "source" (or "feed") and feed transmission line combine to create an obstacle in the direction of radiated energy. The expression for gain, therefore, contains a factor of 0.70 (see Appendix A) to account for this loss.

The signal polarizations also have effects on power transmission. In order to illustrate the polarization of a signal, it is necessary to consider wave motions. In nature, there are two types of wave motion: longitudinal and transverse. Longitudinal wave vibrations occur parallel to and transverse wave vibrations perpendicular to the direction of wave motion. Sound waves are primarily longitudinal;

fluid-surface waves and electromagnetic waves, which include microwave radiation, are primarily transverse. Since microwaves are transverse, either the electric field (E), the magnetic field (H), or both, vibrate in a plane perpendicular to the direction of propagation (fig. 15). The polarization of an electromagnetic wave is, by definition, the direction of the E vector. Figure 14 is an example of a linearly polarized wave whose E vector lies entirely in a fixed plane as the wave propagates in the direction shown. The attenuation of power transmission due to signal polarizations must also be considered here because for maximum efficiency, the transmitting and receiving antennas should have the same polarization. If, for example, the receiver is polarized at 90 degrees with respect to the transmitter, it will receive no power at all.

Circular polarization refers to the circle (a helix in three-dimensional view) swept out by the tip of vector E_r (fig. 15) whose components lie in horizontal and vertical planes. These components are equal in magnitude but have a phase angle difference of 90 degrees between themselves. Circularly polarized signals are often transmitted when the polarization of the receiving antenna is unknown in both magnitude and direction. This study assumes the use of orthogonal receiving antennas to eliminate concerns about signal polarization.

2.2.3 Power Reception: The amount of power intercepted depends directly on the efficiency of the receiving antenna which also rectifies microwave energy into direct current power. This special device has been named the rectenna. Present design of the rectenna evolved from a "string-type" rectenna (ref. 20) as shown on figure 16. Present

rectenna consists of a foreplane, a reflecting plane, and a separation plane between the foreplane and the reflecting plane. The collection and rectification function are carried out at the foreplane, which is a sheet of lightweight Mylar film. The actual circuitry is seen as copper etchings on both sides of this Mylar fiber (thin-film printed circuit). The presence of the reflecting plane, which is metallized up to a small depth to minimize its mass, only adds to the overall efficiency of the rectenna.

Reference 13 provides a list of the advantages of the thin design (over an earlier design using ellipsoidal reflector). First, the design has little or no directivity in order to avoid having to point to the transmitter antenna all the time. Second, heat is locally dissipated by convection. Finally, the acceptability of relaxed mechanical tolerance minimizes weight. Figure 17 shows a sketch of the thin-film rectenna as proposed in reference 21. Table 2 is a summary of different efficiency factors associated with the parts of figure 3. Even though 0.95 is the maximum transmission efficiency, the assumption of the uniform phase and amplitude distributions made earlier gives a lower efficiency factor (see fig. 8). This study assumes the rectenna is located on the lower surfaces of the wing.

2.3 Cost Models

This study uses the same cost model as presented by Brown (ref. 14) for the phased-array transmitting antenna. The relationship is as follows:

Life-cycle cost = Antenna cost + Equipment cost + Energy cost

$$= aA_t + mP_t + \frac{bc\ P_t}{\eta_1}$$

P_t = total radiated power

A_t = transmitting antenna area

a = cost per unit area for antenna

m = cost (per kilowatt of radiated power) of equipment

c = cost of 60-Hz energy per kw-hr

b = number of hours in life cycle

η_1 = conversion efficiency (from 60-Hz to microwave) = 0.60

Using representative values (Table 3) for a, , and bc/η_1, the life-cycle cost is plotted against antenna area (fig. 18). The minimum point for cost occurs approximately where the power cost is equal to the antenna cost. This minimum point can also be derived analytically (ref. 14). Depending on the power requirements of the high-altitude platform, the power density at the rectenna varies. Figure 19 plots the cost against antenna area for a specific value of power density at the rectenna. Brown, in reference 14, showed that the minimum cost increased with square root of the rectenna power density, and this trend is implied by figure 20.

For parabolic reflectors, the antenna cost is an exponential function of its diameter (ref. 20). The expression for antenna cost is:

Antenna Cost = $aD_t^{2.5}$ where D_t = reflector diameter.

Reference 20 provided a range for a from 0.6 to 1.2 $\$/ft^{2.5}$. Other than the above modification to cost model for phased array, the cost

components of the cost model (due to equipment and hours in life cycle) remain the same. Figure 21 is a plot of life-cycle cost versus antenna diameter. Appendix B provides an analytical derivation of the minimum-cost point.

The use of the above two cost models assumes the airplane cost is not included, the development cost is already written off, and some production experience has been accumulated ("learning curve") so as to obtain favorable unit costs. As the airplane cost is assumed to be a fraction of the life-cycle cost, these models should give a close estimate of the total cost. Table 3 gives the range of values of a, bc/n_1, and m as they will be used throughout this study.

2.4 Tracking and Pointing Method

The microwave beam must be focussed on the rectenna at all times. For a mechanically steerable parabolic reflector, it is self-focussed. To point the beam in the proper direction, sensor feedbacks (mounted on the transmitter surface) are compared and any imbalance results in a change in the pointing direction. Reference 14 also suggested the use of a beacon beam at the center of the rectenna to focus and point the beam from a phased array in the desired direction. This method compares phase fronts of the individual modules (fig. 6) to that of a center module and makes changes to focus and point the beam in the right direction.

Another attenuation factor on the power transmission efficiency is the beam deflection angle. For a phased array only, the amount of available power at the rectenna is reduced by approximately the square

of the cosine of the deflection (pointing) angle of the beam as measured from the vertical axis (fig. 22a).

The flight path provides an additional efficiency factor to consider. For an aircraft in turning flight, since the microwave beam is not perpendicular to the rectenna, power available is further reduced by the cosine of the sum of roll angle of the aircraft and the pointing angle defined in the paragraph above (fig. 22a). This attenuation factor becomes the sine of the sum of the flight path angle and the tracking angle measured from the horizon (fig. 22b) for climbing flight (ref. 12).

Mechanical tolerances as well as aperture current errors can produce errors in the pointing of the antenna beam. The Lincoln Laboratory Haystack Hill antenna (120-foot diameter paraboloid) has a peak uncertainty in pointing of 0.003 degree (ref. 22). Brown (ref. 14) obtained the same estimate using a phased-array configuration tracking a platform at 20-km altitude. This study assumes the same pointing accuracy in all the calculations to follow.

Design values this study follows are listed in Table 4 for both phased array and parabolic configurations. Table 5 is another comprehensive list of all attenuation factors on power transmission covered up to this point.

CHAPTER 3

WIND AND TURBULENCE

The ability of high-altitude aircraft to stay near a ground source of power is important in wind environments. An understanding of the wind structure at high altitude is therefore essential to the designer's ability to estimate the size of the powerplant needed in generating sufficient thrust to avoid being blown away.

This study uses the 99-percentile wind profile employed in earlier studies (refs. 11-12). This profile is a statistical measurement of wind velocity versus altitude (fig. 23) for all five launch and landing sites of space vehicles from east to west coast of the United States (ref. 23). Figure 23 shows the scalar values of wind speed, without regard to wind directions. Straight line segments connected altitude levels. Values of wind speed indicated a peak value was reached at about 12 km (39,000 ft.), attributed to jet stream effect, gradually decreased to about 135 ft/sec at 70,000 feet for the 99 percent profile. Another wind study specifically performed for high-altitude platform concepts arrived at approximately the same value for maximum wind speed (ref. 24). The referenced study also recommended, based on wind profiles, "minimum wind altitudes" of about 59,000 to 62,000 feet for summer operations and 69,000 to 72,000 feet for other seasons.

Turbulence at high altitude was also studied. Measurements taken by aircraft such as the U-2 and XB-70 indicated that high-altitude air was relatively free of turbulence (ref. 11). It is often emphasized that gust structure is not entirely understood. "Universal" gust formulation has therefore not been available to be applied to all design cases.

CHAPTER 4

VEHICLE SYSTEMS

The vehicle aerodynamics and systems have several special features. These are introduced in this chapter. The familiar vehicle system is composed of the propulsion, payload, and energy storage components. The constraints uniquely imposed on the vehicle flight path and its structure factor will be examined following the system descriptions.

4.1 Propulsion System

The proposed propulsion system uses an electric motor connected to a propeller by a gear system. The direct-current electric motor has permanent magnets made from Samarium-Cobalt material attached to its rotor shaft. Interactions between the magnetic field produced from this permanent magnet and the one from stator windings produce mechanical rotation (ref. 25). The conventional switching/commutation using brush or slip ring can then be eliminated because no external excitation is required for the rotor field due to its permanent magnets. Electronic commutation using solid-state devices will still be required; however, with the problem of brush wear eliminated, the motor is more reliable without generating electromagnetic interference. Other advantages over conventional motors include reduced rotor diameter, high efficiency over a wide range of speeds, and high power-to-weight ratio. Table 6 compares the specific weight of different energy converters. The specific weight for the Samarium-Cobalt design is 0.57 lb/hp using

projections from a NASA-Lewis study. This study currently forecasts 1987 as the technology readiness date. Table 7 lists the characteristics of present and future designs. Metglas, seen from this table, is an advanced magnetic material that offers weight savings in motor weight.

A reduction gear would be needed to connect the motor to the propeller. This study assumes a gear weight based on the following formula given by reference 11:

Gear Weight = 0.3 x maximum motor horsepower

Reference 12 also stated that this formula closely approximates the results given by detail-design methods. Table 8 summarizes the design parameters for motor, gear, and system.

Other equipment must also provide power transfer, switching, battery-charging and circuits, and dissipation of excess power. Goldsmith and Reppucci (ref. 26) projected a value of 65 W/lb for power processing devices dedicated to payload functions. They also gave 50 W/lb as the value of current devices. Reference 11 provided, based on advanced military aircraft, a value of 250 W/lb as the estimate on power-to-weight design parameter for power processing devices dedicated to propulsion power alone. Table 9 summarizes all values presented thus far on power-processing devices.

The last element in the propulsion system is the propeller. A large-diameter, low-speed design is necessary because high efficiency is desired in the low dynamic pressure encountered in flight (leading to a low-thrust loading). Reference 5 recommends a tradeoff study to

determine if the benefit of a three-bladed propeller (less vibrations) is worth the loss in efficiency compared to a two-bladed propeller. Consideration of minimizing flow disturbances may lead to selection of a pusher propeller configuration. Table 8 presents the design parameters for motor, gear, and propellers.

4.2 Energy Storage Systems

Energy storage technologies are of great interest to high-altitude aircraft because these technologies offer secondary power sources during emergency situations or during the glide portion of the boost-glide flight modes. This study will examine briefly the characteristics of the specific technologies.

(a) Battery Technology: The battery converts chemical energy within its container directly into electrical energy. For applications in space satellites where high reliability and long life are needed, the Nickel-Cadmium battery has been employed quite often. One performance parameter used to compare different batteries has been the specific energy. Table 10 gives the range of the specific energy parameter for different batteries (ref. 27). As seen, the silver-hydrogen batteries offer the highest specific energy but development problems thus far have prevented widespread use of this type of battery for space satellites (ref. 27).

Another performance parameter is the depth-of-discharge, the percentage of specific energy that can be withdrawn from the battery without affecting its efficiency. The depth-of-discharge is inversely proportional to the battery life (fig. 24). Battery life, in turn,

limits the number of charge/discharge cycles. Long-endurance missions generally require a large cycle number. In this regard, the Nickel-Hydrogen battery has an advantage over the Nickel-Cadmium battery in that it is able to offer deep depth-of-discharge for the same battery life as Ni-Cd battery. Deeper depth-of-discharge, along with higher energy density, means that the "usable energy density" of Ni-H_2 battery is higher than that of Ni-Cd battery.

Stadwick (ref. 27) compared weight and volume of the above two batteries. Figures 25 and 26 show a weight advantage of Ni-H_2 battery at the expense of bigger volume. Ni-H_2 batteries, starting in 1983, will be used on telecommunications satellites in place of Ni-Cd batteries.

(b) Fuel Cells: Fuel cells convert chemical energy, from reactants drawn from tanks outside its container, into electrical energy. One notable example is the hydrogen-oxygen fuel cell being deployed on the Space Shuttle Orbiter. Depth-of-discharge for rechargeable fuel cells is as high as 90 percent. The essential characteristic that distinguishes a fuel cell from a chemical reactor (battery) is the spatial separation of charge and reactants (fuel and oxidant). Due to this separation, the chemical reaction occurs only when an electric circuit is completed (ref. 28). This circuit is part electrolytic and part electronic (Fig. 27). Direct contact between reactants, by diffusion across the electrolyte, results in loss of capacity. Maximum power supplied by a regenerative fuel cell in 1981 was 350 kW (ref. 29). This

particular system, designed for satellites, has a total system energy storage density of 17.9 W-hr/lb.

Comparison of energy density between fuel cells and batteries requires specification of discharge time of fuel cells. The longer the discharge period, the higher the energy density of fuel cells since only the tank size increases. Fuel cells also require 30 to 60 percent more mass for thermal control and charging power than batteries. The overall charge/discharge efficiency is less than 50 percent for today's fuel cells and life expectancy of present systems is about 20,000 hours. The 1990's goals call for 60-percent efficiency, 40,000-hour life, and specific power range of 100 to 200 W/kg (ref. 30).

(c) Flywheels: Inertial energy can be converted to electrical energy using a device called a flywheel. The energy is stored in the rotating flywheel in the form of kinetic energy. Electrical power, when required, is extracted by attaching a generator to the wheel shaft and despinning the rotor. The generator can be converted into a rotor by electronic switching. Other key technologies incorporated into the flywheel are the following: (a) magnetic suspension close to the geometric center of the rotating mass, (b) a no-wear mechanism in a vacuum environment to minimize losses at high rotational speeds, and (c) electronics for the motor/generator combination (fig. 28). The motor/generator combination is of the Samarium-Cobalt type discussed earlier. Flywheel devices, unlike batteries, are insensitive to depth of discharge. Charge/discharge cycles easily reach 100,000. Among the disadvantages, there has been no operational system designed for

aerospace purposes. Most available information gave energy density not of the complete system but of the disk alone, making it very difficult to compare against performances of fuel cells or battery systems. Table 11 presents a laboratory unit's characteristics of a system designed for satellite use (ref. 31).

Reference 11 compared the usable specific energies (from batteries, regenerative fuel cell, and flywheel) and concluded that the Ni-H_2 battery system was favored at all times if the requirement for storage power was one hour or less. This study assumes the same requirement on Ni-H_2 batteries. Table 12 gives the design criteria on power storage.

4.3 Aerodynamics and Stability

Long-endurance characteristic of a high-altitude aircraft demands a high cruise-lift coefficient and a very low power. The aerodynamics of flight at this high altitude is also affected by a low Reynolds-number flow. There have been a number of attempts to design high-lift, low-drag, low Reynolds-number airfoils as indicated by figure 29. This figure shows lift-drag polars that were obtained by experiments (ref. 5). Airfoil design must also provide cooling flow over the rectenna surface that is integrated with the wing lower surfaces. As a result of the wide range of lift coefficient over which drag coefficient changes very little, this study assumes the following form for vehicle drag coefficient.

$$C_D = C_{D_o} + C_L^2/\pi ARe$$

where

C_{D_o} = vehicle's profile drag coefficient

AR = aspect ratio

C_L = lift coefficient

e = Oswald efficiency factor

The Oswald factor is assumed to vary linearly with aspect ratio:

$e = 1 - (0.009)(AR)$ (ref. 7)

The vehicle profile drag coefficient is comparable to that of a conventional motorized glider. Based on this assumption, reference 7 estimated C_{D_o} to be 0.02.

High aspect ratio is desirable for good aerodynamic efficiency. However, figure 30 indicates that as span length is increased (higher aspect ratio), power densities of outboard regions are considerably reduced, resulting in less power being successfully intercepted for on-board use. Increasing the diameter of a transmitter causes less wing-tip attenuation compared to smaller transmitters (fig. 31); however, larger transmitters are more expensive. A representative aspect ratio of 10 is therefore assumed in this study.

The low-power requirement on HAPP makes it desirable to design for inherent stability since a stability augmented system would create additional demand on power besides making the overall system more complex. As opposed to conventional aircraft, there would be no center-of-gravity limits because there would be no weight change.

4.4 Structure and Fatigue Factor

The microwave-powered HAPP is designed to consume as little power as possible; consequently, it must be constructed of lightweight material. Current sources of turbulence do not contain data for short-wavelength

gusts which are relevant to HAPP design. Because of this, and because the long duration of HAPP flights preclude frequent inspections, all referenced HAPP studies preferred conservative fatigue-load design factors.

This study assumes that the proposed vehicle resembles a motorized glider in its configuration. A feasible design for this paper, based on a survey of glider specifications from reference 32, would have a structural weight fraction of at least 0.6. It was assumed, therefore, that up to a maximum of 40 percent of vehicle weight would be set aside for power-processing devices, energy-storage system, payload, and propulsion system. The rest of the vehicle weight would come from aircraft control system and structure weight. An analytical expression for structural weight fraction can be found in Appendix A.

4.5 Vehicle Flight Paths

The basic requirement on any vehicle flight path is that it must allow for adequate tracking by a ground station. Data from Table 6 suggest that flight paths be contained within a cone, whose vertex angle is 10 degrees at most, for a phased-array configuration. Parabolic reflectors can track flight paths which are confined to the planes containing the reflectors. Considerations of the attenuation factors (Table 5) may further influence the choice of possible flight paths.

4.6 Payloads

Payloads must be minimized in weight and carefully integrated into the vehicle in order to keep vehicle size as small as possible. Beyond these general guidelines, however, payload characteristics such as

volume, weight, and power vary with the nature of the proposed missions. This study chooses, as a representative mission, a communications-relay mission. A study conducted by the Lockheed Company for the Air Force High-Altitude Aircraft Program indicates that payload for such a mission, on the average, weighs 100 pounds, occupies 3-feet^3 volume, and has a power requirement of 1 kilowatt. The cited study considered airplanes whose gross weight ranged from 1,000 to 40,000 pounds. The reference payload for this study will assume the above characteristics.

CHAPTER 5

VEHICLE OPERATIONS

The normal takeoff procedures employed by conventional aircraft are not suitable for microwave-powered HAPP's because HAPP's do not possess any significant internal power source. Heyson (ref. 9) suggested that an agricultural aircraft, due to its excess thrust, be utilized to tow HAPP's up to a 3-km altitude, in proximity to a ground station. Following the release from the tow aircraft and motor start, a series of climbing turns would bring HAPP's up to their cruise altitude. Another launch option would be to equip the HAPP with a jettisonable power pack. Extra weight of this power pack would not be a problem because the airplane climbs more efficiently in the denser air of low altitudes (ref. 8). Propellers ground clearance would also be another problem. The large dimension of the propellers would necessitate the use of a wheeled dolly (in place of a long landing gear) upon which a HAPP would be mounted during the ground taxi run. In keeping the HAPP close to a ground station, a launch day with favorable weather would be selected.

The recovery procedures would use the gliding flight. The propellers would be stopped and locked in a horizontal position during the recovery phase. This phase could also happen when low-altitude winds are calm due to the low stall speeds of HAPPs. The long duration of HAPP flights would make it possible to choose periods of favorable

weather. Another consequence of the long duration is the few times that the takeoff and recovery procedures would be activated compared to the frequency of takeoffs and landings of conventional aircraft.

There are several modes of operation for a HAPP. In one mode, the vehicle circles above a point on the ground while continuously receiving power from a station located within this circle. A small battery would be needed to power the control surfaces and navigation equipment in case of a short-term interruption of ground power. This continuous power mode can best be employed by phased-array systems whose three-dimensional tracking capability allows a variety of flight paths within its 10-degree "power cone."

The boost-glide mode described in Chapter 1 can be employed when the glide portion of the flight path cannot be contained within the above power cone. Parabolic reflector systems are able to efficiently track vehicles utilizing this intermittent power mode if the flight paths are two-dimensional (fig. 32). During the glide portion of the flight, payload power is extracted from on-board batteries which are recharged during the climb phase. If the vehicle fails to receive power from a ground station in this mode of operation, it will lose altitude before being able to receive power from the next ground station of the chain of stations positioned along the desired direction of flight.

This paper will consider only the two modes (continuous and intermittent) of operation described in this chapter. The continuous and intermittent (or boost-glide) modes are analyzed only with array and dish antennas, respectively.

CHAPTER 6

ANALYSIS AND DISCUSSION

The important technologies mentioned in earlier chapters are now incorporated in analyses of microwave-powered flight at cruise conditions. Appendix A provides a method of relating the vehicle characteristics such as aspect ratio and airspeed to the transmitter size and power. The effects of vehicle flight mechanics on power requirements and, therefore, size can be evaluated. Cost models presented earlier allow cost estimates to be made as soon as total power radiated and size of the transmitter are known. Combinations of changes in design criteria serve to establish trends on vehicle size or system cost. For example, the effect of simultaneous increases in transmitter size and power could be analyzed to see whether it would reduce the vehicle size.

The following analyses concentrate on effects of different wind conditions and flight mechanics on both vehicle size and system cost. The continuous and intermittent power modes are also assumed for each wind condition.

6.1 Continuously Powered Vehicle

The continuous power mode employs a phased-array transmitter (fig. 5) for both the zero-wind speed and nonzero wind speed cases.

6.1.1 Zero-Windspeed Case: There are several considerations with respect to minimizing the power requirement. First, concerns about the

vehicle being blown out of the transmission range notwithstanding, low values of equivalent airspeed are employed in this flight environment. Secondly, the available power is strongly influenced by the turn radius of the vehicle's assumed circular flight path (whose center coincides with the phased-array transmitter). A small turn radius would produce a large roll angle, the propulsive power would be increased while the available power would be decreased (the rectenna is less "visible" to the oncoming beams). The ratio of the propulsive power to the available power would be very large at small turn radii. This power ratio is plotted against the turn radius in figures 33a and 33b. As seen for each value of the wing loading, the ratio decreased until a minimum value was reached. The power ratio slowly increased as larger turn radii were reached because while the required propulsive power was less, the available beam power was even smaller (than those at smaller turn radii) as the beam was deflected at larger angles from the vertical axis. The above trend on the available power can best be seen by plotting its "efficiency" factor $\cos^2 \theta_o \cos (\theta_o + \phi)$ (equation (14), Appendix A) against the turn radius (fig. 34). As seen from this figure, maximum values were reached at the same turn radii that produced minimum values of the power ratio on figure 33. The optimum turn radii vary from 3600 feet to 6300 feet for the wing loadings shown. Appendix C offers an expression for $\cos^2 \theta_o \cos (\theta_o + \phi)$ in terms of the turn radius and the vehicle's characteristics.

A vehicle sizing algorithm was written to facilitate the computations involved. The algorithm selected an optimum turn radius based on

the above considerations. Next, payload characteristics, component efficiencies, and vehicle aerodynamics were specified. Assuming a value for P_t (equation (14), Appendix A) allows the wing area to be calculated. The structural weight fraction is then calculated. If it is not at least 0.6, calculations are repeated with a different assumed value for P_t. The estimate on the system cost can be made if unit costs are also specified earlier.

The predicted size and annual cost for several sample cases are shown in figures 35 and 36. The vehicle size increases linearly with increased payload power (fig. 35). This is predicted by equation (16) of Appendix A. The changes in slopes of the curves were caused by the structural weight fraction exceeding the minimum required value of 0.6. The annual cost is plotted against the power cost (the term bc/η_1 of section 2.3) in figure 36. The cost estimates were very close for different payload weights. The resulting linear increases for the same amount of power consumed were direct results of higher unit costs.

Variations from the design values that were made on the propulsive efficiency and the vehicle's profile drag coefficient. The required propulsive power per unit of wing area went up as a result of decreasing propulsive efficiencies and higher drag coefficients (equation (9) of Appendix A). An examination of the structural-weight-fraction expression revealed that the payload weight per unit of the wing area was reduced in order to keep this fraction constant. The payload weight was held constant so the wing area was increased as a result. Figure 37

shows the results for the case of a 100-pound payload weight (reference payload).

Reductions were also made on the battery endurance T and the structural weight fraction. This fraction includes the sum of two components: the propulsive power per unit of the wing area and the payload weight per unit of the wing area. The propulsive component is unchanged when the structural weight fraction is lowered. The payload weight (per unit of wing area) component therefore must be increased in order to reduce the fraction. The payload weight was held constant, resulting in a decrease in the wing area. The smaller sizes as the structural weight fraction is lowered are shown by figure 38. Likewise, the reductions in the battery endurance parameter T caused both of the above components (payload weight and propulsive power per unit of the wing area) of the structural weight fraction to decline. The fraction itself, as a result, is decreased if the wing area is kept constant. By proportionally reducing the wing area, the fraction can be kept constant. The net effect (lowering the parameter T decreases the size) is also shown by figure 33 for a 100-pound payload weight.

Another consideration involves the vehicle size versus the cost of the transmission system. The cost of the transmission system as formulated does not include the airplane cost. The same payload power can be extracted from larger vehicle sizes (resulting from heavier payload weight) as shown by figure 35. However, the power density (per unit of wing area) is reduced if the payload power is kept unchanged as vehicle size is increased (the required propulsive power per unit of wing area

is always constant by using equation (9) of Appendix A). The system cost is proportional to the power density at the rectenna (section 2.3) and, hence, is also reduced for larger vehicle sizes. Figure 39 shows a slight drop in cost for heavier payload weights (larger vehicle sizes) as payload power is kept constant. The above tradeoff between cost versus size is possible only if a larger vehicle size does not pose operational problems.

6.1.2 Non-zero Wind Speed. There are alternative flight paths available to the vehicle in the presence of winds. The vehicle could climb to a higher altitude to seek more favorable wind speeds as figure 23 indicated, providing there is no adverse effect on payload capacity. A comprehensive list of possible maneuvers to counter wind effects depends on many other factors like payload power and attenuation factors (ref. 12).

The flight paths for vehicles constrained in a constant altitude were evaluated by Sinko (ref. 35). One flight path would combine a constant-radius turn segment and a straight flight segment. The vehicle heading is into the wind at the start and completion of the turn segment. The vehicle returns to the starting position by employing a straight flight segment into the wind following the completion of the turn. The ground track resembles a letter "D" and increases in its maximum dimension (compared to the diameter of a zero-wind circle discussed in section 6.1.1) depending on the ratio of the wind velocity to the vehicle velocity (fig. 40).

Another flight path was also considered for a vehicle flown at a constant altitude. Following this path, a constant-radius, left turn occurs when the vehicle faces a "head" wind. A right turn would then be executed to bring the vehicle into the head wind again. The left-turn, right-turn sequence would be followed by a right-left sequence to return the vehicle to the starting point. The ground track would resemble a "Figure-8." Under the ideal condition of zero wind speed, this "Figure-8" is actually two adjacent circles. The maximum dimensions of the Figure-8 tracks would decrease as wind speed becomes larger and larger (fig. 41).

The maximum dimensions for both of the above ground tracks are compared in figure 42. Starting from a sum of the diameters of the contiguous circles at zero wind speed, the maximum dimension for a Figure-8 track decreases to zero as the wind speed approaches the vehicle speed. The vehicle would then be in a "hovering" flight. By contrast, the maximum dimension of a D-shaped track would be equal to the diameter of the zero-wind circle at zero wind speed, but would increase until it is about three times this diameter as the wind speed approaches the vehicle speed (fig. 42). The transmission efficiency of the phased-array transmitter suffers if the beam pointing angle has to be increased to track the vehicle (fig. 22a). A larger maximum dimension of the ground track necessitates a larger pointing angle. Following this logic, it is necessary to switch from a "D-shaped" track to a "Figure-8" track as the wind speed is about 0.35 of the vehicle speed (fig. 42).

The variations of the power ratio (the required power divided by the available beam power) are considered because of the irregular shape of the ground track. Unlike the constant power ratio of a zero-wind, circular ground track considered earlier, the power ratio for a D-shaped track varies because the beam pointing angle has to be changed regularly to track the vehicle. Assuming the station is located at the center of a "D" track, the power ratio is plotted against the angle ψ (fig. 43). As ψ varies from 0 to π, the vehicle would travel half of the D-track if the wind direction is not changed. The power ratio for each value of the velocity ratio (the wind velocity divided by the vehicle velocity) rises to a maximum value, then declines (fig. 43). The available beam power is being proportionally reduced as the size of the maximum dimension of the D-shaped track increases in higher wind speeds. The power ratio is therefore highest at the highest velocity ratio (fig. 43). The peaks of the different curves of figure 43 occur at particular values of the angle ψ where the available power is at a minimum (the required power is assumed constant). The variation in the available power is evident by plotting its efficiency factor $\cos^2 \theta_o \cos(\theta_o + \phi)$ against the variable ψ. The same values of ψ that produce peaks in figure 43 cause minimum values of the efficiency factor and, therefore, minimum available power (fig. 44).

The power ratio of a vehicle flying a Figure-8 track is also considered. This ground track is utilized whenever the ratio of the wind speed to air speed is 0.35 or greater as discussed earlier. The power station is assumed to be at the center of this track. As a result, the

horizontal distance between the ground station and the vehicle decreases to zero as it completes one-fourth of the ground track. The direction of motion is indicated by the arrows of figure 41. Because of the symmetry of the ground track, the power ratio is calculated for only one-fourth of the track (fig. 45). For the same angle ψ of figure 45, the size of the track shrinks as the wind speed increases, enabling the vehicle to receive more of the available power compared to the amount of receivable power at a lower wind speed. Therefore, the ratio of the constant required power to the available power is largest at the smallest velocity ratio. For each curve of figure 45, the maximum ratio occurs at $\psi = 0$ when the constant required power is divided by the minimum available power. This happens when the vehicle is at a maximum distance from the power source. This maximum distance is half of the maximum dimension shown by figure 41. Likewise, the corresponding efficiency factor $\cos^2 \theta_o \cos(\theta + \phi)$ is minimum at $\psi = 0$ because the available power is minimum (fig. 46). For the same angle ψ, the highest efficiency of figure 46 corresponds to the highest velocity ratio.

The curves of figures 43-46 are useful in establishing the design point along the ground tracks at different wind conditions. A vehicle sized at the point of maximum power ratio (minimum efficiency) would offer more than enough wing area (rectenna surface) to intercept power for on-board systems at other points of the ground track. The power ratio for a D-track is maximized when the horizontal distance from the

vehicle to the station is greatest. This distance from the design point is calculated by using the method of Appendix D.

The vehicle sizing algorithm of the previous section is modified to include the 99-percentile wind profile of figure 23. The wind velocity can then be calculated at the design altitude. The above algorithm requires the velocity ratio (the wind velocity to the vehicle velocity) as an additional input parameter.

The sizing results provided by the algorithm are shown by figures 47-48. The thrust generated by the vehicle carrying this payload is sufficient to prevent it from being blown away by a wind speed of up to 135 ft/sec at 70,000-foot altitude. The almost identical vehicle sizes, which are proportional to the required power, results from figures 43 and 45 where it is shown that the power ratios (proportional to the required power) are very close at different wind conditions. For the case of a vehicle maintaining a D-shaped track, the increases in the wind speed lead to ground tracks with larger dimensions. More power must be supplied to the vehicle, resulting in the increases in the cost estimates. Because of this effect, the cost goes up as the velocity ratio is increased for the same payload power (fig. 49). Less power is required in the "Figure-8" track because the track size shrinks as the wind speed steps up in its magnitude. The cost savings of figure 50 reflect this condition.

Variations were also made in the transmitter diameter and the resulting vehicle sizes and cost estimates calculated at each diameter. The vehicle size is relatively constant for the same payload weight

(fig. 51). The fluctuations in vehicle size are caused by the actual structural weight fraction exceeding the design fraction. When the antenna diameter is increased from the baseline value of 240 feet, the power that must be supplied to a vehicle can be reduced. The savings in power cost (less power transmitted) are more than offset by the increase in the antenna cost (fig. 18). The net effect is an increase in the total cost (fig. 52). Decreasing the transmitter diameters still leads to an increase in the annual cost estimate because the reductions in the antenna cost are compensated by the rise in the power cost. At the optimum diameter, the cost components are about equal.

6.2 The Boost-Glide Flight Mode

The boost-glide flight mode (chapt. 1) is considered when the vehicle ground track requires a large beam deflection angle for tracking. A parabolic reflector (fig. 6) is suitable for this task since it does not suffer any loss in transmitted power when it is deflected from the vertical axis (table 5). In contrast to the nonplanar flight paths associated with the phased-array configuration of the previous section, the boost-glide flight path would be restricted to a plane generated by the tracking microwave beam.

The boost and glide portions of the flight path are shown by figure 32. The linear altitude gain during the climb period is a reflection of the assumption of constant climb rate. The linear glide portion is a function of the lift-drag ratio of the vehicle. The total range per station (fig. 32) depends on the wind direction and magnitude, the altitude difference achieved by the climb phase, the vehicle climb

rate, and the equivalent airspeed. Appendix E offers a method for calculating the total range. The range computed by this method is important for the purpose of spacing the power stations along the desired ground track. Another performance-related parameter that is also calculated by the method of Appendix E is the glide time. This is the time taken by the vehicle to glide between the maximum and minimum altitudes of figure 32. The glide time determines the required battery endurance. The battery endurance, in turn, affects the structural weight fraction as defined in Appendix A.

The extensive ground track of a boost-glide flight requires some considerations as to the proper location of a ground station given that the total range is calculated by the method of Appendix E. This paper considers every location along the climb range as candidate locations (fig. 53). The flight path and the climb range are discretized into equal segments. The effectiveness of each candidate location is assumed to be measured by the total far-field power density. The total far-field power density is found by summing up the individual power density at each vehicle position. This process is repeated for all m candidate locations. The sum of power density of each candidate location is then plotted against the candidate location measured in terms of its distance from the origin of the climb range called the percent of climb range (fig. 53). As seen from this plot, the power density rises to a maximum, then declines. The optimum location for the ground station is then at approximately 45 to 50 percent of the climb range. This criterion for locating a station would be assumed for all future calculations.

The design point has been chosen to reflect a maximum power ratio (figs. 43 and 45). This practice would be continued for the boost-glide mode. The design point would be at the maximum altitude where the true airspeed is at its maximum value, requiring the greatest amount of propulsive power. A vehicle sized at the design point would therefore have excess power at the lower altitudes where the true airspeed is lowered. The excess power would be used to recharge the batteries (chapt. 5).

The vehicle sizing algorithm of the previous section now accepts the wind direction angle and the wind-scale factor as additional inputs. The wind-scale factor controls the magnitude of the 99-percentile profile of figure 23. A factor of 0.5, for example, would return a profile only half the magnitude of that shown by figure 23.

The total range and predicted span in zero wind speed are given by figures 54 and 55. The total range is the sum of the ranges obtained during the climb and glide phases. Assuming a constant climb rate and a constant equivalent airspeed, the total range is a linear function of the lift-drag ratio and the altitude difference. The minimum altitude is assumed at 60,000 feet, the maximum at 70,000 feet for the best tracking accuracy (chapt. 2). With the same altitude difference, the total range then depends only on the lift-drag ratio (fig. 54). The actual structural weight fraction exceeded the desired fraction at some payload power, causing a change in slope of the curves of figure 55.

The vehicle size is also calculated for a non-zero wind environment. The vehicle airspeed is generally higher than that of a zero-wind case.

This would guarantee that the vehicle is not blown away by a strong wind. Since the wind velocity gradually increases below an altitude of 20 km (fig. 23), the maximum wind speed would be known upon specifying a minimum altitude of flight. For design purposes then, the airspeed at the minimum altitude would have to exceed this maximum wind speed. The effects of the wind direction angle and the wind magnitude on the vehicle size are shown by figures 56 and 57. For the same payload power, the vehicle size decreases slightly as wind magnitude (scale factor) is reduced (fig. 56). This results from a slightly lower demand for propulsive power as the wind resistance is lessened. No such effect is evident when only the wind direction is changed; the sizes are virtually the same (fig. 57).

The total range (per station) is a function of many variables stated at the beginning of this section. For illustration purposes, varying the wind magnitude (or the wind-profile scale factor) produces the profile shown by figure 58. Gradually decreasing the magnitude improves the ground speed proportionally. Range is therefore increased (fig. 58). The gain in range comes at the expense of rising annual cost as the power loss increases with distance. The cost estimate shown by figure 59 is for a reference payload of 100 pounds and 1000 watts.

6.3 Comparative Analysis

Results from the sizing algorithms developed for the boost-glide (parabolic dish) and continuous power (phased-array) configurations were compared. A reference payload that weighs 100 pounds and consumes 1 KW of power was assumed for all comparisons between the two configurations.

Since the cost analysis of this study is limited to the antenna-related costs (excluding considerations of vehicle costs), the following discussion identifies system type according to the type of transmitter used.

The vehicle ranges for both configurations were not compared because the range for a vehicle powered by an array was limited by the power availability at the extreme deflection angles for the microwave beam (figs. 33-34). Power, not range, was the primary consideration here.

The vehicle sizes were compared for a zero-wind speed case. The sizes were calculated using the same vehicle aerodynamic characteristics for both the dish and array transmitters. The small difference in size arose from the dish-powered vehicle having to extract power from the on-board batteries for a longer period of time (fig. 60). The longer battery endurance did affect the vehicle size as demonstrated earlier (fig. 38).

The size comparison was also made for a nonzero wind speed. A maximum wind speed of 167 ft/sec would be assumed for an array-powered vehicle operating at 60,000-feet altitude. Since the wind magnitude is decreased at higher altitudes, this would also be the maximum wind speed encountered by a dish-powered vehicle whose maximum altitude is 70,000 feet. With the design point for boost-glide flight chosen at this altitude, the dish-powered vehicle has a higher airspeed than that of a local-flight, array-powered vehicle. This difference in speed led to demands for larger propulsive power that accounted for the larger size of a dish-powered vehicle (fig. 61).

The annual cost (excluding the airplane cost) of the dish and array transmitters was compared using the models introduced earlier (section 2.3). The transmitters were assumed to produce the same far-field power density (same vehicle capability). The equipment and power were also assumed to cost the same (per kilowatt of power generated) for both transmitters. The antenna cost of a parabolic dish was higher (fig. 62). The dish transmitter, therefore, cost more for the same vehicle capability (fig. 63).

CHAPTER 7

CONCLUDING REMARKS

A limited study has been made on the sizing and performance of high-altitude, long-endurance vehicles. These vehicles are powered by the microwave beam energy supplied by either a phased-array transmitter for continuosly powered flight or a parabolic dish transmitter for boost-glide flight.

Results have shown that the phased-array configuration is favored over the dish transmitter when the cost estimates for both are compared. Using a reference payload, the predicted vehicle size is less for array-powered vehicles.

APPENDIX A

EXPRESSIONS FOR WING AREA AND STRUCTURAL WEIGHT FRACTION

Wing-Area Expression:

"Radar-range"equation (ref. 33):

$$P_{avail} = \frac{G_1 G_2 \lambda^2 P_t}{(4\pi h)^2} \qquad (1)$$

where P_{avail} = far-field power

h = range of transmission

λ = wavelength

P_t = power transmitted from a ground station

G_1 and G_2 are antenna and rectenna "gains," respectively. Assuming uniform phase and amplitude distributions of power density on surface of transmitter:

$$G_1 = \frac{4\pi}{\lambda^2} A_t \qquad \text{(phased-array configuration)}$$

or $$G_1 = \frac{4\pi}{\lambda^2} (0.7)\, A_t \qquad \text{(parabolic dish)}$$

where A_t = surface area of transmitter

and $$G_2 = \frac{4\pi}{\lambda^2} \eta F S_{wing}$$

where F = percent of wing area, S_{wing}, covered by rectenna

η = "illumination" efficiency
= 1 for uniform illumination

Let θ_o and θ be the pointing and tracking accuracy angles, respectively. P_t for a circular aperture being uniformly illuminated, is given by:

$$P_t(\theta,\theta_o) = \cos^2 \theta_o \; 4 P_t \frac{\left[J_1\left(\frac{\pi D_t}{\lambda} \sin \theta\right)\right]^2}{\left(\frac{\pi D_t}{\lambda} \sin \theta\right)^2} \qquad (2)$$

J_1 is the first-order, first-kind Bessel function.

θ_o is defined in Figure 22a

$\theta = 0.003^0$ (ref. 15)

D_t = diameter of the circular transmitter

For a mechanically steerable parabolic transmitter, P_t is not affected by θ_o (see Table 5):

$$P_t(\theta) = 4 P_t \frac{\left[J_1\left(\frac{\pi D_t}{\lambda} \sin \theta\right)\right]^2}{\left(\frac{\pi D_t}{\lambda} \sin \theta\right)^2} \qquad (3)$$

S_{wing}, the wing area, is less visible (not perpendicular to microwave beams) when the vehicle is climbing or turning (figs. 22a, 22b). Therefore, the effective wing area is:

$\cos (\theta_o + \phi) S_{wing}$ (turning flight)

$\sin (\theta_o + \gamma) S_{wing}$ (climbing flight)

Angles θ_o and γ are shown by figures 22a and 22b. θ_o, in climbing flight, is the tracking angle shown by figure 22b.

For a vehicle in turning flight, powered by a phased-array ground antenna, substitute (2), appropriate expressions for G_1 and G_2 into (1) and simplify:

$$P_{avail} = \frac{F \cos^2 \theta_o \, P_t \cos(\theta_o + \phi)}{\pi x^2} \left[J_1 \left(\frac{\pi D_t x}{\lambda h} \right) \right]^2 \eta \, S_{wing} \qquad (4)$$

where $x = h \sin(0.003°)$

h = transmission range

For a vehicle in climbing flight, powered by a parabolic dish, substitute (3) and expressions for G_1 and G_2 into (1):

$$P_{avail} = \frac{\eta F \, S_{wing} \times 0.7}{\pi x^2} P_t \left[J_1 \left(\frac{\pi D_t}{\lambda} \sin \theta \right) \right]^2 \sin(\theta_o + \gamma) \qquad (5)$$

The required propulsive power (in steady, level flight) per unit wing area:

$$\frac{P_{prop}}{S_{wing}} = D \frac{V_o}{\eta_{prop} S_{wing}}$$

where η_{prop} = the propulsive efficiency

V_o = the air speed of the vehicle in level flight

D = the drag force

$$\frac{P_{prop}}{S_{wing}} = \left(C_D \frac{1}{2} \rho V_o^2 S_{wing} \right) \frac{V_o}{\eta_{prop} S_{wing}} = \frac{\rho}{2 \eta_{prop}} C_D V_o^3 \qquad (6)$$

where ρ = the air's density

C_D = the vehicle's drag coefficient (defined in section 4.3)

Let V be the airspeed in turning flight. If the lift coefficient is assumed to be constant during turning and level flight, then:

$$C_L\Big|_{\substack{\text{level}\\\text{flight}}} = C_L\Big|_{\substack{\text{turning}\\\text{flight}}}$$

$$\frac{W}{\frac{1}{2}\rho V_o^2 S_{wing}} = \frac{W}{\frac{1}{2}\rho V^2 S_{wing}\cos\phi} \tag{7}$$

W = the aircraft weight

ϕ = the roll angle

(7) simplifies to: $V = \frac{V_o}{\sqrt{\cos\phi}}$ (8)

The required propulsive power per unit wing area in turning flight at a constant C_L is found by substituting (8) into (6):

$$\frac{P_{prop}}{S_{wing}}\Big|_{\substack{\text{turning}\\\text{flight}}} = \frac{\rho}{2\eta_{prop}(\cos\phi)^{1.5}} C_D V_o^3 \tag{9}$$

or $P_{turn} = \frac{P_{level}}{(\cos\phi)^{1.5}}$

For a vehicle in climbing flight, the required propulsive power can be developed from reference 36:

$$\frac{P_{prop}}{S_{wing}} = \frac{\rho}{2\eta_{prop}} C_D V^3 + \left[\frac{ROC}{\eta_{prop}}\right]\left[\frac{W}{S_{wing}}\right] \tag{10}$$

where ROC = rate of climb

W/S_{wing} = wing loading

V = air speed

Energy balance equation:

$$P_{prop} + P_{pay} + F_{st} P_{avail} = P_{avail} \left[\frac{F}{F_{rd}}\right] \eta_{rect} \qquad (11)$$

where η_{rect} = the rectenna efficiency (in collection and rectification)

F_{rd} = percent of built-in redundancy of rectenna elements, i.e., extra wing area needed to provide space for backup elements.

P_{avail} = available power

F_{st} = percent of available power dedicated to storage

P_{pay} = payload power

F = percent of wing area covered by rectenna elements

Solve for P_{avail} from (11)

$$P_{avail} = K(P_{prop} + P_{pay})$$

where $K = \left[\frac{F_{rd}}{F}\right]\left[\frac{1}{1 - F_{st}}\right] \eta_{rect}$ = dimensionless constant (12)

Therefore:

$$\frac{P_{avail}}{S_{wing}} = K\left[\frac{P_{prop} + P_{pay}}{S_{wing}}\right] \qquad (S_{wing} = \text{wing area}) \qquad (13)$$

From (4): $$\frac{P_{avail}}{S_{wing}} = \frac{F \cos^2 \theta_o P_t \cos(\theta_o + \phi)\eta}{\pi x^2} \left[J_1\left(\frac{\pi D_t x}{\lambda h}\right)\right]^2 \qquad (14)$$

(phrased-array transmitter)

From (5): $$\frac{P_{avail}}{S_{wing}} = \frac{\eta F (0.7)}{\pi x^2} P_t \left[J_1\left(\frac{\pi D_t}{\lambda} \sin \theta\right)\right]^2 \sin(\theta_o + \gamma) \qquad (15)$$

(parabolic dish)

(a) The wing area for a vehicle in turning flight at constant lift coefficient is found by substituting expressions (14) and (9) into (13) and solve for S_{wing}:

$$S_{wing} = \frac{K\ P_{pay}}{D_1 - K\ D_2} \qquad \text{(phased-array configuration)} \qquad (16)$$

D_1 is the right-hand side of (14), D_2 is the right-hand side of (9), and K is defined in (12).

(b) For a vehicle in climbing flight, powered by a parabolic reflector, the expression for wing size differs only in the definitions of D_1 and D_2. D_1 is now the right-hand side of (15). D_2 is the right-hand side of (10).

Expression for Structural Weight Fraction

Let WFT be the structural weight fraction ($0 < WFT < 1$), W_1 be the total weight of payload, propulsion system, battery, and power-control devices.

$$W_1 = W\ (1 - WFT) \quad \text{where} \quad W = \text{total weight of aircraft}$$

Or: $WFT = 1 - (W_1/W)$

$$= 1 - \left[\frac{W_1/S_{wing}}{W/S_{wing}}\right]$$

In terms of payload power and propulsive power:

$$WFT = 1 - (C_2\ P_{pay}/S_{wing} + C_3\ P_{prop}/S_{wing})/(W/S_{wing})$$

Using Tables 8, 9, and 12, C_2 and C_3 are given as following:

$$C_2 = W_{pay}/P_{pay} + 0.015 + 0.05\ T$$

$$C_3 = 0.004 + 0.05T + 0.0022$$

where
- T = the battery endurance in hours
- W_{pay} = payload weight, lbs
- W/S_{wing} = wing loading, lbf/ft^2
- P_{prop} = propulsive power, Watts
- P_{pay} = payload power, Watts

C_2 and C_3 are in units of lbf/W. WFT is dimensionless.

APPENDIX B

MINIMUM-COST POINT FOR DISH-ANTENNA COST MODEL

$$\text{Life-cycle cost} = C = aD_t^{2.5} + mP_t + \frac{bc\ P_t}{\eta_1} \tag{1}$$

where a, D_t, m, P_t, $\frac{bc}{\eta_1}$ are defined in section 2.3.

P_t is further related to D_t by the following expression:

$$P_t = \frac{\lambda^2 h^2 P_d}{\frac{\pi}{4} D_t^2\ \eta_2\ (0.7)} \tag{2}$$

where P_d = power density at the rectenna

λ = wavelength = 0.12 cm = 0.40 ft.

h = reference altitude

η_2 = rectenna efficiency

0.7 = illumination efficiency for dish antenna

Substitute (2) into (1):

$$C = aD_t^{2.5} + \frac{K}{D_t^2} \tag{3}$$

where $$K = \left[m + \frac{bc}{\eta_1}\right]\left[\frac{\lambda\, h^2\, P_d^2}{\frac{\pi}{4}\, 0.7\ \eta_2}\right]$$

Take the first derivative of (3) with respect to D_t:

$$\frac{dC}{dD_t} = 2.5\ a\ D_t^{1.5} - \frac{2K}{D_t^3} \tag{4}$$

(4) vanishes at a particular value of D_t, let it be D_t^*:

$$D_t^* = \left[0.8\,\frac{K}{a}\right]^{\frac{1}{4.5}} = \left[\frac{m}{a} + \frac{bc}{a\eta_1}\right]^{0.222} \left[\frac{0.8\,\lambda^2 h^2 P_d}{0.7\,\frac{\pi}{4}\,\eta_2}\right]^{0.222}$$

Take the second derivative of (3) with respect to D_t:

$$\frac{d^2C}{dD_t^2} = (2.5)(1.5a)\,D_t^{0.5} + \frac{6K\,D_t^2}{D_t^6} > 0 \text{ for all } D_t > 0$$

Therefore, C is at the minimum value when $D_t = D_t^*$

From (3):

$$\text{Minimum cost} = C^* = a\left(D_t^*\right)^{2.5} + \frac{K}{\left(D_t^*\right)^2}$$

$$= 1.988\; a^{0.444}\left[m + \frac{bc}{\eta_1}\right]^{0.555}\left[\frac{P_d}{0.7\,\frac{\pi}{4}\,\eta_2}\right]^{0.555}(\lambda h)^{1.111}$$

Minimum cost varies with $(P_d)^{0.555}$ whereas it varies with square root of P_d for a phased-array transmitter as noted earlier in the Cost Models section of the text.

APPENDIX C

AN EXPRESSION FOR $\cos^2 \theta_o \cos(\theta_o + \phi)$

The cosine of the pointing angle θ_o:

$$\cos \theta_o = \frac{h}{\sqrt{h^2 + R_o^2}} \tag{1}$$

where h = the altitude of flight

R_o = the vehicle's turn radius (or the horizontal distance from the vehicle to the ground station)

The sine of the roll angle ϕ:

$$\sin \phi = 2\left(W/S_{wing}\right)\left(1/(g\, C_L \rho\, R_o)\right) = K_1/R_o \tag{2}$$

where W/S_{wing} = the wing loading

g = the gravity's acceleration constant

C_L = the vehicle's lift coefficient

ρ = the air's density

$K_1 = 2\left(W/S_{wing}\right)\left(1/(g\, C_L\, \rho)\right)$

$$\cos(\theta_o + \phi) = \cos \theta_o \cos \phi - \sin \theta_o \sin \phi \tag{3}$$

where

$$\sin \theta = \frac{R_o}{\sqrt{h^2 + R_o^2}} \tag{4}$$

From (2):

$$\cos \phi = \sqrt{1 - (K_1/R_o)^2} \tag{5}$$

Substitute (1), (2), (4), and (5) into (3):

$$\cos^2 \theta_o \cos (\theta_o + \phi) = \frac{h^2}{h^2 + R_o^2} \left[\frac{h}{h^2 + R_o^2} \sqrt{1 - \left(\frac{K_1}{R_o}\right)^2} - \frac{R_o}{\sqrt{h^2 + R_o^2}} \times \frac{K_1}{R_o} \right]$$

$$\cos^2 \theta_o \cos (\theta_o + \phi) = \frac{h^2}{(h^2 + R_o^2)^{1.5}} \left[h \sqrt{1 - \left(\frac{K_1}{R_o}\right)^2} \right] - K_1 \qquad (6)$$

APPENDIX D

MAXIMUM BEAM DEFLECTION ANGLE AND RADIAL DISTANCE

(x,y) = the coordinates of vehicle at time t.

(x_o,y_o) = the coordinates of initial position.

R_o = the turn radius of vehicle in zero wind (Appendix C).

Point 0 = location of the ground station.

ψ = the angle between the vehicle velocity vector and the wind vector.

V_a = the vehicle air speed.

V_w = the wind speed.

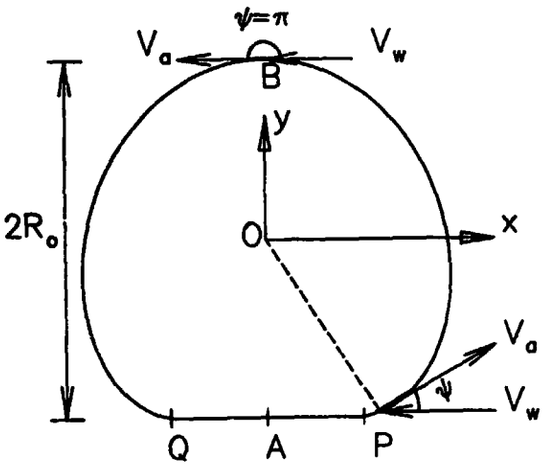

ω = the angular speed = V_a/R_o (1)

The coordinates x,y are given by integrating the equations of motion:

$$x = \int(V_a \cos \psi - V_w)\, dt + x_o \tag{2}$$

$$y = \int V_a \sin \psi \, dt + y_o \tag{3}$$

Substitute $dt = d\psi/\omega$ irto (2) and (3):

$$x = {}_0\int^{\psi} (V_a \cos \psi - V_w) \frac{d\psi}{\omega} + x_o \tag{4}$$

$$y = {}_0\int^{\psi} V_a \sin \psi \frac{d\psi}{\omega} + y_o \tag{5}$$

V_a and ω are assumed constant throughout the flight.
Substitute (1) into (4) and (5):

$$x = R_o \left(\sin \psi - \frac{V_w}{V_a} \psi\right) + x_c \tag{6}$$

$$y = R_o(1 - \cos \psi) + y_o \tag{7}$$

The distances AB, AP can be calculated by (6) and (7) if we let:

$x_o = y_o = 0$ (point 0 of the sketch coincides with point P)

$\psi = \pi$ (the vehicle is at point B)

$$AP = \left|R_o \left(\sin \pi - \frac{V_w}{V_a} \pi\right)\right| = \pi R_o \frac{V_w}{V_a}$$

$$AB = \left|R_o (1 - \cos \pi)\right| = 2R_o$$

$$PQ = 2AP = 2\pi R_o \frac{V_w}{V_a}$$

For a vehicle constrained in a constant-altitude flight, the maximum beam deflection angle occurs when the radial distance (shown by the dashed line of the sketch) is maximized. This maximum radial distance is:

$$d_{max} = \sqrt{\left[R_o \left(\sin \psi^* - \frac{V_w}{V_a} \psi^*\right) + x_o\right]^2 + \left[R_o (1 - \cos\psi^*) + y_o\right]^2} \tag{8}$$

Max. deflection angle = $\tan^{-1} (d_{max}/h)$

where: ψ^* = the value of the angle ψ at which the maximum radial distance occurs.

h = the altitude of flight

ψ^* was found by a numerical method for several values of V_w/V_a.

ψ^*	V_w/V_a
1.04 rad	0.1
0.96	0.2
0.88	0.3

The efficiency factor $\cos^2 \theta_o \cos (\theta_o + \phi)$ (Appendix C) becomes:

$$\cos^2 \theta_o \cos (\theta_o + \phi) = \frac{h^2}{K_2} (K_3 - K_4) \tag{9}$$

where:

h = the altitude of flight

$$K_2 = \left(h^2 + \left[x_o + R_o \left(\sin \psi - \frac{V_w}{V_a} \psi\right)\right]^2 + \left[y_o + R_o (1 - \cos \psi)\right]^2\right)^{1.500} \tag{10}$$

$$K_3 = h\sqrt{1 - (K_1/R_o)^2}$$

K_1 = defined in Appendix C

$$K_4 = \frac{K_1}{R_o} \left[x_o + R_o \left(\sin \psi - \frac{V_w}{V_a} \psi\right)\right]^2 + \left[y_o + R_o(1 - \cos \psi)\right]^2 \tag{11}$$

Variations of $\cos^2 \theta_o \cos (\theta_o + \phi)$ with the angle ψ are shown by figures 44 and 46.

Special Cases:

(a) Zero wind speed: $V_w/V_a = 0$

Let the initial position of the vehicle coincide with point P (see sketch):

$$x_o = |AP| = \pi R_o \frac{V_w}{V_a} = 0$$

$$y_o = -R_o$$

(6) and (7) become:

$$x = R_o \sin \psi$$

$$y = -R_o \cos \psi$$

$x^2 + y^2 = R_o^2$ ("D" track becomes a circular track)

Max. radial distance = $x^2 + y^2 = R_o$ = constant

Max. deflection angle = $\tan^{-1} (R_o/h)$ = constant

(10) and (11) become:

$$K_2 = (h^2 + R_o^2)^{1.500}$$

$$K_4 = \frac{K_1}{R_o} R_o = K_1$$

(9) is independent of ψ and is reduced to the expression (6) of Appendix C.

(b) <u>The wind speed is equal to the vehicle speed:</u> $V_w/V_a = 1$

Let point 0 coincide with point P (see sketch):

$x_o = y_o = 0$

$\psi = 0$ in this case because the wind speed opposes the vehicle speed ("hovering" condition), (6) and (7) give:

$$x = R_o (\sin \psi - \psi) = 0$$

$$y = R_o (1 - \cos \psi) = 0$$

From expression (1) of Appendix C:

$$\cos \theta = \frac{h}{(h^2 + x^2 + y^2)^{0.5}} = 1$$

$$\sin \theta_o = 0$$

$$\cos^2 \theta_o \cos (\theta_o + \phi) = \cos \phi \qquad (\phi = \text{vehicle roll angle})$$

The efficiency factor is again independent of ψ and is constant for a constant ϕ.

Max. radial distance = $x^2 + y^2 = 0$

Max. deflection angle = $\cos^{-1} (1) = 0$

APPENDIX E

THE RANGE AND GLIDE-TIME EXPRESSIONS

The Glide-Time Expression:

Let h_i, h_f, be the intial and final altitudes in meters.

V_e the equivalent airspeed in m/s

t_g the glide time in seconds

From reference 34, the rate of sink:

$$\frac{dh}{dt} = \frac{D}{W} V = \frac{-D}{L} V \qquad (1)$$

where L/D is the lift-drag ratio

V = the airspeed at an altitude $h = [2(W/S)/(\rho C_L)]^{0.5}$

W/S = the wing loading

ρ = the density of air at altitude h

C_L = the lift coefficient

Let $\sigma = \rho/\rho_o$ (2)

ρ_o = sea-level density of air

From (1) and (2)

$$dt_g = -\frac{L}{D}\frac{dh}{V} = -(L/D)\left[\sigma\rho_o C_L/2(W/S)\right]^{0.5} dh = -\frac{L}{D}\frac{1}{V_e}\sqrt{\sigma}\, dh \qquad (3)$$

where $V_e = [2(W/S)/(\rho_o C_L)]^{0.5}$

Reference 5 offers an expression for σ, the dimensionless ratio of densities:

$$\sqrt{\sigma} = 1.29746 \exp(-h/12683.24) \qquad (4)$$

where: h = the altitude in meters.

exp ( ) = the exponential function of base e.

Substitute (4) into (3).

$$\int_0^{t_g} dt_g = -\frac{L}{D}\frac{1}{V_e}\int_{h_i}^{h_f} 1.29746 \exp(-h)/12683.24)dh \qquad (h_f < h_i)$$

$$\text{Glide time } t_g = -1.29746\,(L/DV_e)\int_{h_i}^{h_f} \exp(-h/12683.24)dh$$

$$= 16456\,(L/DV_e)[\exp(-h_f/12683.24) - \exp(-h_i/12683.24)]$$

$$(11{,}000 \text{ m} < h_i, h_f < 20{,}000 \text{ m})$$

The Range Expression (in Gliding Flight):

Φ = the angle between the vehicle speed and the ground track

μ = the angle between the wind speed and the ground track

V = the vehicle airspeed

V_w = the wind speed

V_g = the ground speed

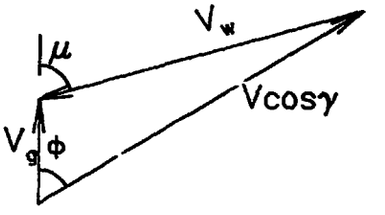

The following assumptions are made for the following equation: (a) a small flight path angle, (b) the vehicle heading is changed to offset the wind effect, (c) the flight path (fig. 32) is completely contained within a plane generated by the tracking microwave beam (ref. 10).

$$V \sin \Phi - V_w \sin \mu = 0 \qquad (5)$$

$$V_g = \frac{dx}{dt} = V \cos \Phi - V_w \cos \mu \qquad (6)$$

From (5):

$$V = V_w \sin \mu / \sin \Phi \qquad (\sin \Phi \neq 0) \qquad (7)$$

Substitute (7) into (6):

$$dx = \left[(V_w \sin \mu / \sin \phi)/\cos \Phi\right] dt - V_w \cos \mu \, dt \qquad (8)$$

(a) "Head" wind: $\mu = 0$

$\sin \mu = 0$

From (5) with $V \neq 0$: $\sin \Phi = 0$

$\Phi = 0$ or π

From (6): $dx = (V - V_w) dt$

From (1): $V \, dt = -\frac{L}{D} dh$

$$\text{Range in a head wind} = -\frac{L}{D} \int_{h_i}^{h_f} dh + \frac{L}{D} \int_{h_i}^{h_f} \frac{V_w}{V} dh \qquad (9)$$

Equation (9) assumes the lift-drag ratio is constant over the whole glide path. From (3):

$$\frac{dh}{V} = \frac{\sqrt{\sigma}}{V_e} dh$$

V_w varies linearly with altitude h (fig. 23):

$$V_w = a + bh$$

(9) becomes:

$$\text{Range} = \frac{L}{D} \left[h_i - h_f + (1/V_e) \int_{h_i}^{h_f} (a + bh) \sqrt{\sigma} \, dh\right] \qquad (10)$$

Substitute (4) into (10):

$$\text{Range} = \frac{L}{D} \left[h_i - h_f + (1.29746/V_e) \int_{h_i}^{h_f} (a + bh) \exp(-h/12683.24) \, dh\right] \quad (h_f \leq h_i)$$

$$= F_1 - F_2$$

where:

$$F_1 = \frac{L}{D}\left[h_i - h_f - 16456\,(\alpha/V_e)\left(\exp(-H_f) - \exp(-H_i)\right)\right]$$

$$F_2 = -2.08715 \times 10^8\, b(L/DV_e)\left[\exp(-H_f) * (H_f + 1) - \exp(-H_i) * (H_i + 1)\right]$$

$H_f = h_f/12683.24$

$H_i = h_i/12683.24$

α = in units of m/s

b = in units of s^{-1}

(b) A constant "head" wind: $b = 0$ ($V_w = \alpha$ = constant)

$$\text{Range} = F_1 = \frac{L}{D}\left[h_i - h_f - 16456\,(\alpha/V_e)\left(\exp(-H_f) - \exp(-H_i)\right)\right]$$

(c) Zero-wind range: $\alpha = b = 0$

$$\text{Range} = \frac{L}{D}(h_i - h_f)$$

(d) If $\Phi = \pi$: $\sin\Phi = 0$

Vector V_g (see sketch) is in the opposite direction. This case will not be considered further.

(e) General case: $\sin\Phi \neq 0$ and $\alpha, b \neq 0$

From (8): $dx = V_w \sin\mu \cot\Phi\, dt - V_w \cos\mu\, dt$

Substitute $dt = -(L/D)(dh/V)$

$$V_w = \alpha + bh$$

$$\text{Range} = \int_{h_i}^{h_f} -(\alpha + bh)\sin\mu\cot\Phi\left(-\frac{L}{D}\frac{dh}{V}\right) + \int_{h_i}^{h_f}(\alpha + bh)\cos\mu\,\frac{L\,dh}{DV} \qquad (11)$$

$\cot\Phi$ also varies linearly with altitude h:

$$\cot\Phi = c + dh$$

Assume the wind direction is constant over the whole glide path, (11) can be integrated to yield the range expression.

$$\text{Range} = -\sin\mu\,(L/DV_e)(F_3 - F_4 - F_5 - F_6) - \cos\mu\,(F_7 + F_2) \qquad (12)$$

where:

$$F_3 = -16456\,\alpha c\,[\exp(-H_f) - \exp(-H_i)]$$

$$F_4 = 2.08715 \times 10^8\,(\alpha d + bc)[\exp(-H_f) * (H_f + 1) - \exp(-H_i) * (H_i + 1)]$$

$$F_5 = 16456\,bd\,[h_f^2 \exp(-H_f) - h_i^2 \exp(-H_i)]$$

$$F_6 = 5.29437 \times 10^{12}\,bd\,[\exp(-H_f) * (H_f + 1) - \exp(-H_i) * (H_i + 1)]$$

$$F_7 = 16456\,(L/D)(\alpha/V_e)[\exp(-H_f) - \exp(-H_i)]$$

$$F_2 = 2.08715 \times 10^8\,(L/D)(b/V_e)[\exp(-H_f) * (H_f + 1) - \exp(-H_i) * (H_i + 1)]$$

$$H_f = h_f/12683.24$$

$$H_i = h_i/12683.24$$

Range in a Climbing Flight:

$$\text{Rate of climb} = \text{ROC} = \frac{dh}{dt}$$

$$dt = dh/\text{ROC}$$

(a) Head wind: $\Phi = 0$

$$V_g = \frac{dx}{dt} = V - V_w$$

$$V = V_e/\sqrt{\sigma}\ ;\ V_w = \alpha + bh$$

$$dx = (V_e/\sqrt{\sigma} - \alpha - bh)(dh/\text{ROC})$$

Assume the rate of climb is constant over the climb portion of the flight, the above expression can be integrated with (4) substituted for $\sqrt{\sigma}$:

$$\text{Climb range} = \frac{12683.24\ V_e}{1.29746 * ROC}\left[\exp(H_f) - \exp(H_i)\right] - G_l$$

$$= 9775\ (V_e/ROC)[\exp(H_f) - \exp(H_i)] - G_l$$

where:

$$H_f = h_f/12683.24$$

$$H_i = h_i/12683.24 \qquad (h_i < h_f)$$

$$G_l = (\alpha/ROC)(h_f - h_i) + (\frac{b}{2} * ROC)(h_f^2 - h_i^2)$$

(b) Zero wind climb range:

$\alpha = b = 0$

Climb range = $9775\ (V_e/ROC)[\exp(H_f) - \exp(H_i)]$

(c) Constant head wind: $b = 0$

Climb range = $9775\ (V_e/ROC)[\exp(H_f) - \exp(H_i)] - (\alpha/ROC)(h_f - h_i)$

H_f and H_i are defined above.

(d) General case: $\Phi \neq 0$

α and $b \neq 0$

From (8):

$$dx = V_w \sin \mu \cot \Phi\ dt - V_w \cos \mu\ dt$$

where $dt = dh/ROC$

$V_w = \alpha + bh$

$\cot \Phi = c + dh$

$$dx = (\alpha + bh)(c + dh) \sin \mu \frac{dh}{ROC} - (\alpha + bh) \cos \mu \frac{dh}{ROC}$$

Assuming a constant rate of climb and constant wind direction:

$$\text{Climb range} = \frac{\sin \mu}{ROC} \int_{h_i}^{h_f} (\alpha c + \alpha dh + bch + bdh^2)\ dh$$

$$- \frac{\cos \mu}{ROC} \int_{h_i}^{h_f} (d + bh)\, dh \qquad (13)$$

$$= G_2 - G_3$$

where:

$$G_2 = \frac{\sin \mu}{ROC} \left[\alpha c \, (h_f - h_i) + \frac{\alpha d + bc}{2} \, (h_f^2 - h_i^2) + \frac{bd}{3} \, (h_f^3 - h_i^3) \right]$$

$$G_3 = \frac{\cos \mu}{ROC} \left[\alpha \, (h_f - h_i) + \frac{b}{2} \, (h_f^2 - h_i^2) \right]$$

$$(h_f > h_i)$$

The total range per station (fig. 32) is the sum of (12) and (13) for the general case.

REFERENCES

1. Earhart, R. W.; Kuhner, M. B.; Madigan, J. A.; and Ruck, G. T.: Applications of a High-Altitude Powered Platform, Battelle Columbus Laboratories Final Report, September 1977.

2. Wessel, P. R.; and Petrone, F. J.: HASPA Design and Flight Test Objectives. AIAA Paper No. 75-924, July 1975.

3. Boucher, R. J.: "Project Sunrise." AIAA Paper No. 79-1264, June 1979.

4. MacCready, P. B.; Morgan, W. R.; Burke, J. D.; and Lissaman, P. B. S.: "Sun-Powered Aircraft Design." AIAA Paper No 81-0916, May 1981.

5. Parks, R. W.; Hall, D. W.; Dimiceli, E. V.; and Fortenbach, C. D.: "A Preliminary Study of Solar Powered Aircraft and Associated Power Trains." NASA CR-3699, December 1983.

6. Reed, Arthur: "Brassey's Unmanned Aircraft." Brassey's Publishers Limited, 1979.

7. Liu, G. C.; Morris, C. E.; and Koenig, R. W.: "Performance of High-Altitude, Long-Endurance, Turboprop Airplanes Using Conventional or Cryogenic Fuels." NASA TM 84534, January 1983.

8. Sinko, J. W.: "High Altitude Powered Platform Cost and Feasiblity Study." Stanford Research Institute, SRI Project 5655-502, Contract NASW 2962, October 1977.

9. Heyson, H. H.: "Initial Feasibility Study of a Microwave-Powered Sailplane as a High-Altitude Observation Platform." NASA TM 78809, December 1978.

10. Morris, C. E. K.: "Parametric Study of Microwave-Powered High-Altitude Airplane Platforms Designed for Linear Flight." NASA TP 1918, November 1981.

11. Graves, E. B.: "The Feasibility of a High-Altitude Aircraft Platform with Consideration of Technological and Societal Constraints." NASA TM 84508, June 1982.

12. Morris, C. E. K.: "Design Study for Remotely Piloted, High-Altitude Airplanes Powered by Microwave Energy." AIAA Paper No. 83-1825, July 1983.

13. Brown, W. C.: "The Technology and Application of Free-Space Power Transmission by Microwave Beam." Proceedings of the IEEE, Vol. 62, No. 1, January 1974.

14. Brown, W. C.: "Design Study for a Ground Microwave Power Transmission System for Use with a High-Altitude Powered Platform." NASA Contractor Report 168344, June 1983.

15. Goubau, G.: "Microwave Power Transmission from an Orbiting Solar Power Station." The Journal of Microwave Power, Vol. 5, No. 4, 1970.

16. Wheeler, G. J.: "Radar Fundamentals." Prentice Hall Series in Electronic Technology, 1967.

17. Angelakos, D. J.; and Everhart, T. E.: "Microwave Communications." McGraw-Hill Electrical and Electronic Engineering Series, 1968.

18. Silver, S.: "Microwave Antenna Theory and Design." First edition, McGraw-Hill, 1949.

19. Toomay, J. D.: "Radar Principles for the Non-Specialist." Lifetime Learning Publications, 1982.

20. Brown, W. C.: "Microwave-Powered Aerospace Vehicles." Microwave Power Engineering, vol. 2, Academic Press, 1968.

21. Brown, W. C.: "Design Definition of a Microwave Power Reception and Conversion System for Use on a High Altitude Powered Platform." NASA Contractor Report 156866, May 1981.

22. Collin, R. E.; Zucker, F. J.: "Antenna Theory Part 2." McGraw-Hill Inter-University Electronics Series, vol. 7, 1969.

23. Kaufman, J. W.: "Terrestrial Environment (Climatic) Criteria Guidelines for Use in Aerospace Vehicle Development, 1977 Revision." NASA Technical Memorandum 78118, November 1977.

24. Strganac, T. W.: "Wind Study for High Altitude Platform Design." NASA RP-1044, December 1979.

25. Klass, P. J.: "Powerful Magnets Find Aerospace Role." Aviation Week and Space Technology, August 8, 1977.

26. Goldsmith, P.; Reppucci, G. M.: "Advanced Photovoltaic Power Systems." AIAA Paper No. 77-506, March 1977.

27. "The 1982 Goddard Space Flight Center Battery Workshop." NASA Conference Publication 2263, November 1982.

28. Selman, J. R.: "Fuel Cells: Fundamentals and Types - Unique Features." Symposium Papers Fuel Cells Technology Status and Applications, Institute of Gas Technology, November 1981.

29. Schubert, F. H.; Reid, M. A.; Martin, R. E.: "Alkaline Regenerative Fuel Cell Systems for Energy Storage." Proceedings of the International Energy Conversion Engineering Conference, 1981.

30. Badcock, C. C.: "High Power for Space Systems." Aerospace America, June 1984 Issue.

31. Keckler, C. R.: "Integrated Power/Attitude Control System." Integrated Flywheel Technology 1983, NASA Conference Publication 2290, August 1983.

32. Coates, Andrew: "Jane's World Sailplane and Motor Gliders." Flying Books, Ziff-Davis Publishing Company, Great Britain, 1978.

33. Sands, L. G.; and Dumas, K. L.: "Microwave Systems Planning." Hayden Book Company, New York, 1967.

34. Perkins, C. F.; and Hage, R. E.: "Airplane Performance Stability and Control " John Wiley and Sons, New York.

35. Sinko, J. W.: "Circling Flight in Wind for HAPP Aircraft." SRI Project 7345. August 1978.

TABLE 1.- REQUIRED RECEIVING APERTURE AREA

Transmission Efficiency	Amount of Power Radiation (KW)	Required Aperture Area (ft^2)
0.8	500	139,931
0.8	1000	279,862
0.8	1500	419,783

TABLE 2.- TRANSMISSION EFFICIENCIES

	Efficiency
60-Hz to microwave conversion	0.6
Transmission from generator to rectenna	0.95 (max.)
Rectenna collection and rectification	0.90

TABLE 3.- RANGE OF VALUES FOR COST MODELS

	Phased Array	Parabolic Reflector
Area unit cost	9.3 $/ft^2	0.6 - 1.2 $/ft$^{2.5}$
Equipment cost $/KW	200	200
Power cost (yearly) $/KW	380	380

TABLE 4.- DATA ON GROUND POWER STATION

	Phased Array	Parabolic Reflector
Diameter	240 ft	204 ft
Wavelength	0.40 ft	same
Scan Angle	± 10° in all directions	180°
Accuracy (at 20 km)	0.003°	same

TABLE 5.- POWER TRANSMISSION ATTENUATION FACTORS

Factor	Parabolic "Dish"	Phased Array	Analytical Expression
Range, wavelength Aperture areas	x	x	"Radar-Range" equation (Appendix A)
Amplitude and Phase Distributions	x	x	Gain expressions (see Appendix A)
Transmitter geometry (1-D or circular)	x	x	$\left(\frac{\sin u}{u}\right)^2$ or $\left[\frac{J_1(u)}{u}\right]^2$
Beam deflection angle θ_o (measured from vertical axis)	o	x	$\cos^2 \theta_o$
Climbing flight	x	x	$\sin \theta_o + \gamma$) (fig. 22b)
Turning flight	x	x	$\cos \theta_o + \phi$ (fig. 22a)

o = no effect
x = affected

TABLE 6.- A COMPARISON OF DIFFERENT ENERGY CONVERTERS

Energy Converter	Specific Weight (lb/hp)
70-HP diesel	10.71
70-HP, 2-cycle gas	1.42
Turboprop PT6A-41, 643 HP	0.59
Samarium-Cobalt motor (8600 RPM)	0.57

TABLE 7.- MOTOR DESIGNS COMPARISON

Type	Samarium-Cobalt	Samarium-Cobalt
Power	35-HP max	35-HP max
Speed	8600 RPM	8600 RPM
Conductor	Copper	Diffused graphite
Frame	Steel	Copper
Stator-rotor	Steel	Metglas
Efficiency	0.93	0.93
Specific weight	1.71 lb/hp	0.57 lb/hp

TABLE 8.- PROPULSION DESIGN PARAMETERS

Electric motor	
Type	Advanced Sa-Co, brushless
Specific power	1308 W/lb
Efficiency*	0.93
Gear	
Type	Reduction
Specific power (ref. 12)	2461 W/lb
Efficiency (ref. 12)	0.99
System (gear and motor)	
Specific power	849 W/lb
Efficiency*	0.92
Propeller	
Number of blades	3
Diameter, ft	24
RPM	450
Reynolds number	0.1×10^6
Efficiency*	0.85

*At design conditions

TABLE 9.- POWER PROCESSING TECHNOLOGY

Function	Specific Power	
	Present (w/lb)	1985 (w/lb)
Payload	45	65
Propulsion	225	250

TABLE 10.- SPECIFIC ENERGY OF ELECTROCHEMICAL SYSTEM

SYSTEM	Gravimetric Energy Density W-HR/Kg	Volumetric Energy Density W-HR/Dm^3
Ni-Cd	30-35	100
Ag-Zn	90-120	260
Ag-Cd	40-60	120
Ni-H_2	45-55	40
Ag-H_2	70-80	50

TABLE 11.- LABORATORY FLYWHEEL CHARACTERISTICS

Speed range	17,500-35,000 RPM
Energy capacity	1.5 KW-HR
Rotor weight	50.8 Kg
Rotor energy density	29.5 W-HR/KG
Charge/discharge duration	50/40 minutes
Assembly weight	78.5 Kg
Overall efficiency	0.52

TABLE 12.- BATTERY CAPABILITY ($Ni-H_2$)

Storage energy, W-hr/kg	55
Depth of discharge (6,000 cycles)	0.80
Usable specific energy, W-hr/kg	44
Endurance, hr	1.0 or less

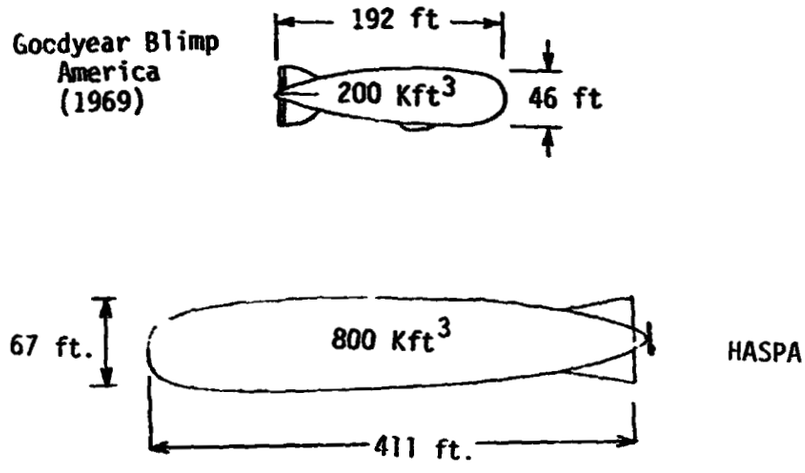

Figure 1.- HASPA configuration vs. "Goodyear" blimp.

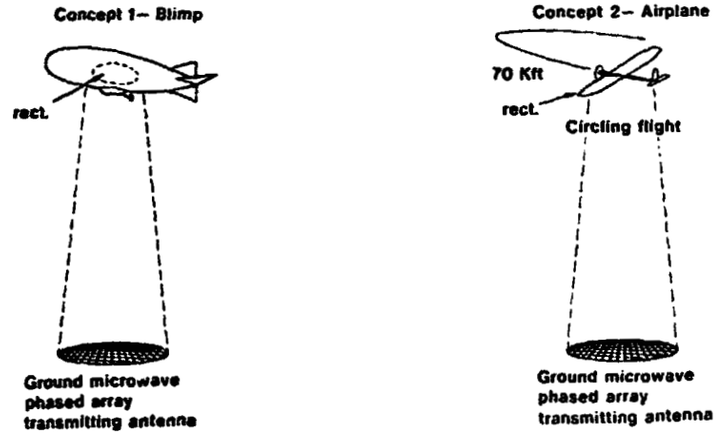

Figu· - High-altitude powered platform concepts.

Figure 3.- Elements of a microwave transmission system.

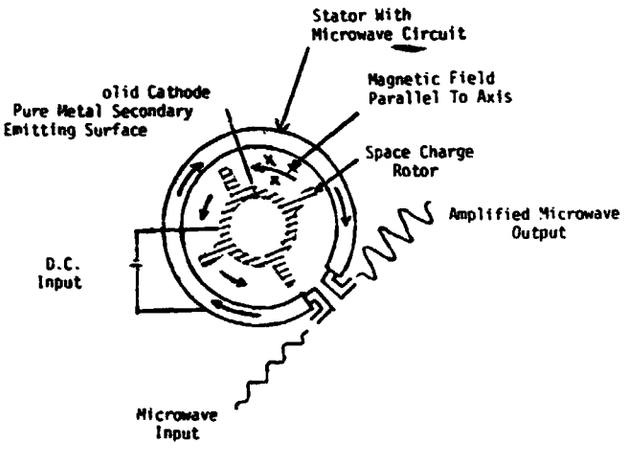

Figure 4.- Principle of operation of the amplitron. Rotating spokes of space charge induce currents into the microwave circuit and provide efficient amplification of the input signal.

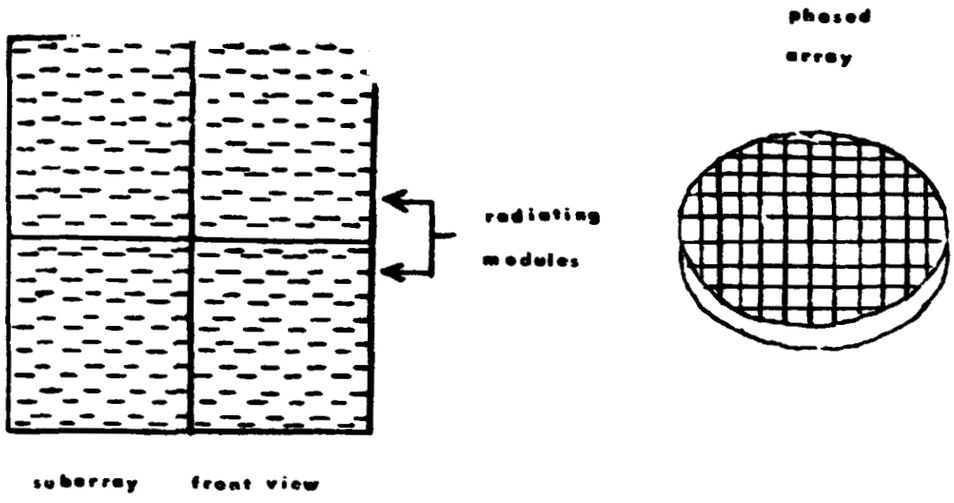

Figure 5.- Individual modules (left) and circular array (right).

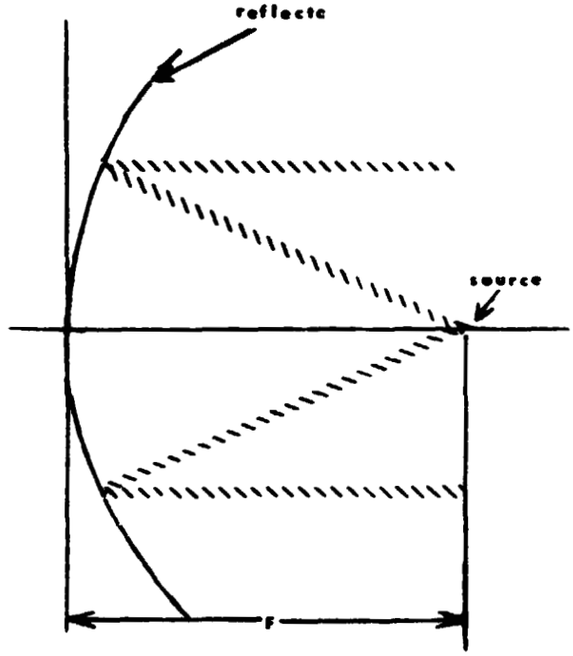

Figure 6.- Paraboloidal reflector with focal length F.

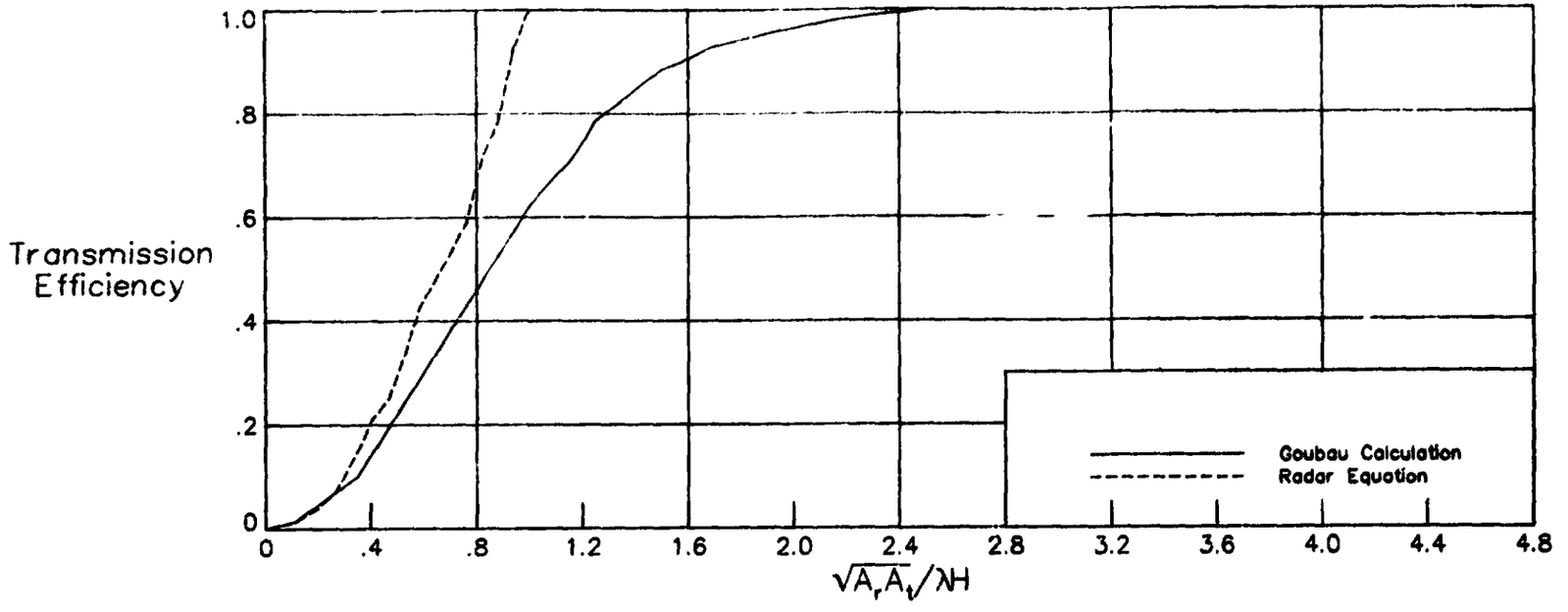

Figure 7.- Efficiency vs. aperture areas, range, and wavelength.

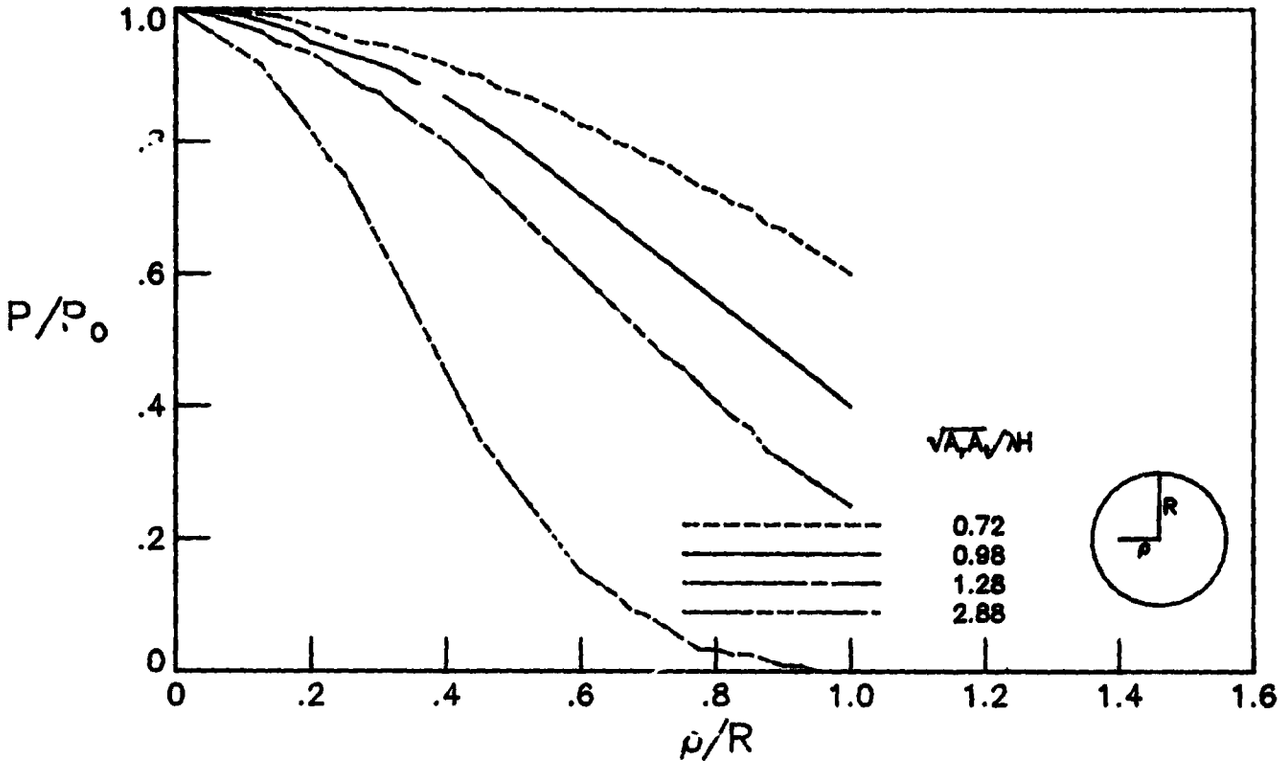

Figure 8.- Illumination distributions across the face of the circular transmitter.

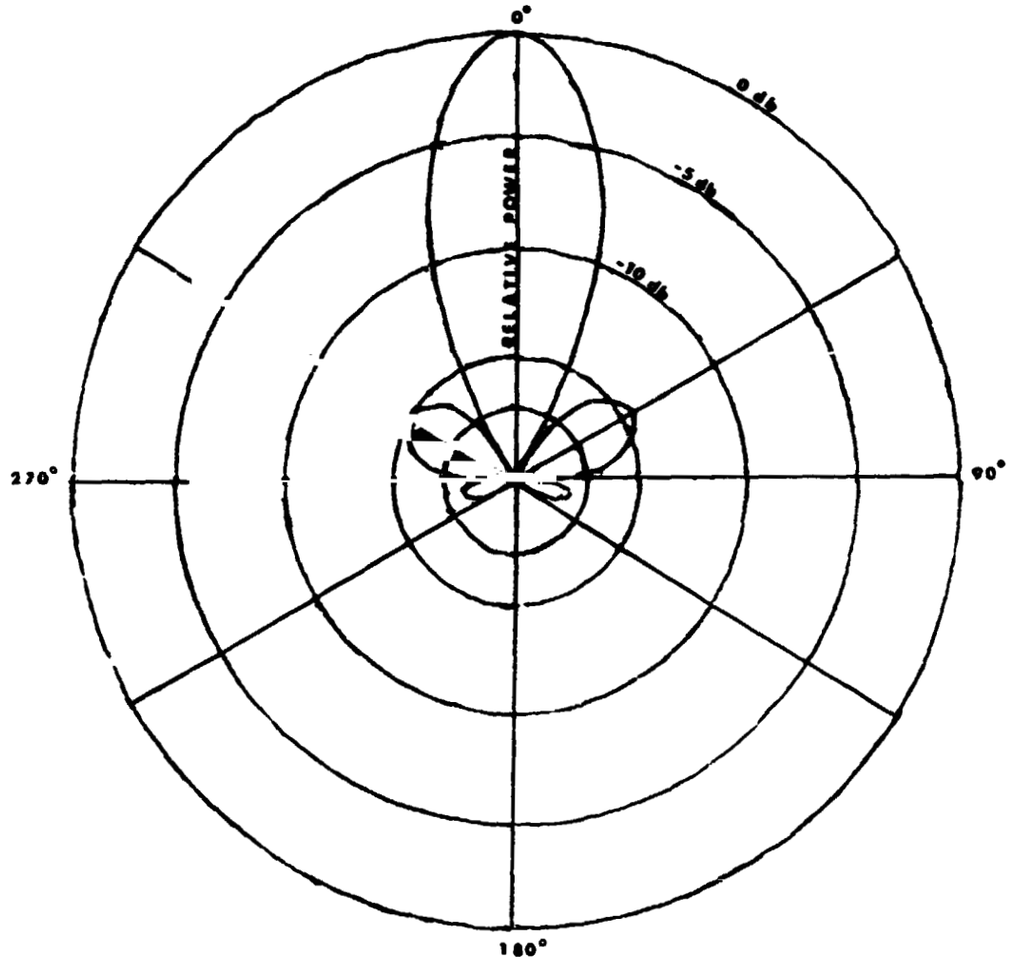

Figure 9.- Beam pattern in polar coordinates.

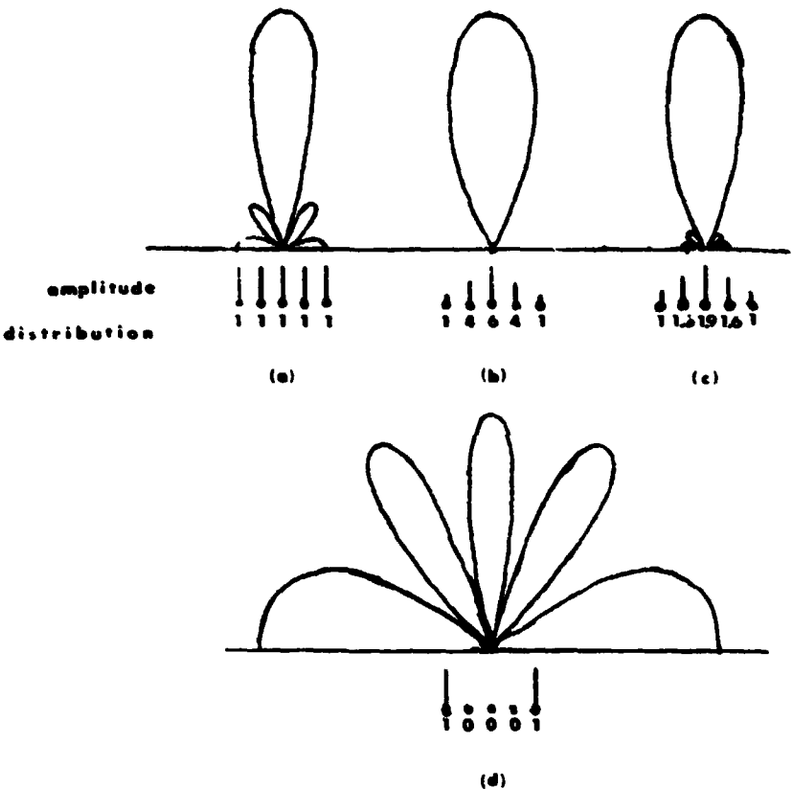

Figure 10.- Tapered illumination effect on the radiation pattern of arrays. (a) Uniform; (b) Binomial; (c) Optimum; and (d) End-excited.

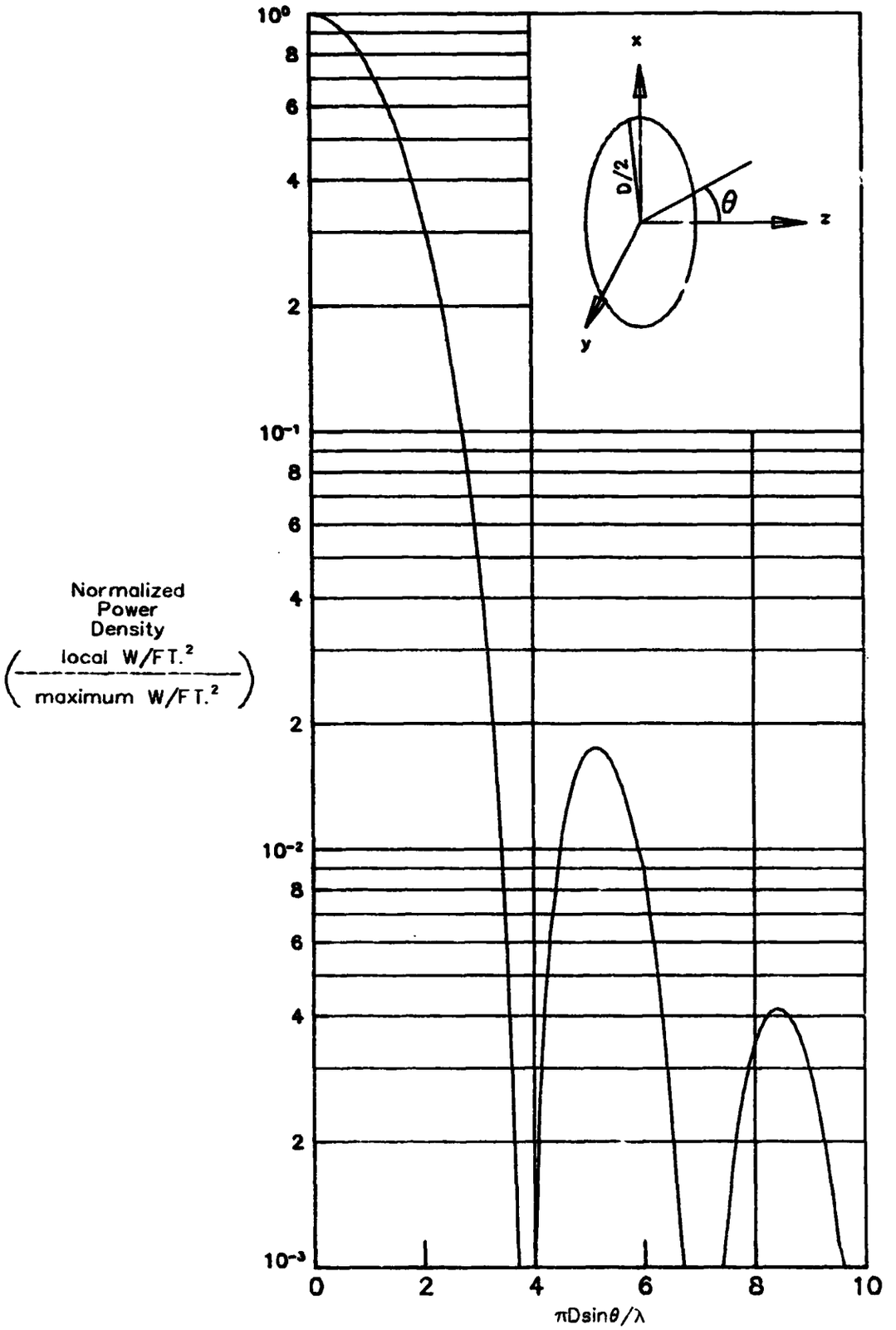

Figure 11. - Far-field pattern of a circular aperture.

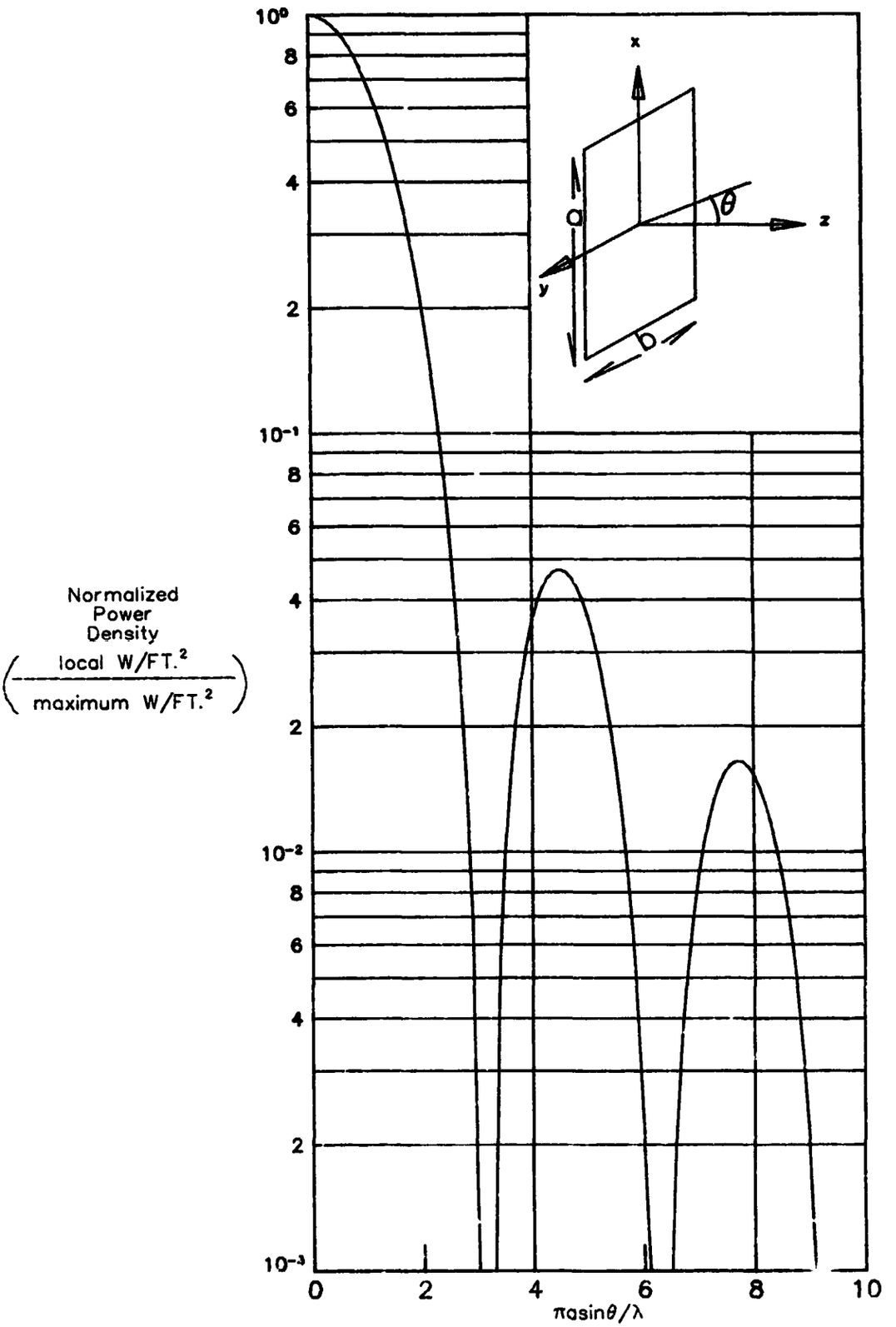

Figure 12.- Far-field pattern of a rectangular aperture.

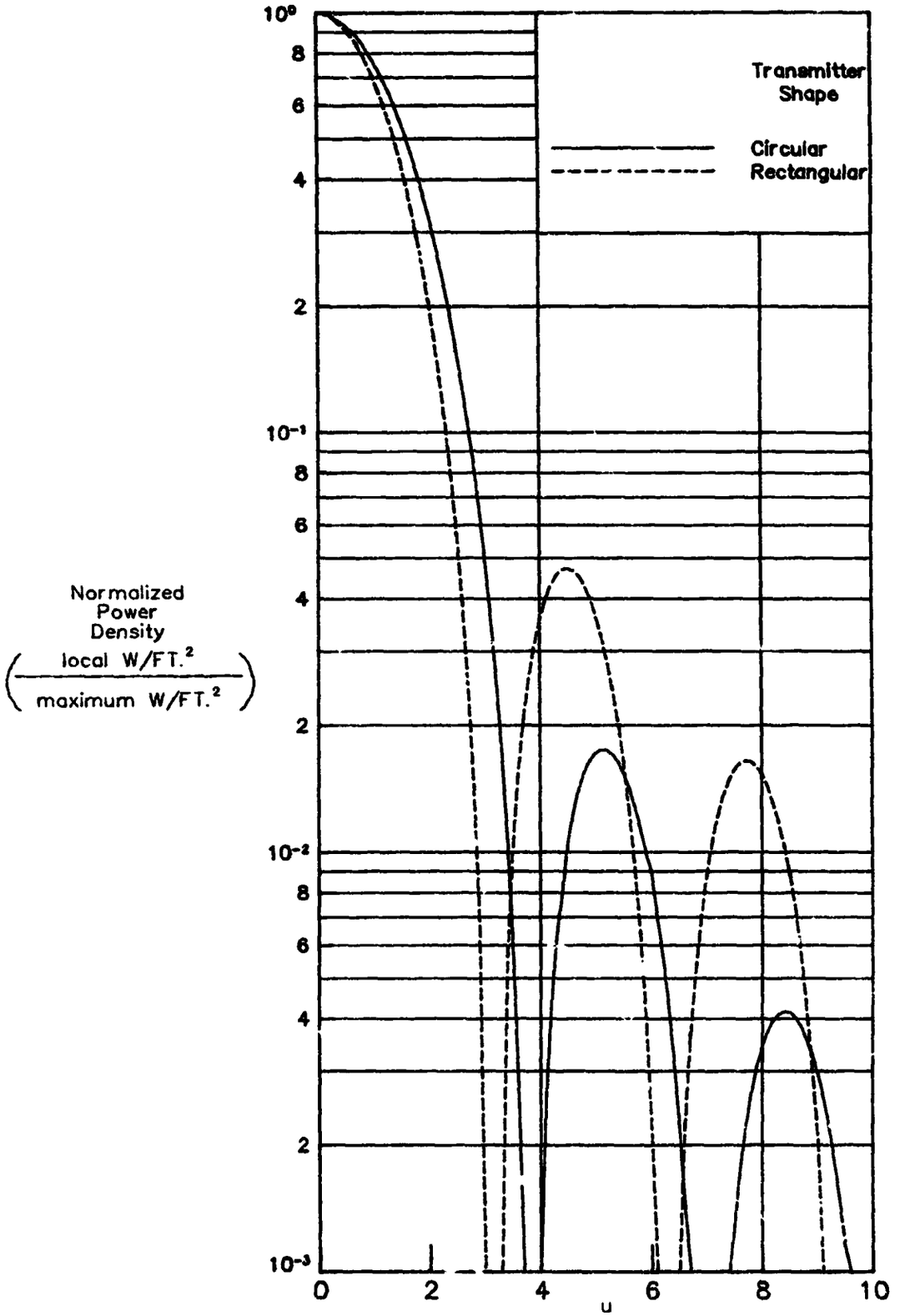

Figure 13.- Comparison of patterns from circular and one-dimensional apertures.

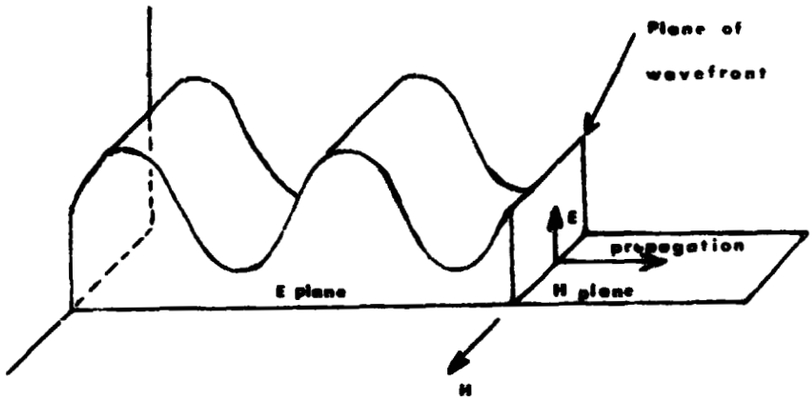

Figure 14.- Linear polarization of electromagnetic waves.

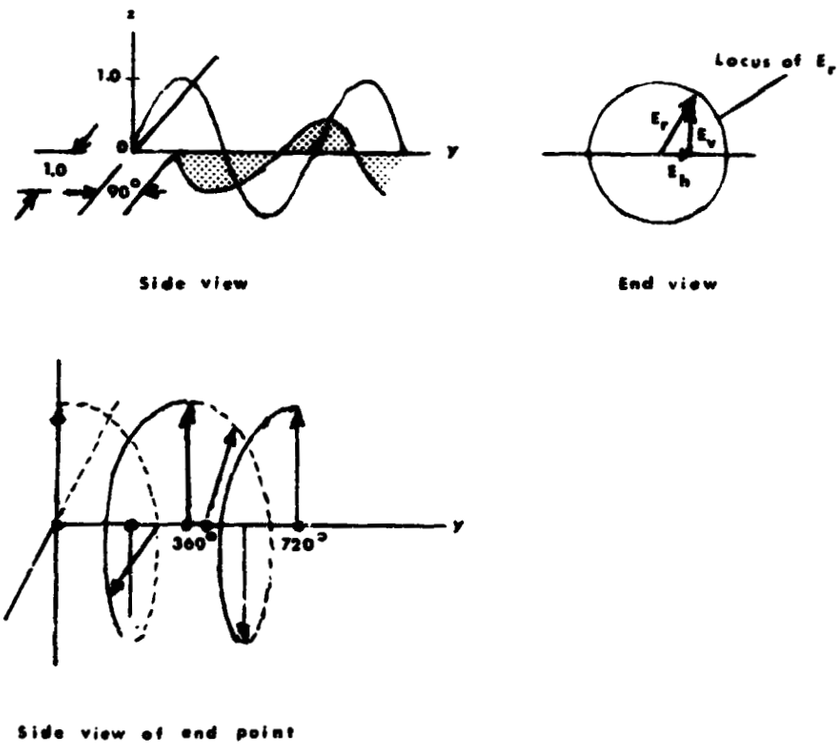

Figure 15.- Circularly polarized waves.

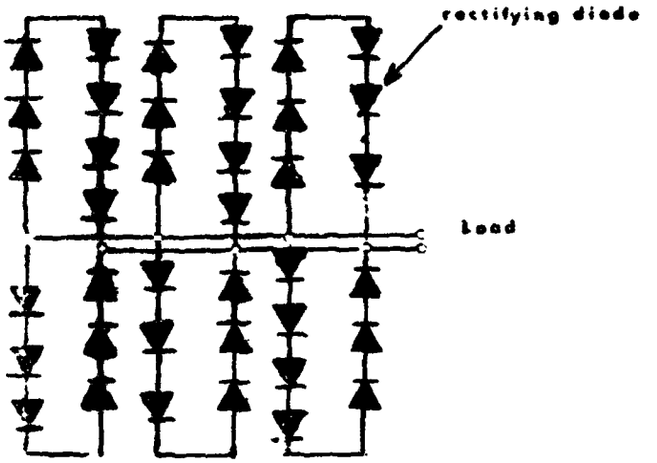

Figure 16.- Schematic drawing of a "string-type" rectenna.

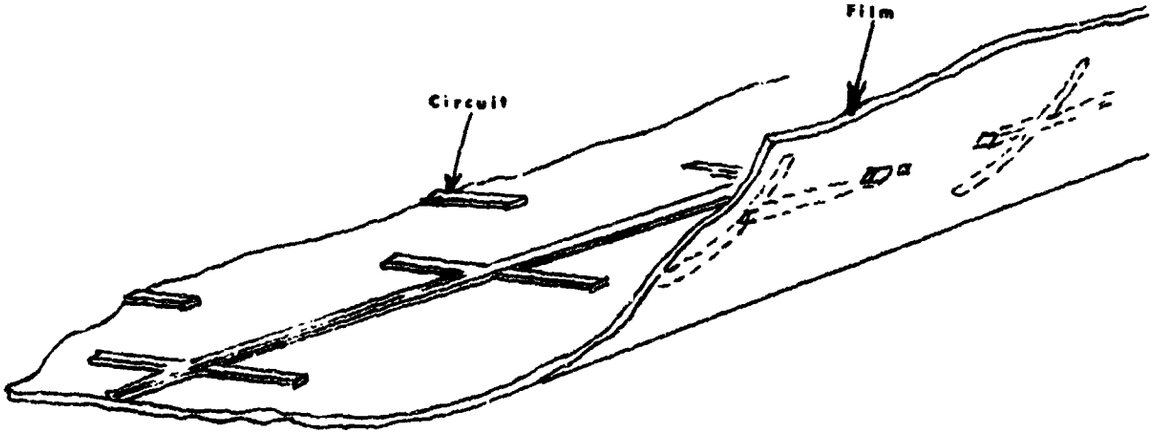

Figure 17.- Printed-film rectenna.

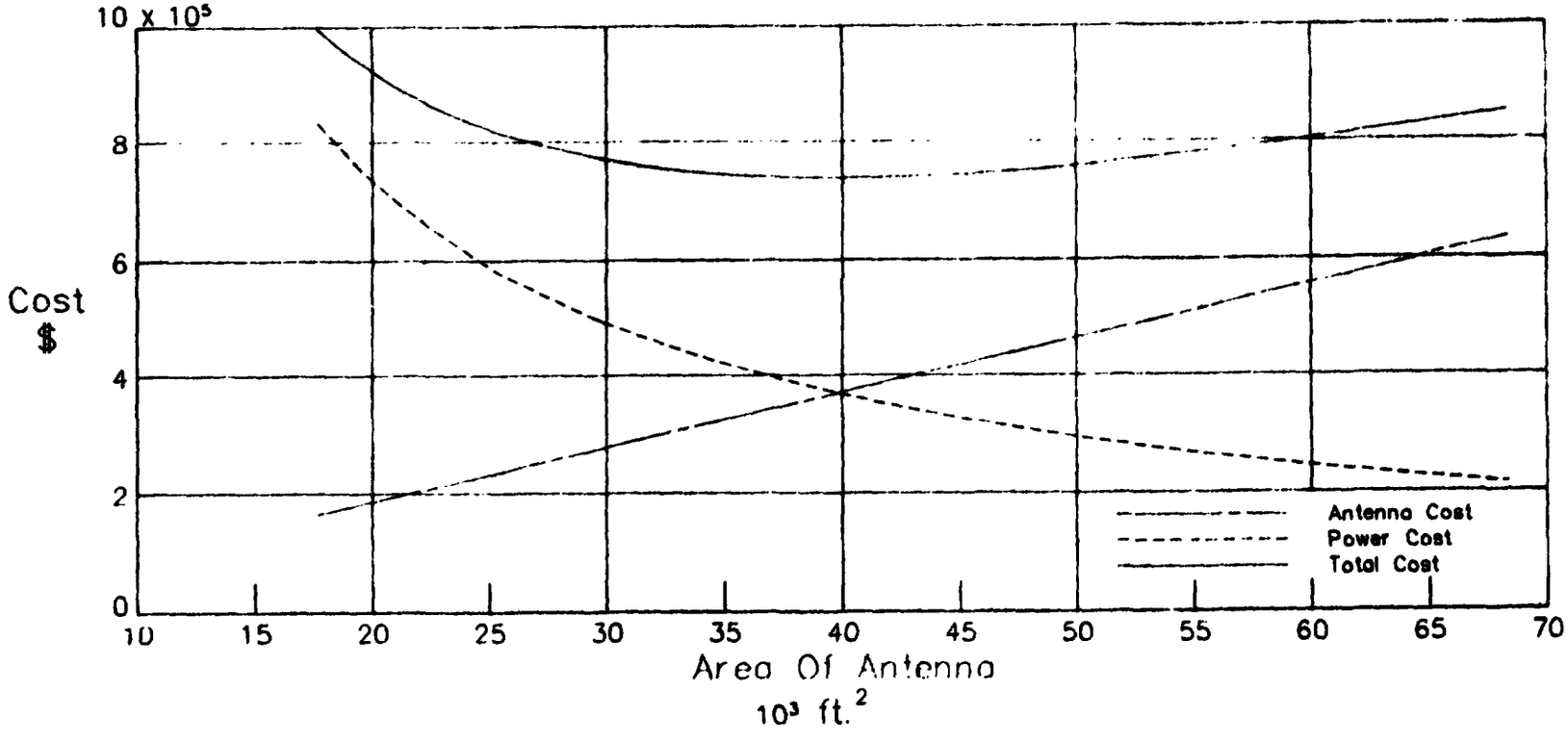

Figure 18.- Life-cycle cost as function of phased-array aperture area.

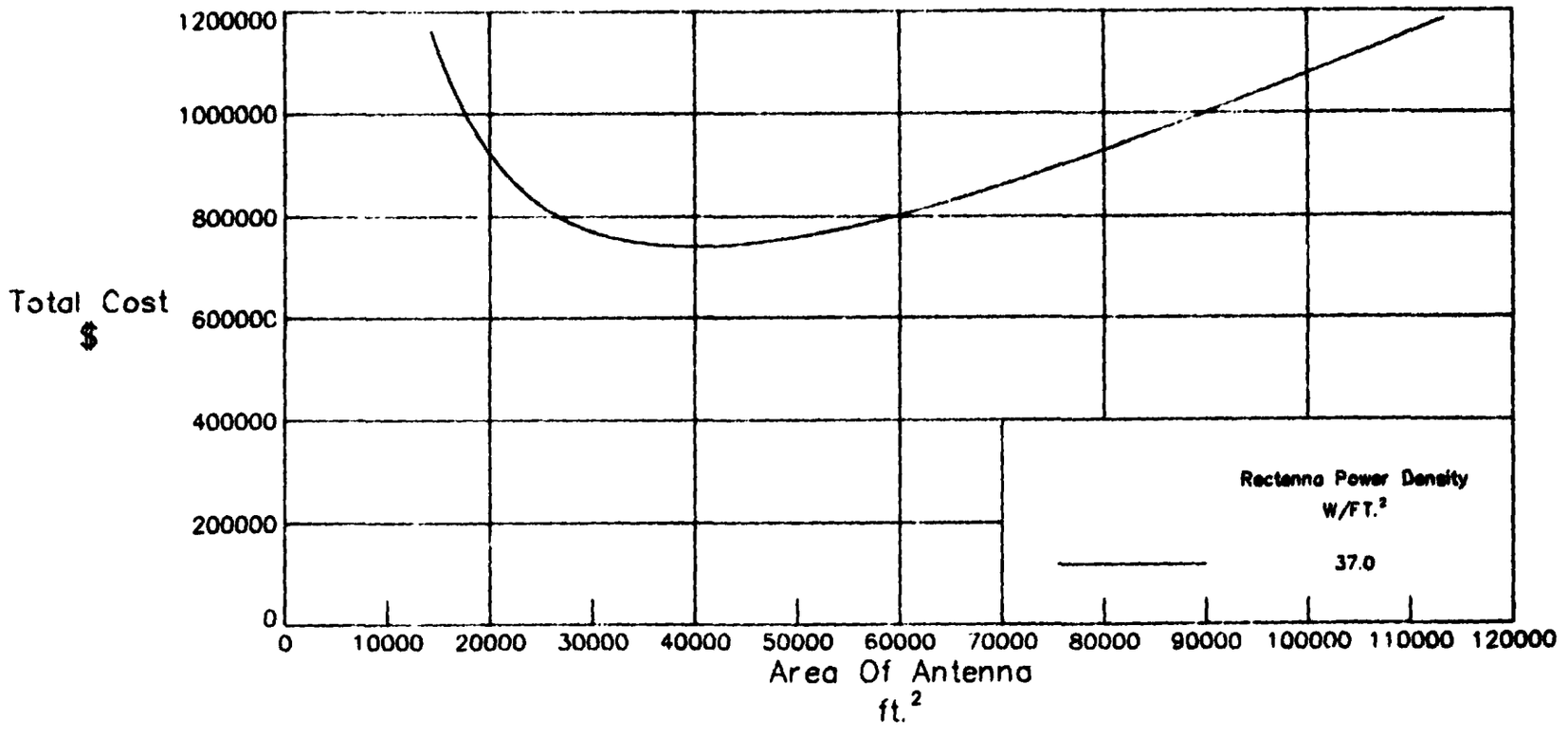

Figure 19.- Life-cycle cost for a specific value of rectenna power density.

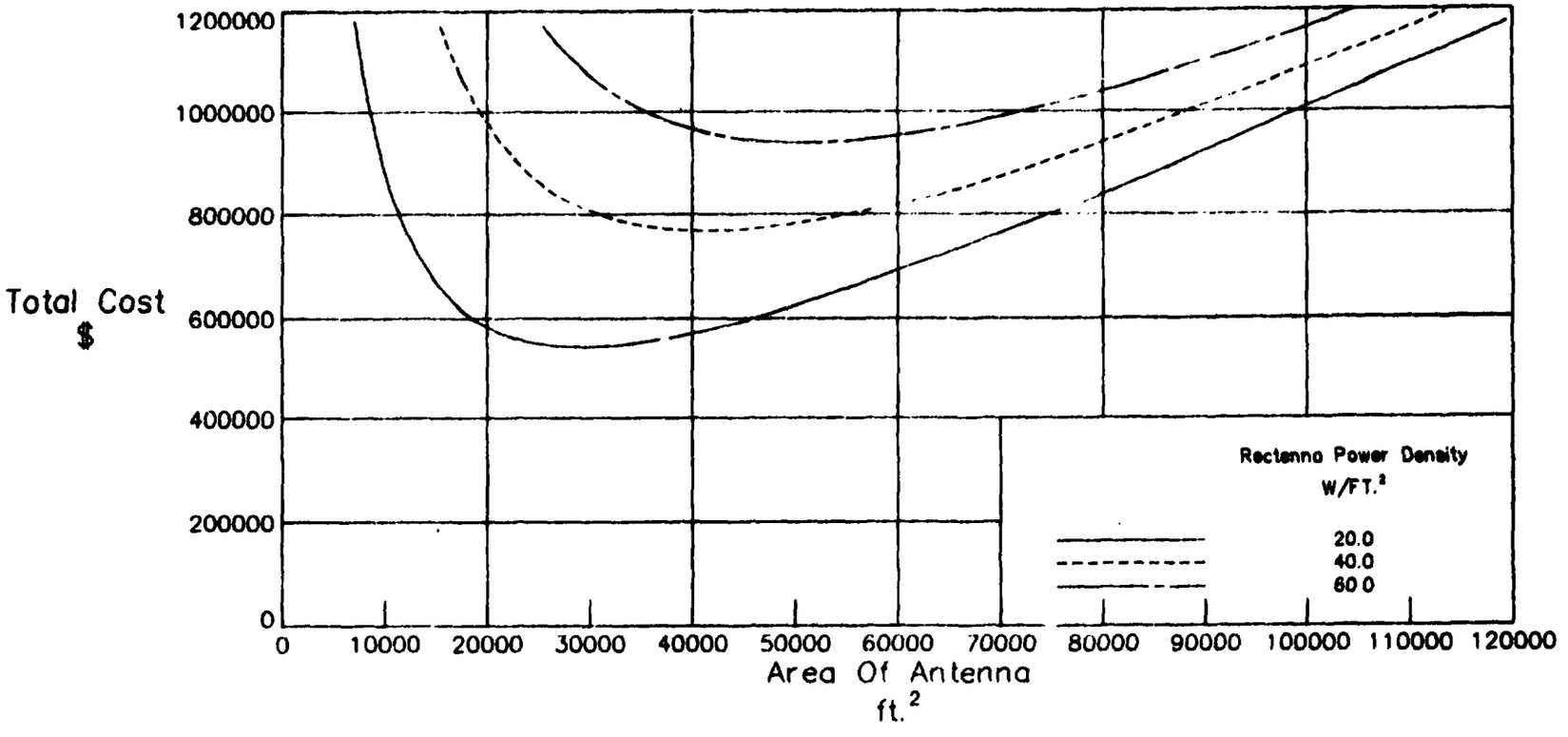

Figure 20.- Power density effect on cost.

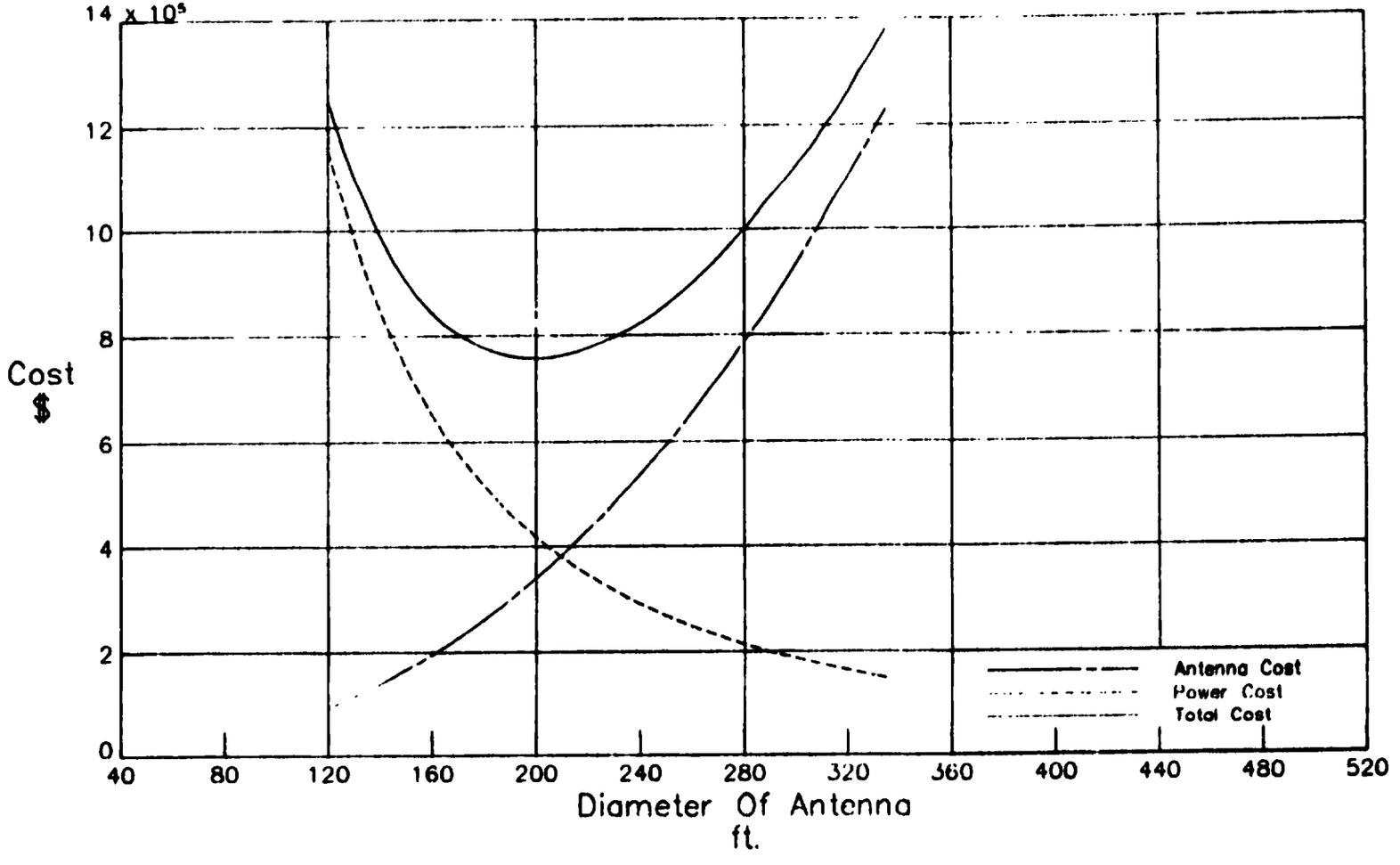

Figure 21.- Cost model for a parabolic "dish."

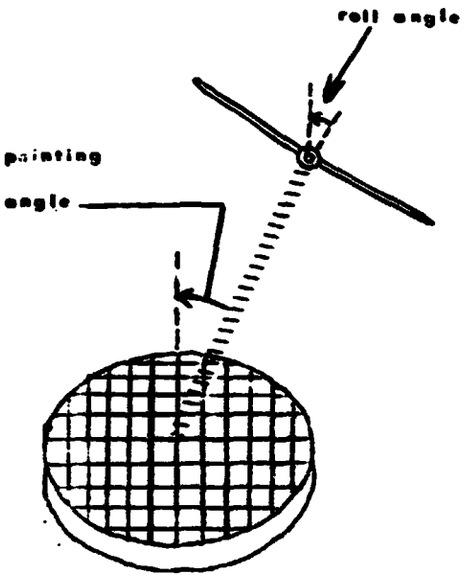

Figure 22a.- Attenuation factors in turning flight.

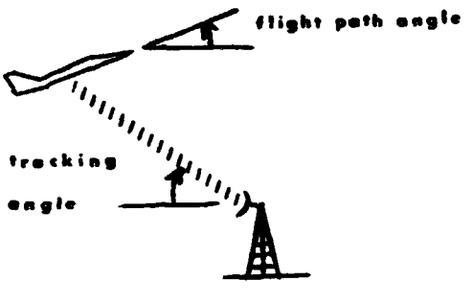

Figure 22b.- Attenuation factors in climbing flight.

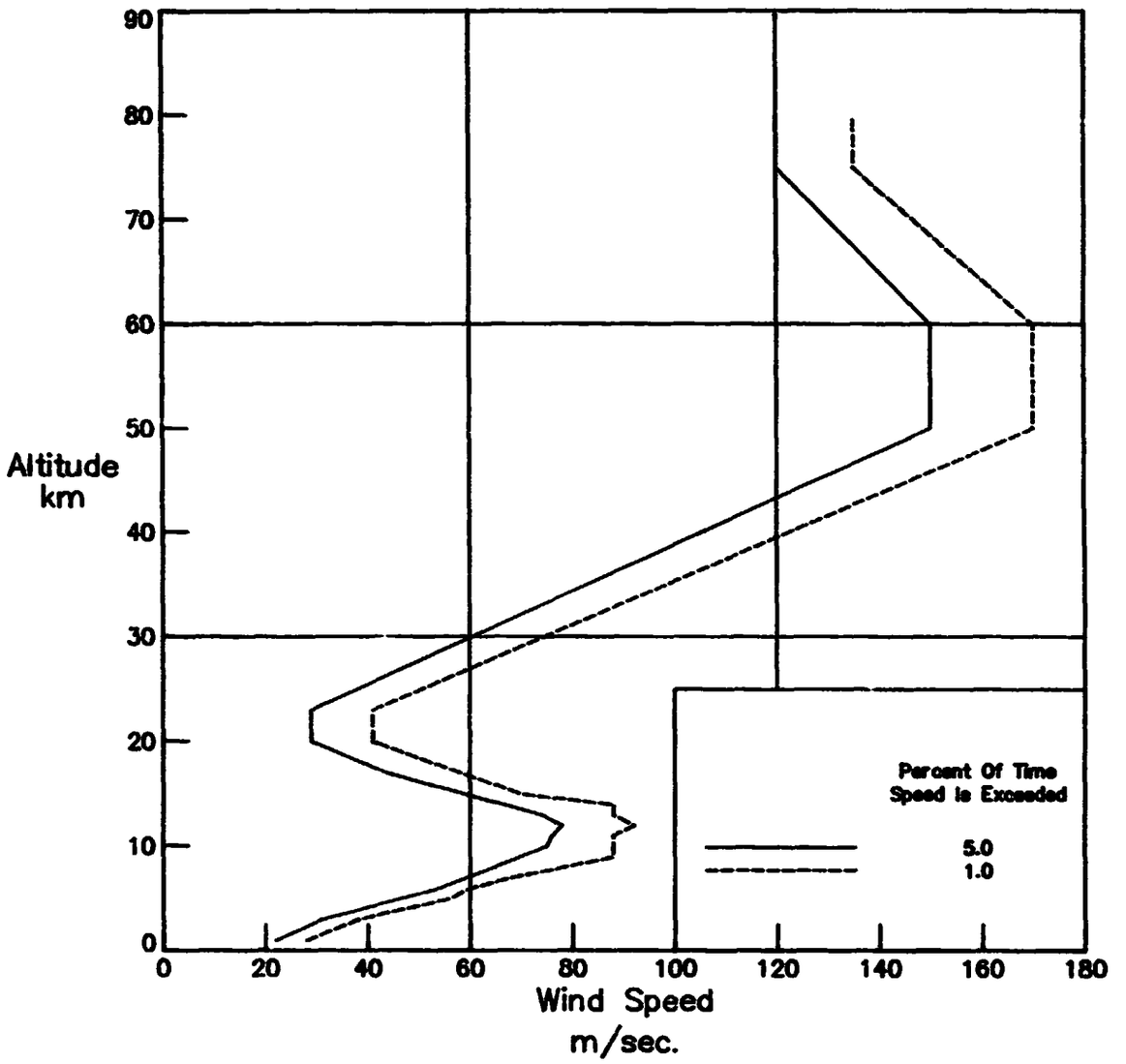

Figure 23.- Steady-state, scalar wind-speed envelopes.

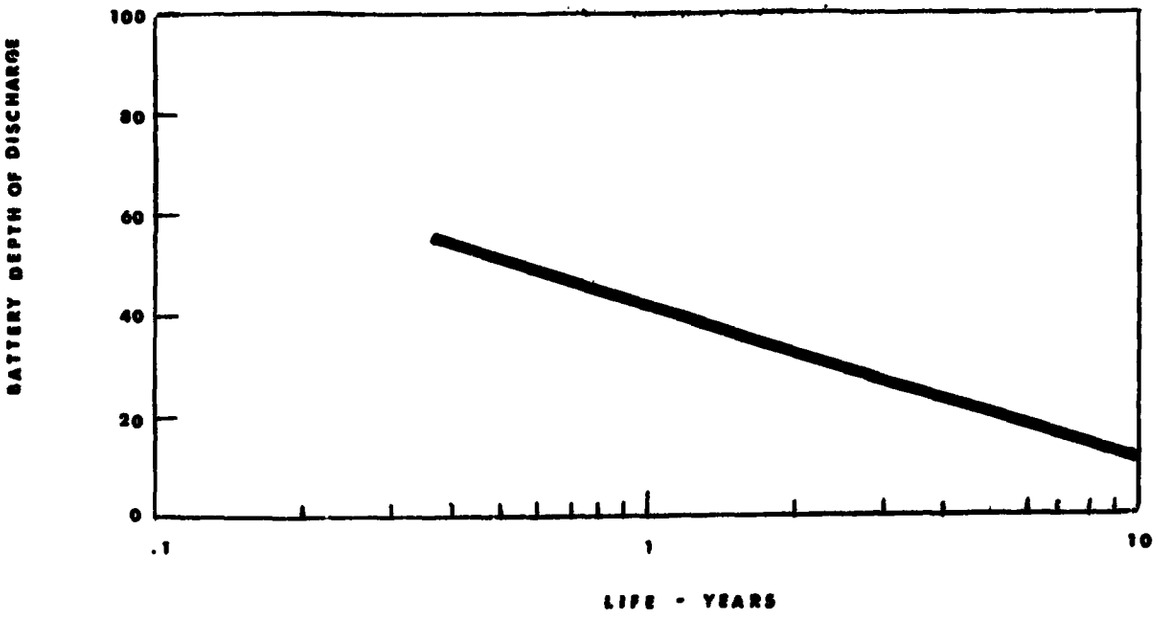

Figure 24.- Demonstrated capability of nickel-cadmium battery. (ref. 28).

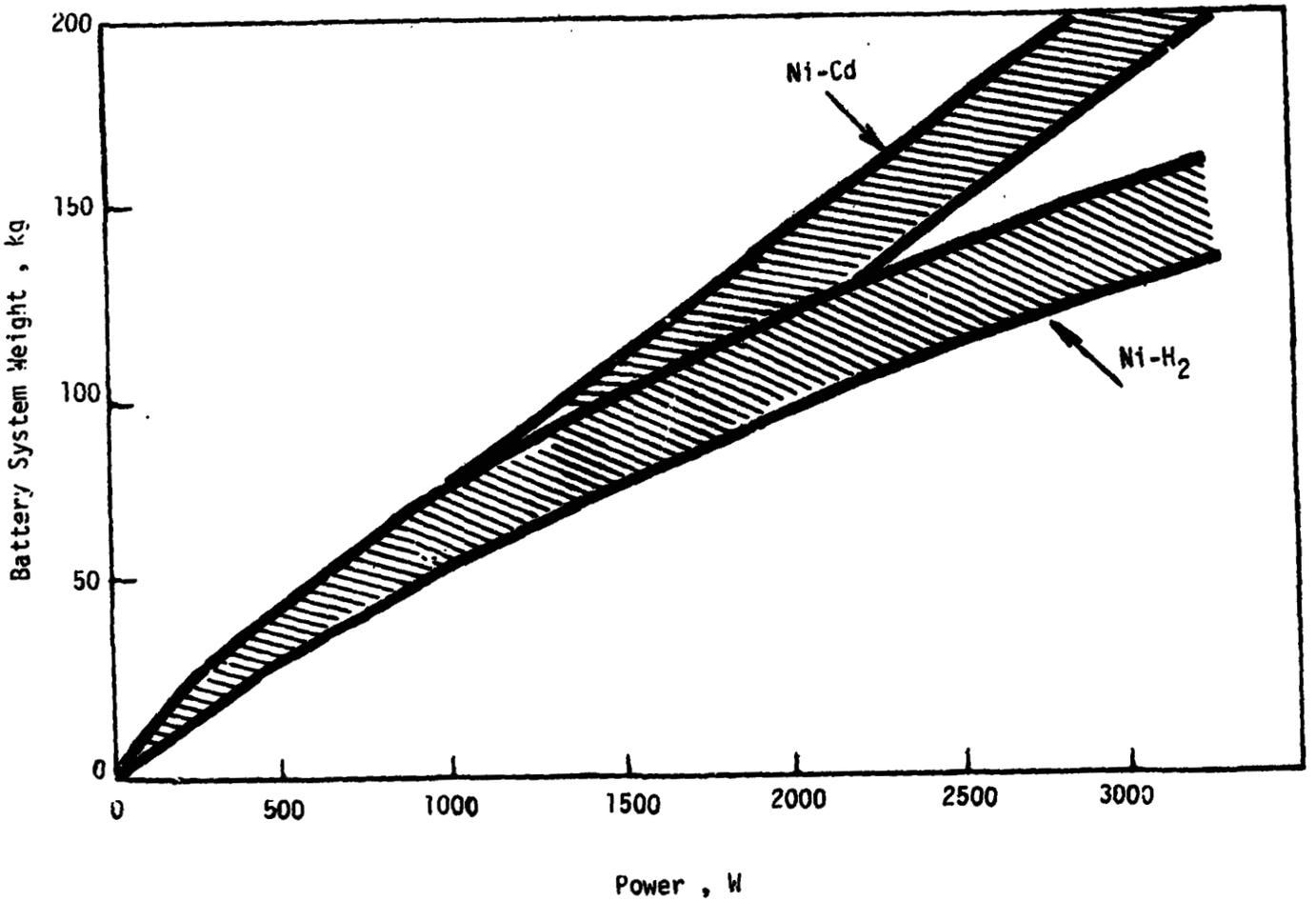

Figure 25.- Weight vs. power comparisons between N_i-H_2 and N_i-Cd batteries.

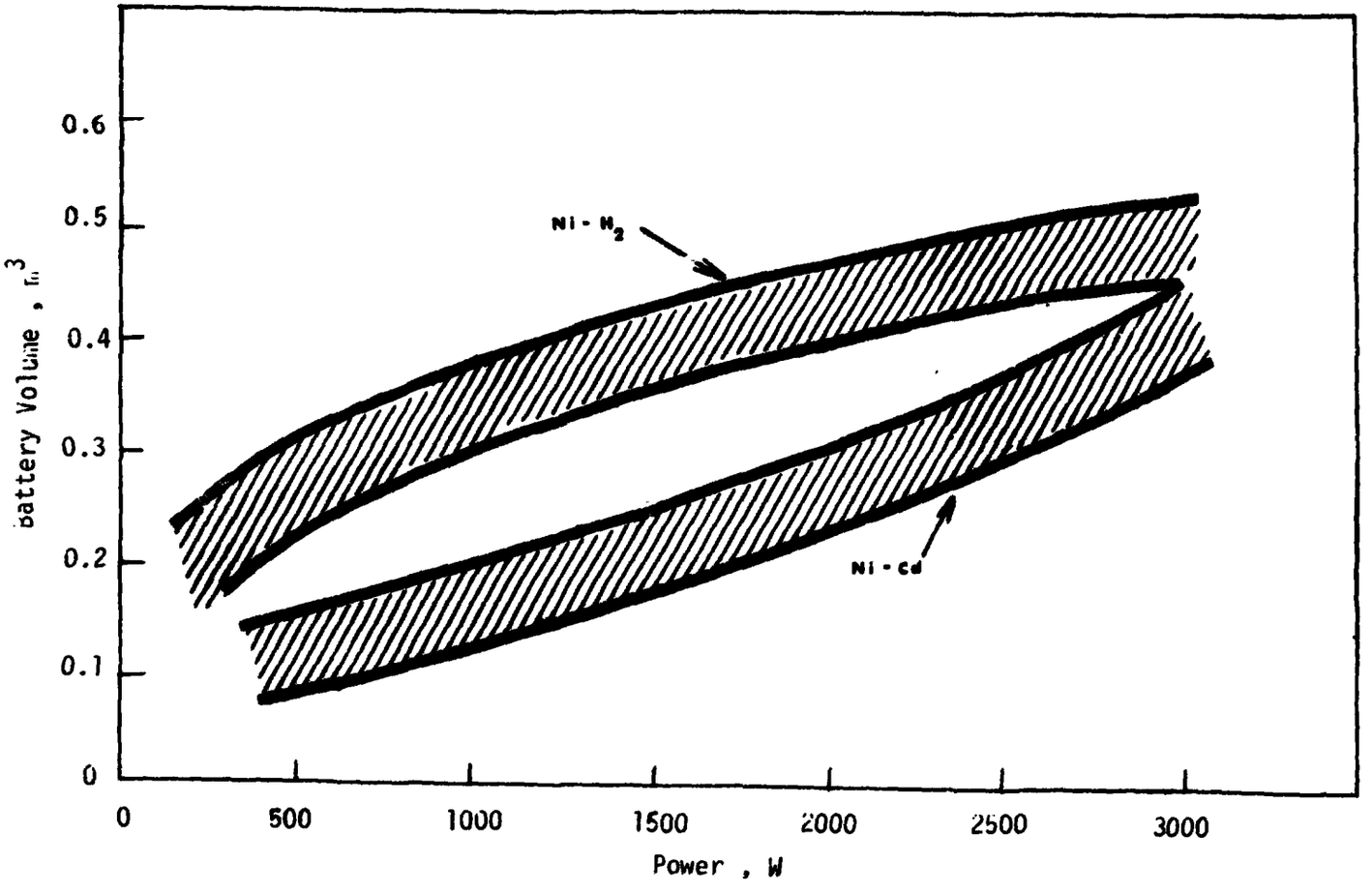

Figure 26.- Volume vs. power comparison between N_i-H_2 and N_L-Cd batteries.

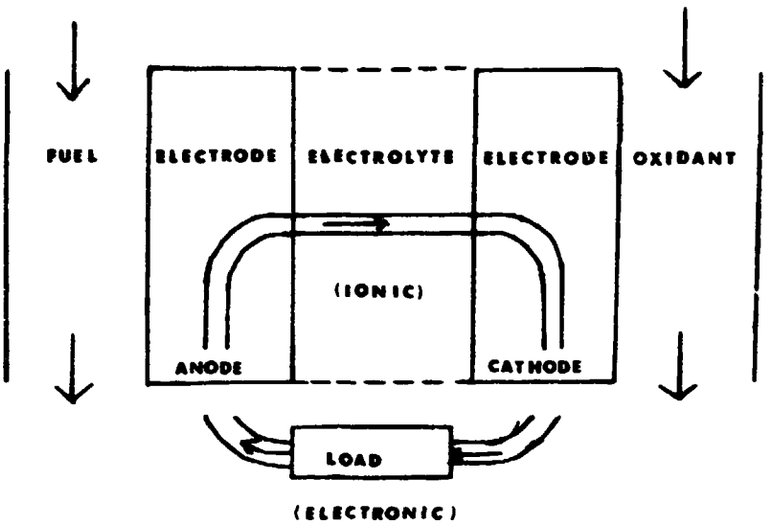

Figure 27.- Fuel cell schematic.

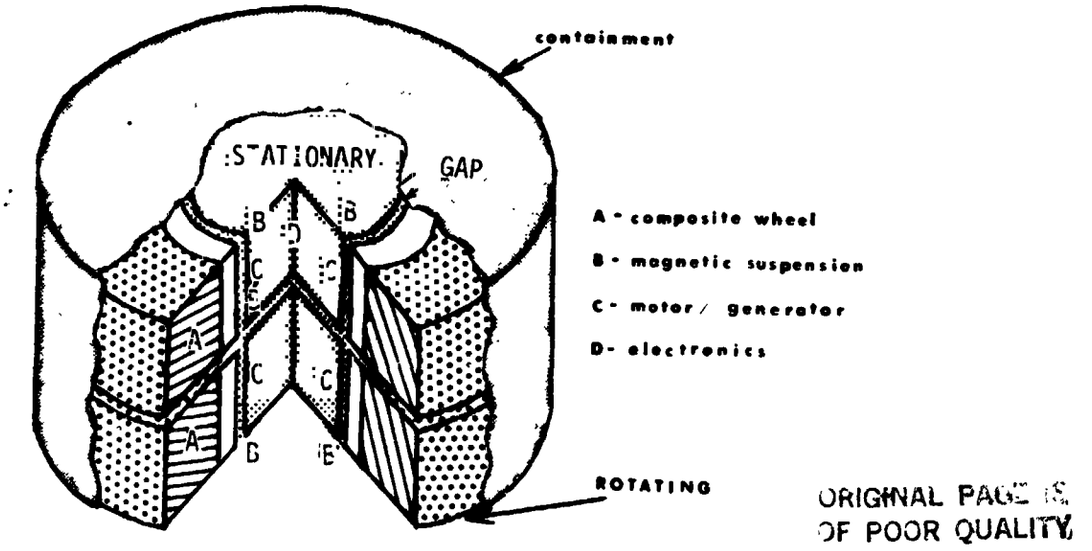

Figure 28.- Flywheel design.

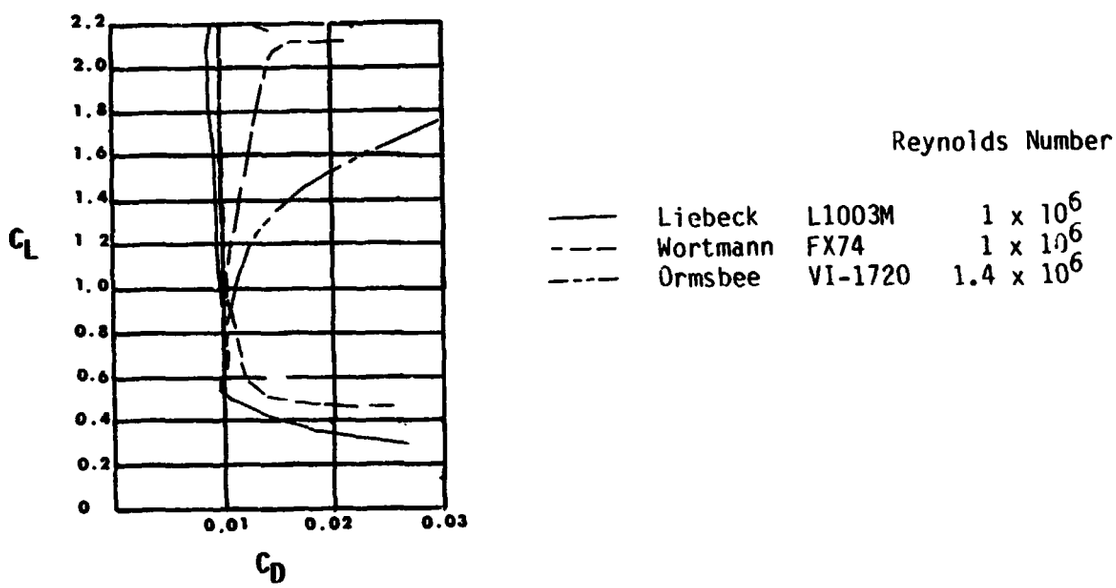

Figure 29.- Experimentally determined lift-drag polars for several high-lift airfoils.

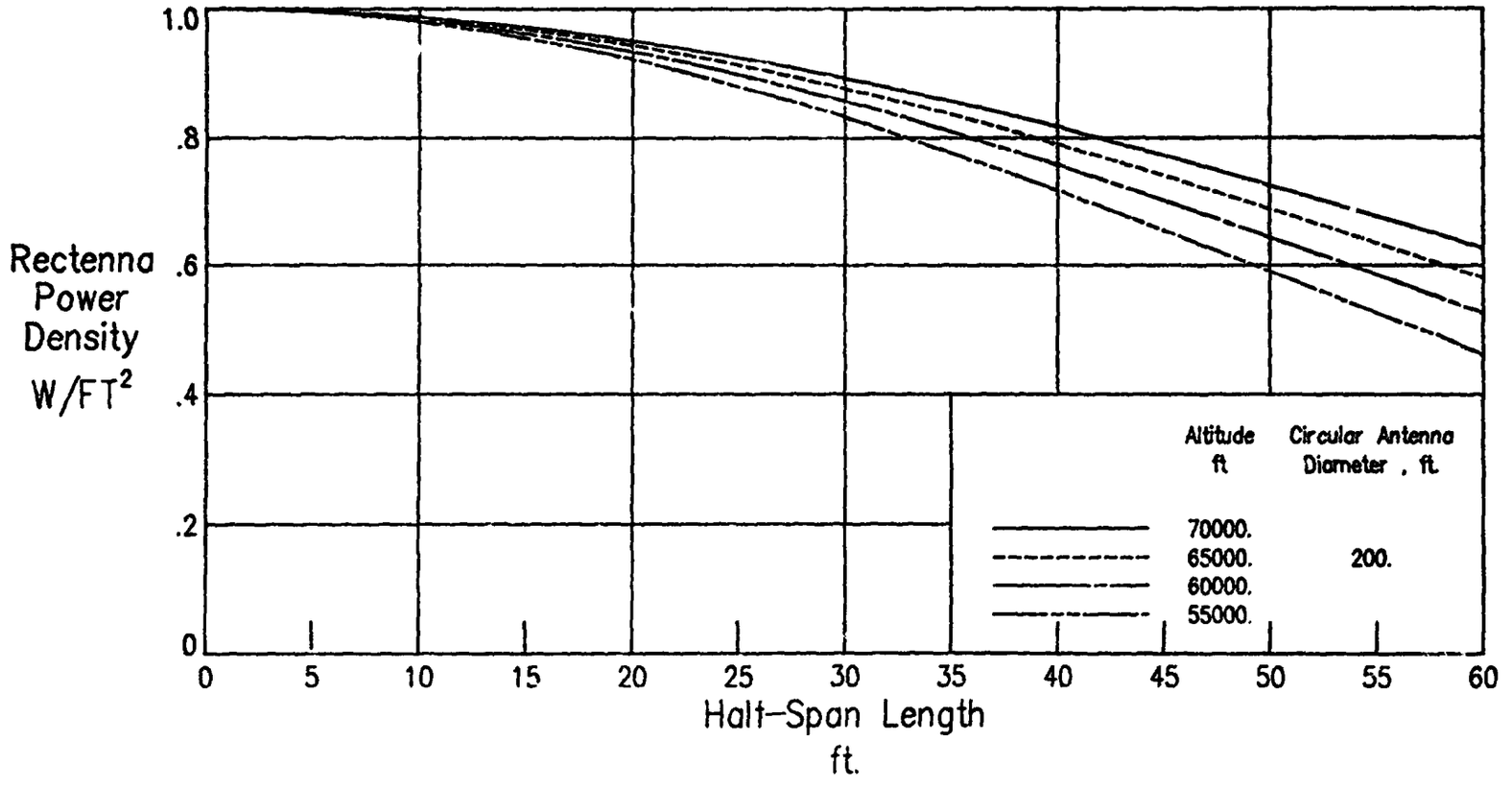

Figure 30.- Spanwise variations of power density for a particular antenna diameter.

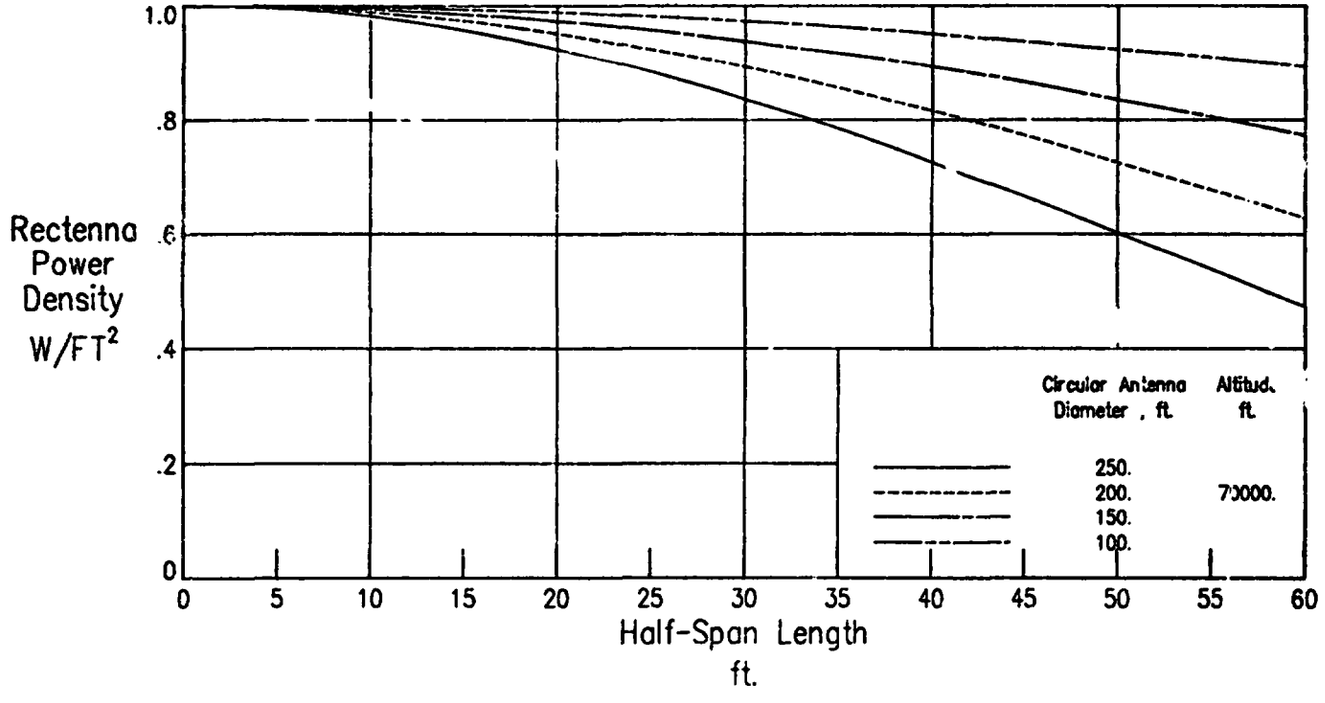

Figure 31.- Spanwise variations of power density for different antenna diameters.

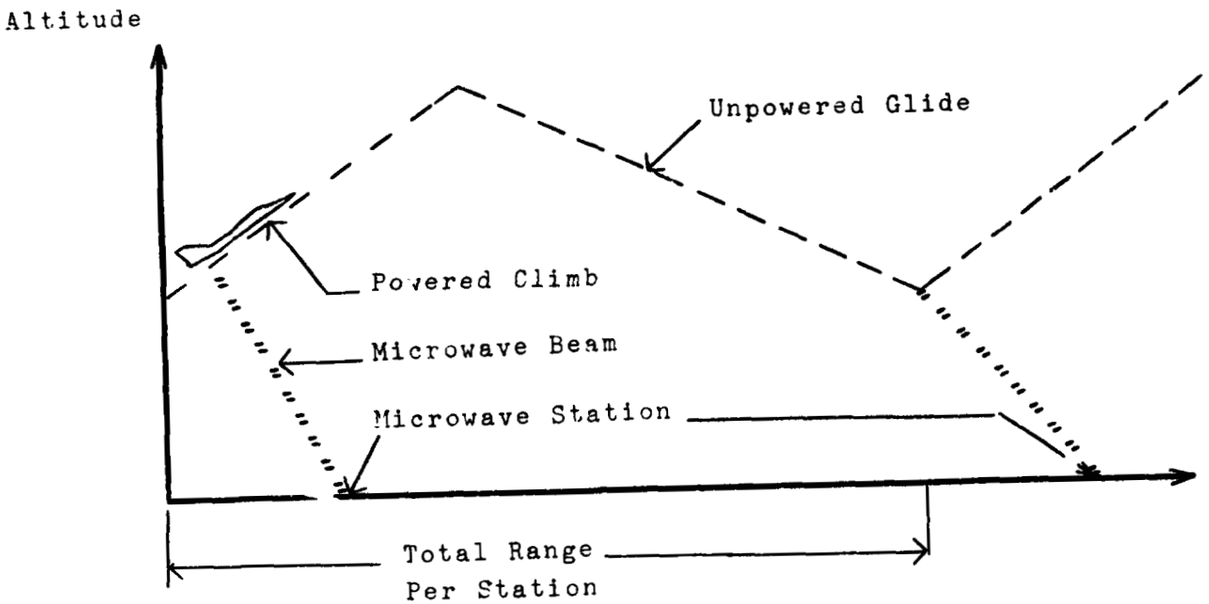

Figure 32.- Boost-glide mode of operation

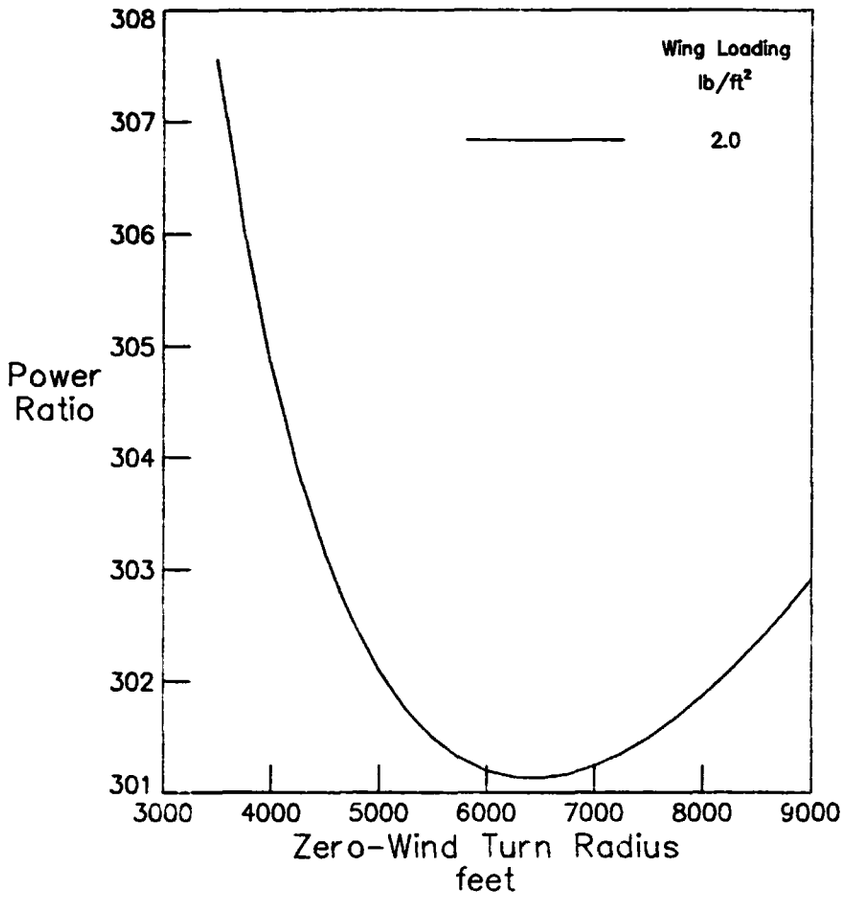

Figure 33a.- Power ratio as a function of the turn radius for a specific value of the wing loading .

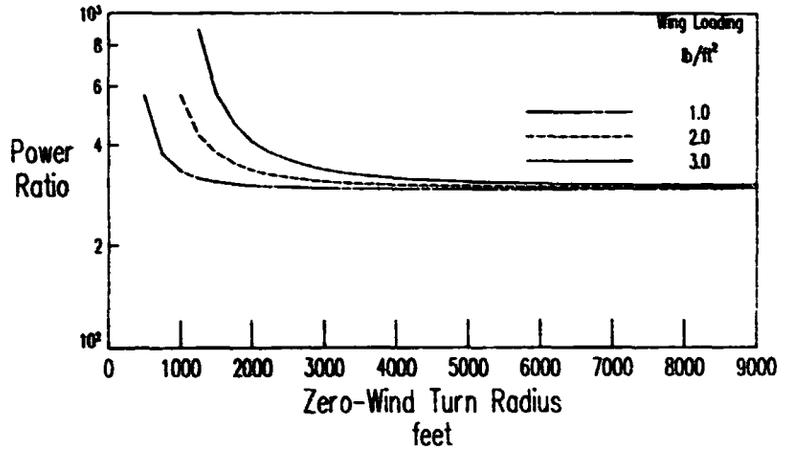

Figure 33b.- Power ratio vs. turn radius for several values of the wing loading .

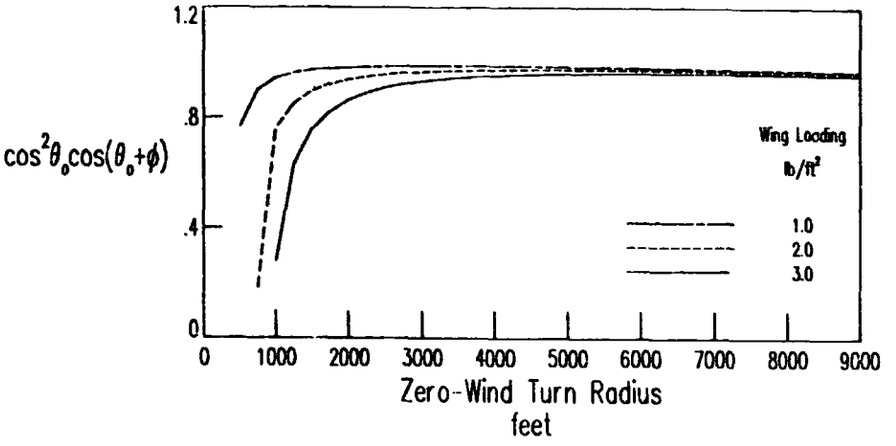

Figure 34.- Effect of turn radius on available power.

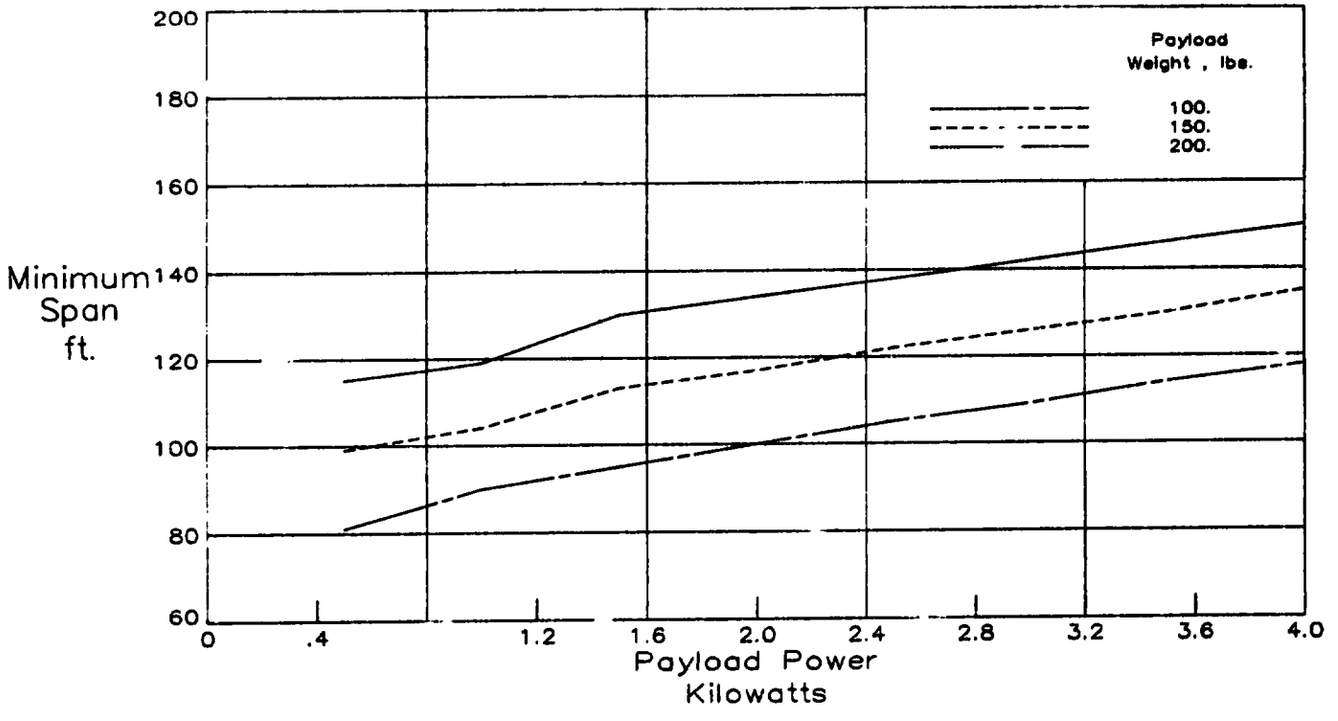

Figure 35.- Predicted span length in zero-wind, continuously powered flight.

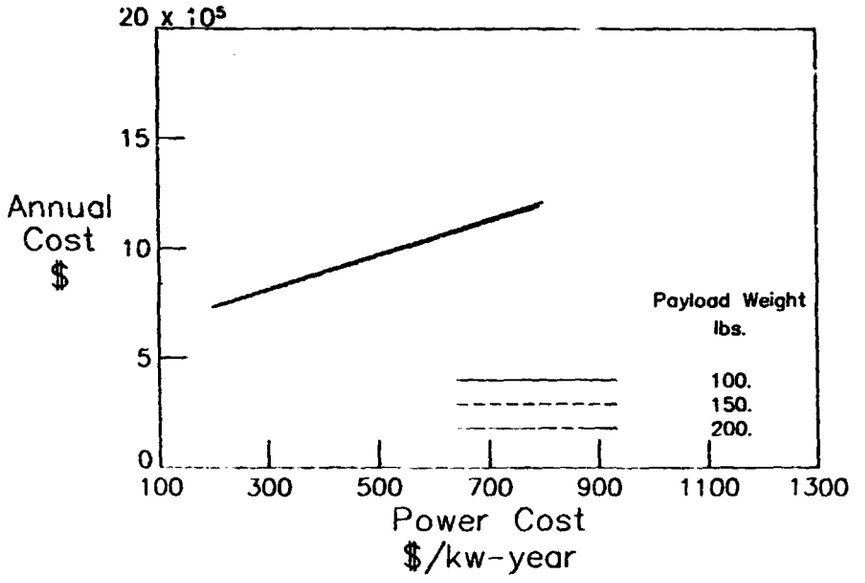

Figure 36.- Effect of variation of power cost on annual cost.

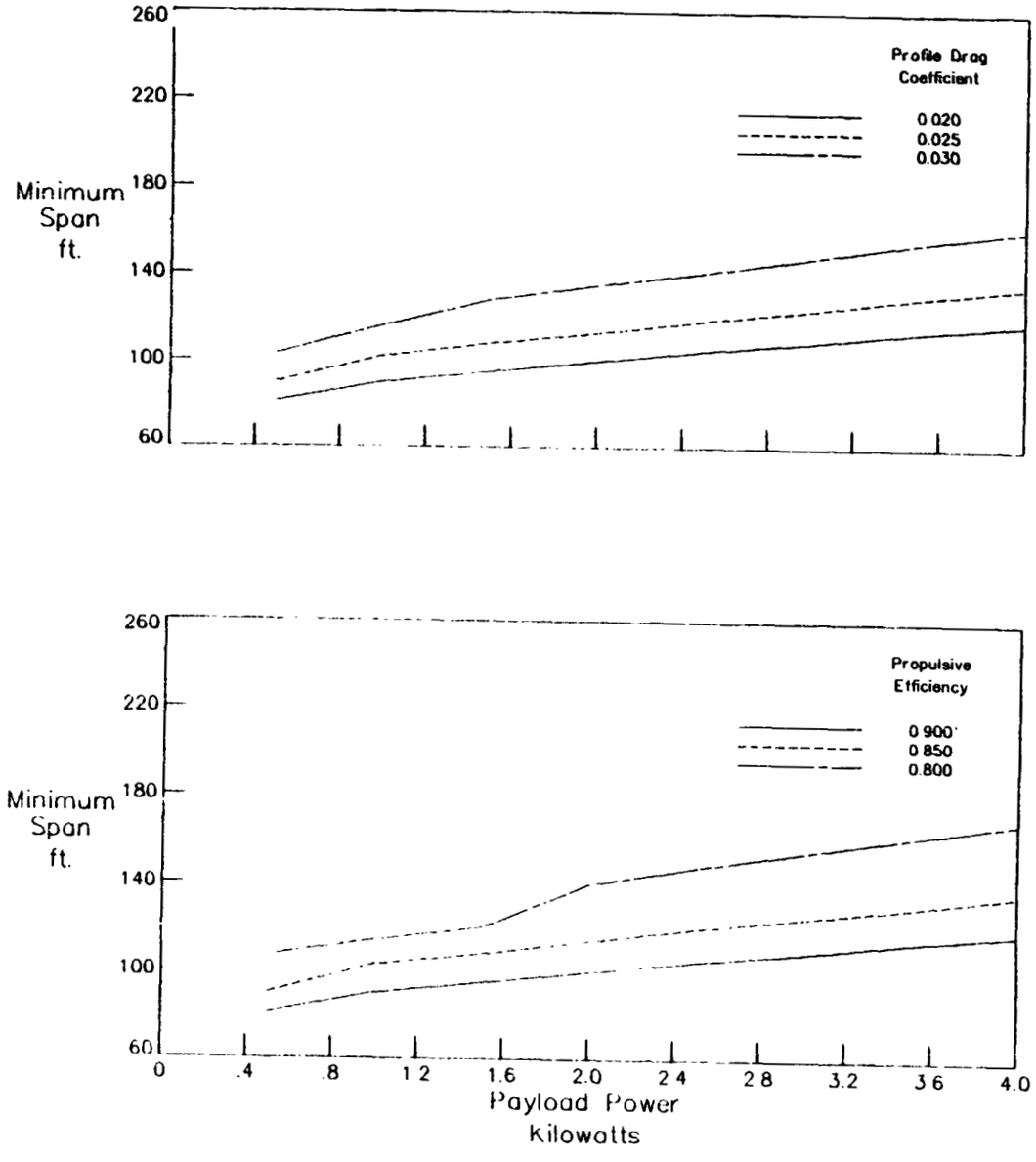

Figure 37.- Effects of profile drag coefficient and propulsive efficiency on vehicle size.

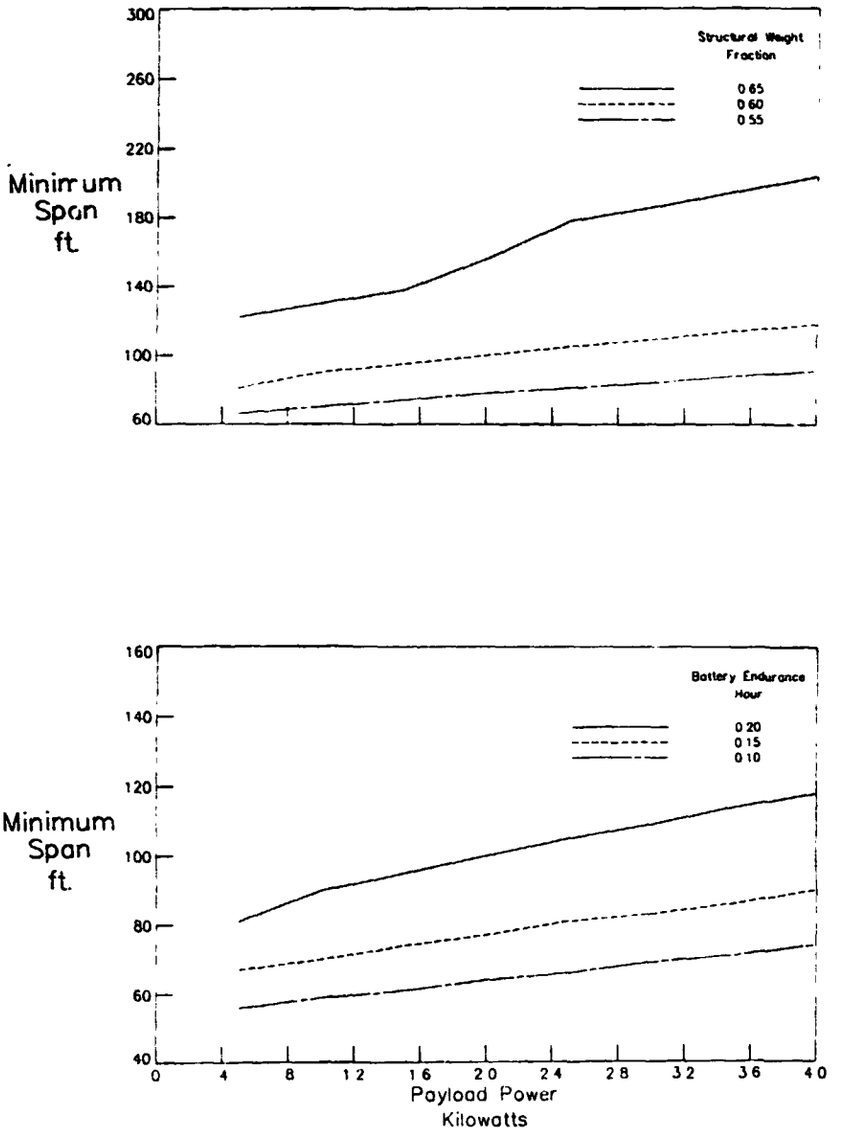

Figure 38.-Effects of lowering the battery endurance and the structural weight fraction on the vehicle size .

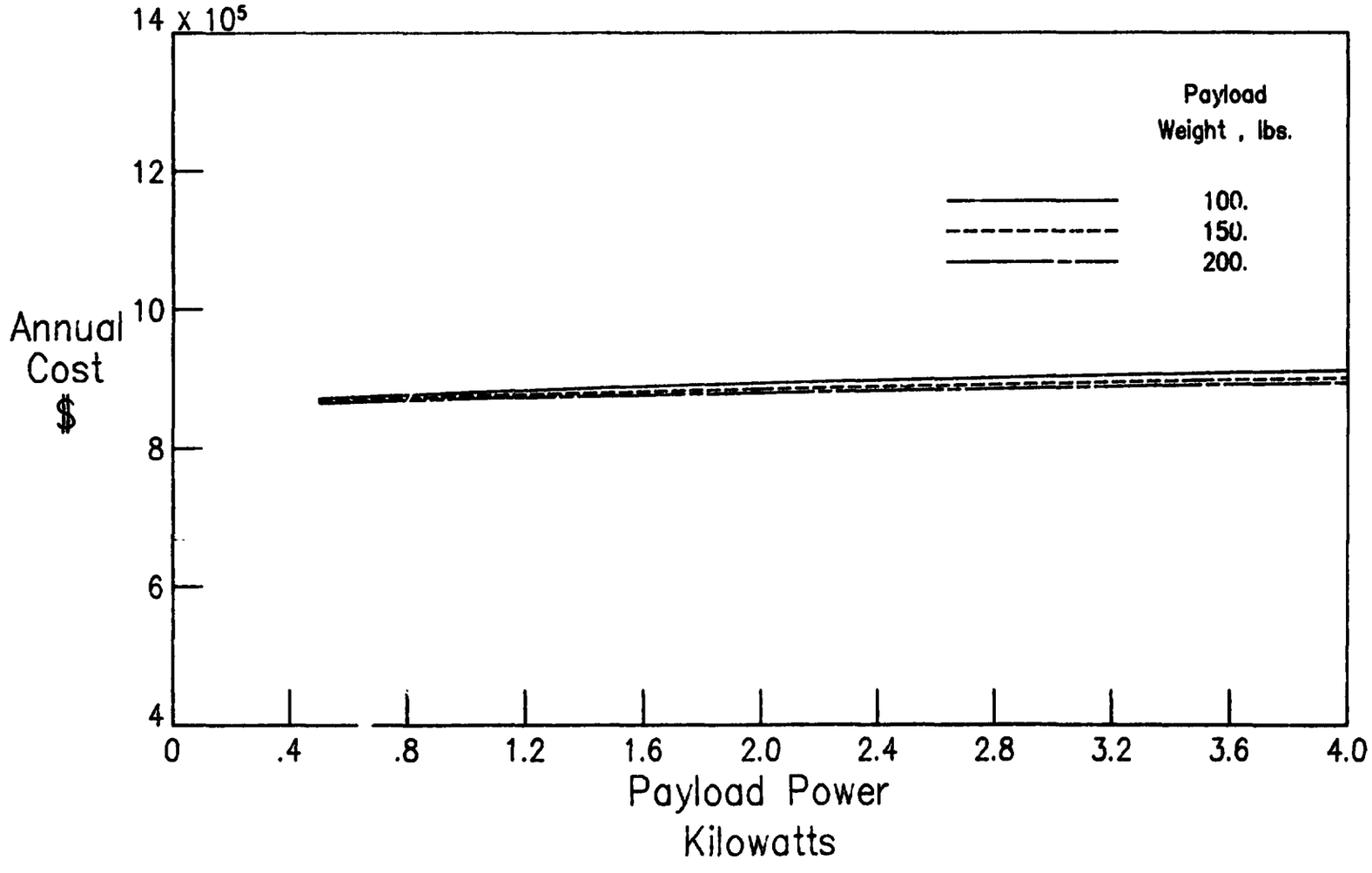

Figure 39.- Effects of payload power and payload weight on annual cost .

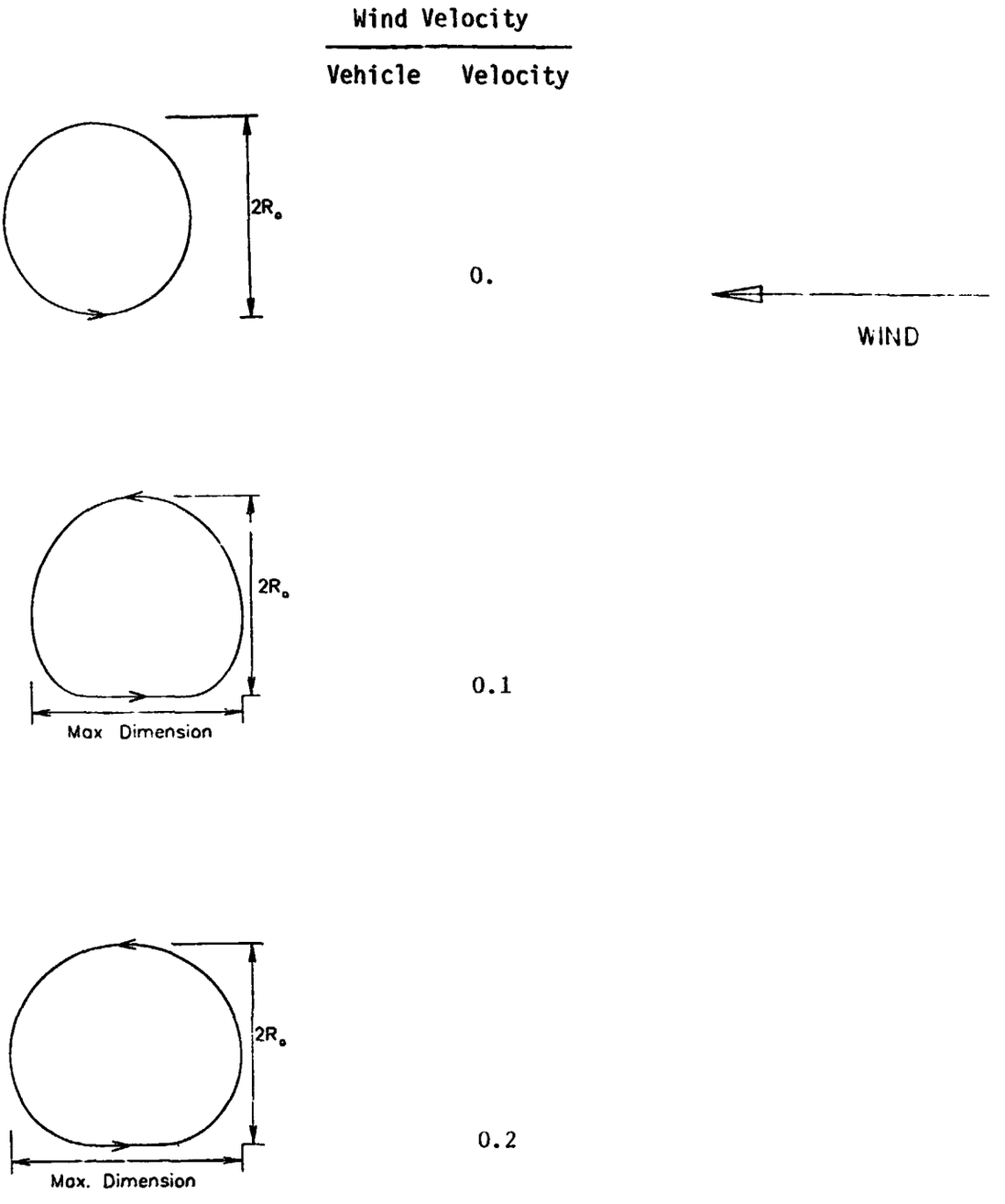

Figure 40.- Maximum dimensions of D-shaped ground tracks with increasing wind speeds .

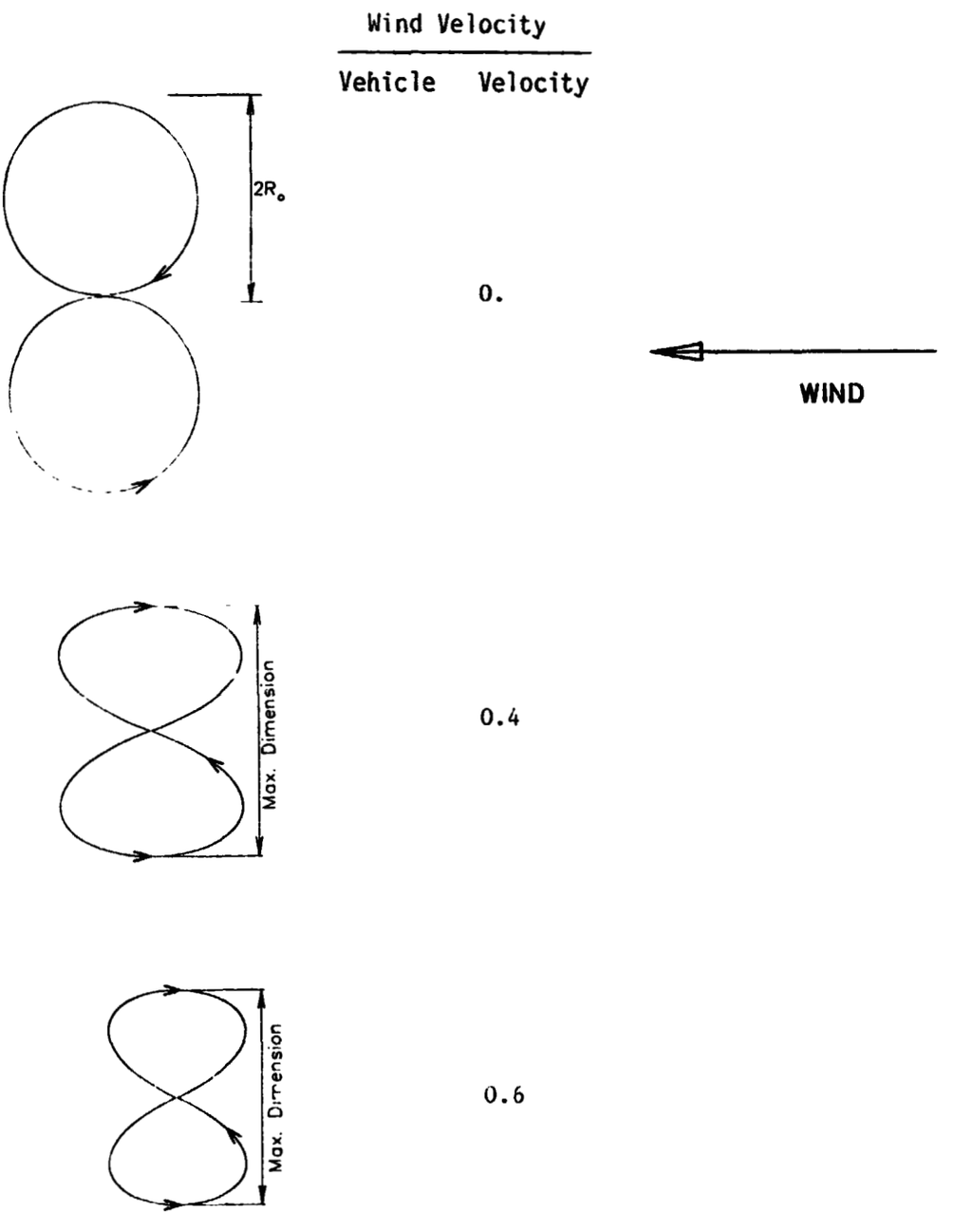

Figure 41.- Maximum dimensions of "Figure-8" ground tracks with increasing wind speed .

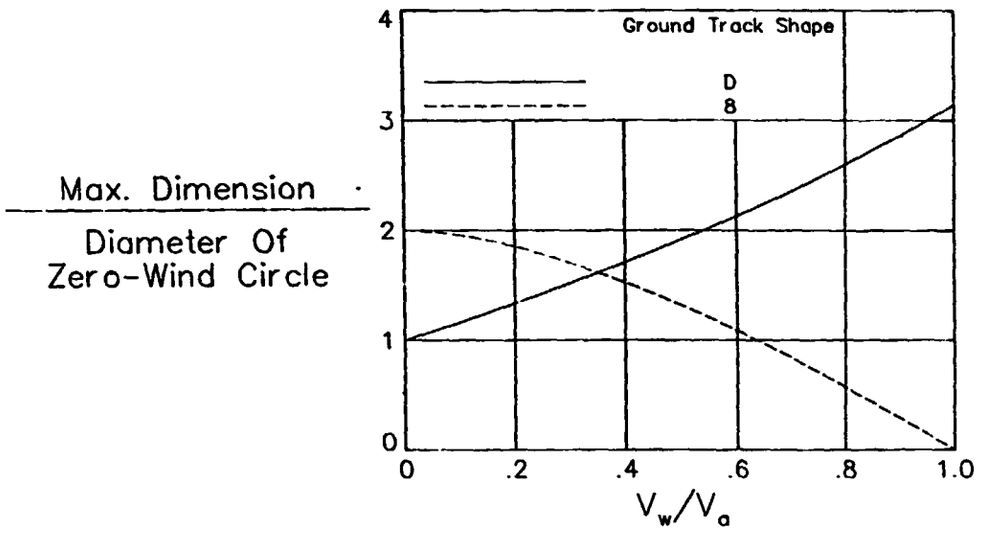

Figure 42.- Ground track sizes for different wind speeds.

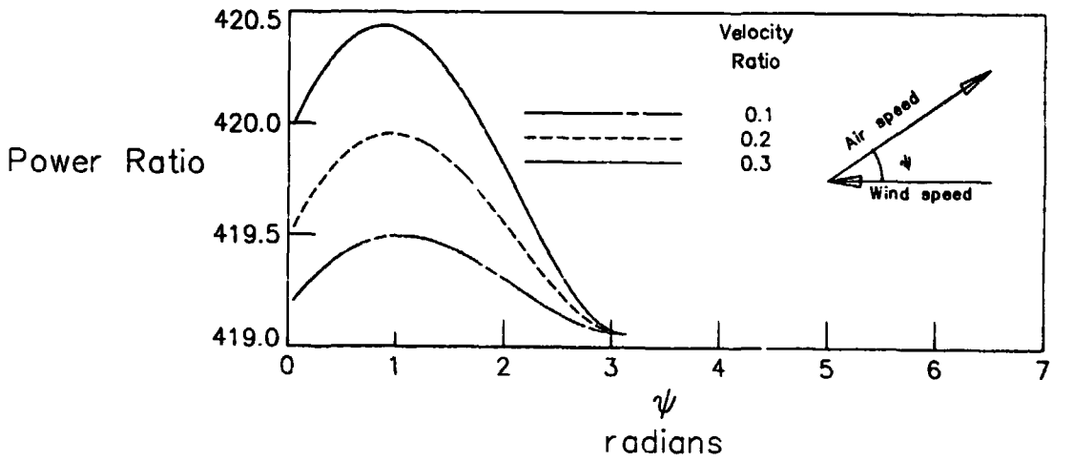

Figure 43.- Variations of the power ratio with one-half of the D-track traveled(fixed wind direction) .

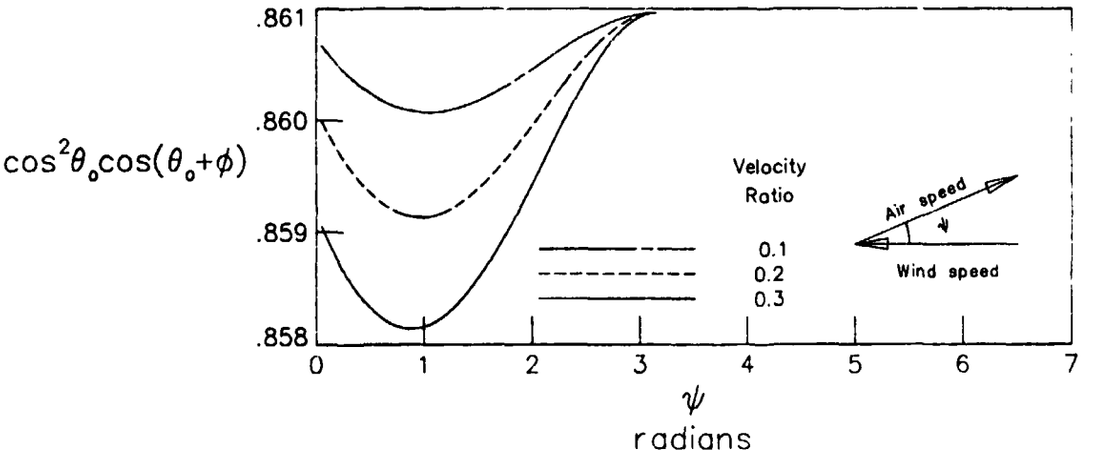

Figure 44.- Variations of the available power (one-half of the D-track traveled) .

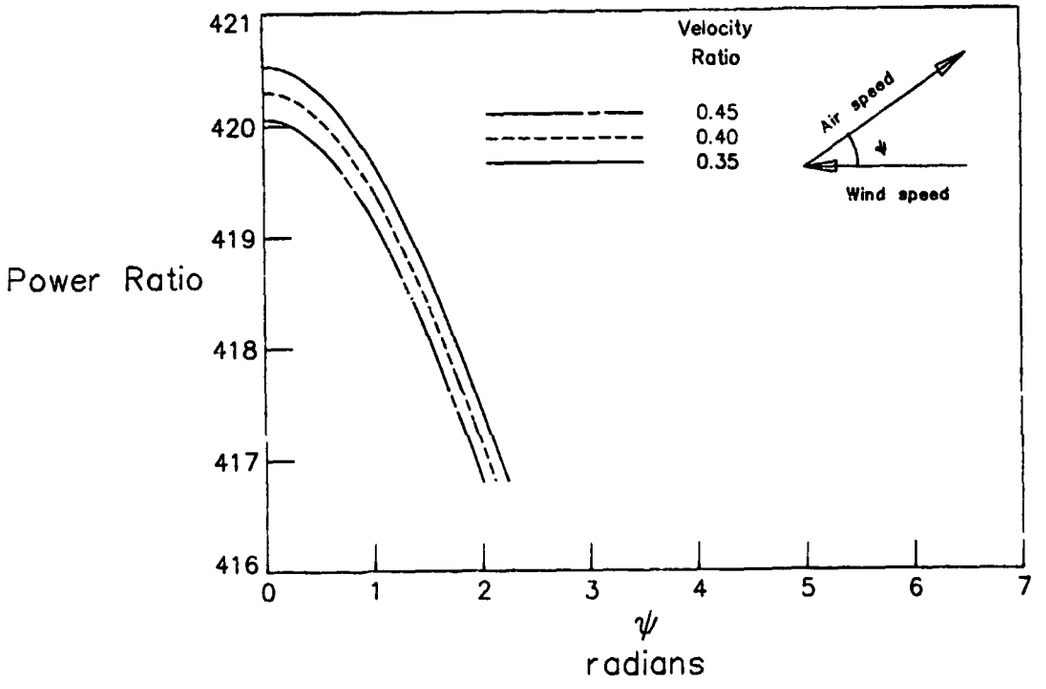

Figure 45.- Variations of the power ratio with one-fourth of the Figure-8 track traveled (fixed wind direction) .

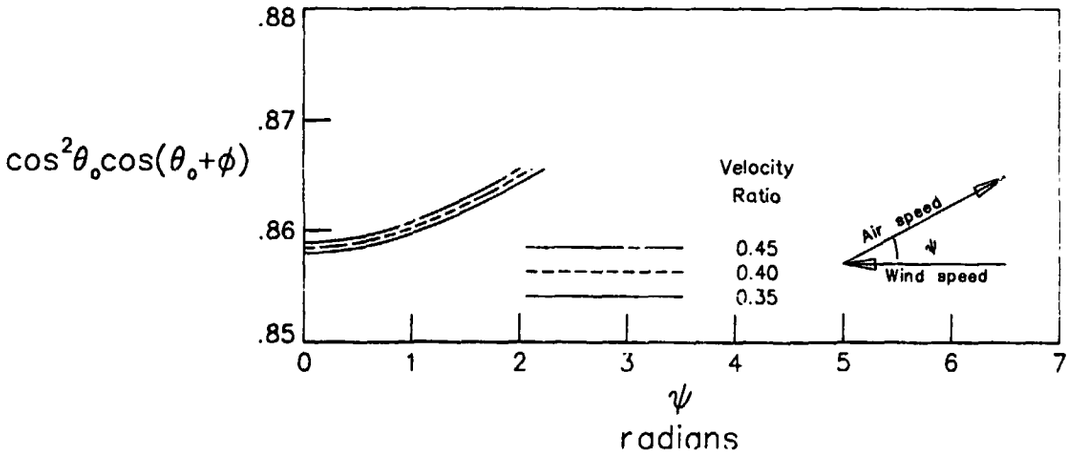

Figure 46.- Variations of the available power with one-fourth of the Figure-8 track traveled .

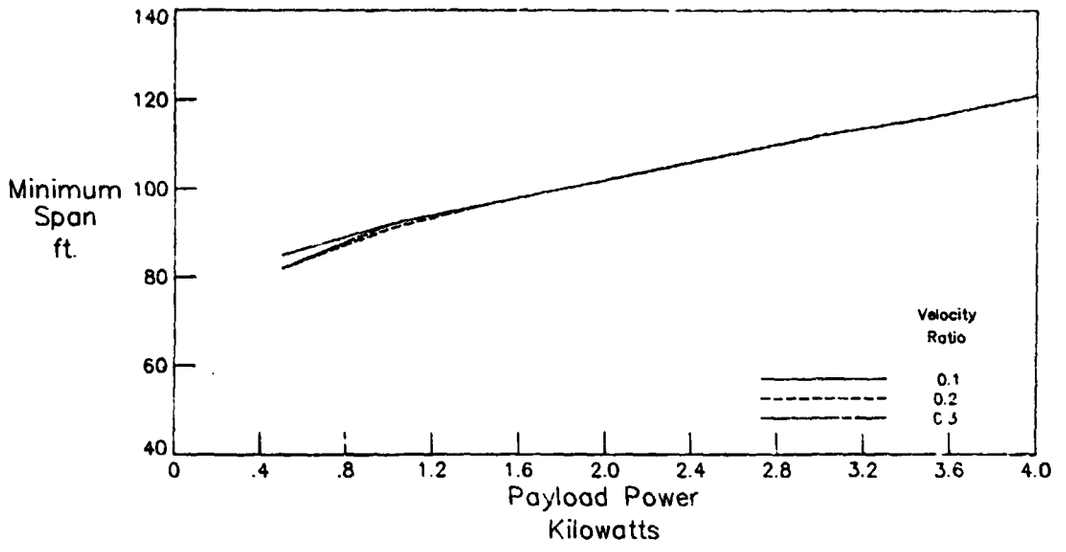

Figure 47.- Predicted span length for a 100-pound payload weight ("D" ground track)

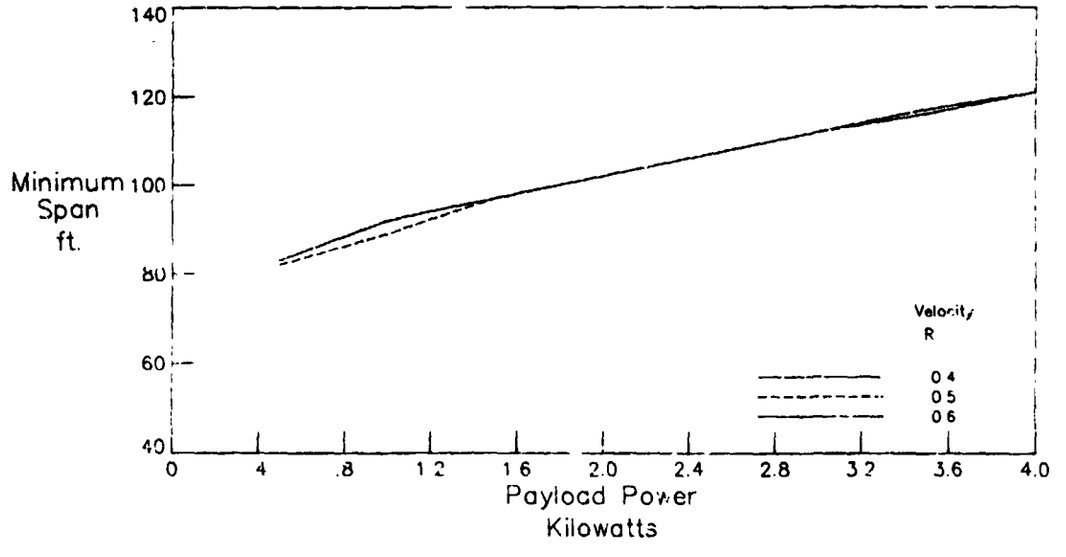

Figure 48.- Predicted span length for a 100-pound payload weight (Figure - 8 track).

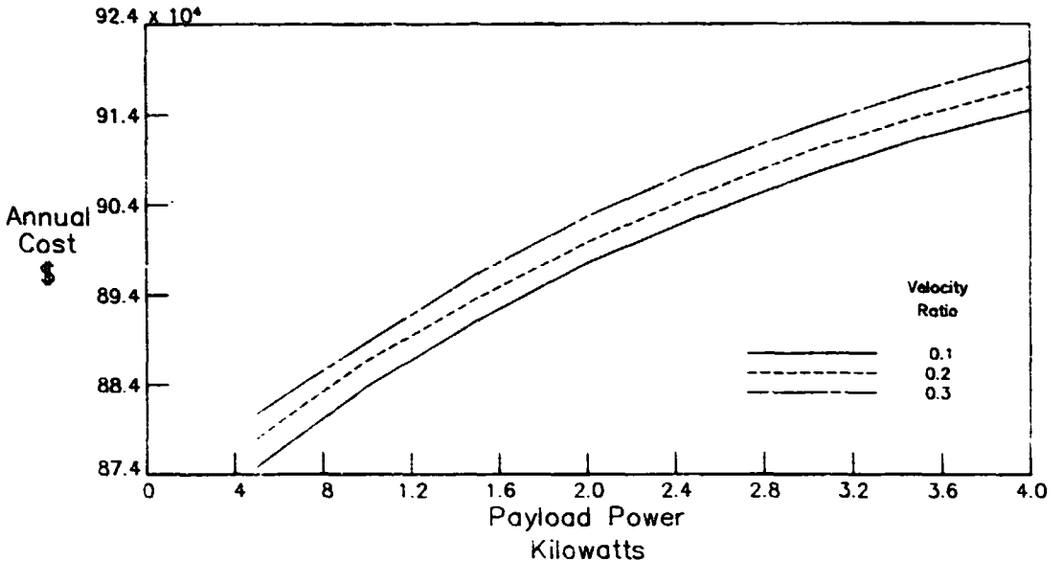

Figure 49.- The cost estimate for a vehicle using a D-shaped track (100-lb payload).

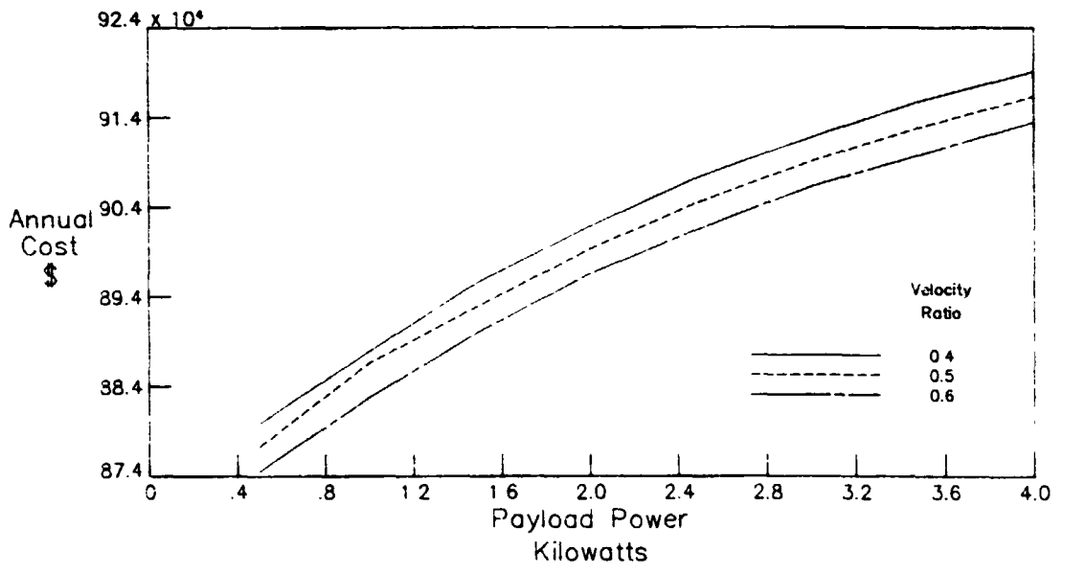

Figure 50.- The cost estimate for a vehicle using a Figure-8 track (100-lb payload).

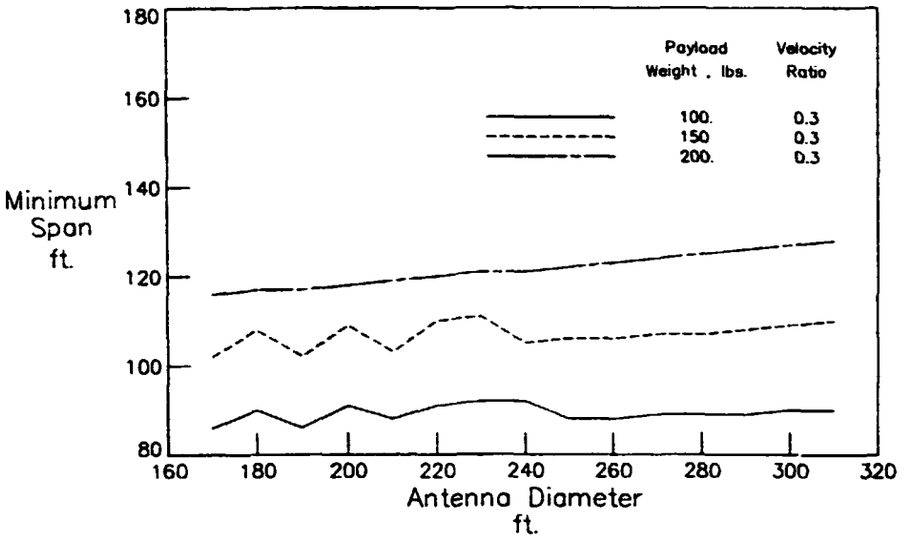

Figure 51.- The vehicle size as a function of the antenna diameter .

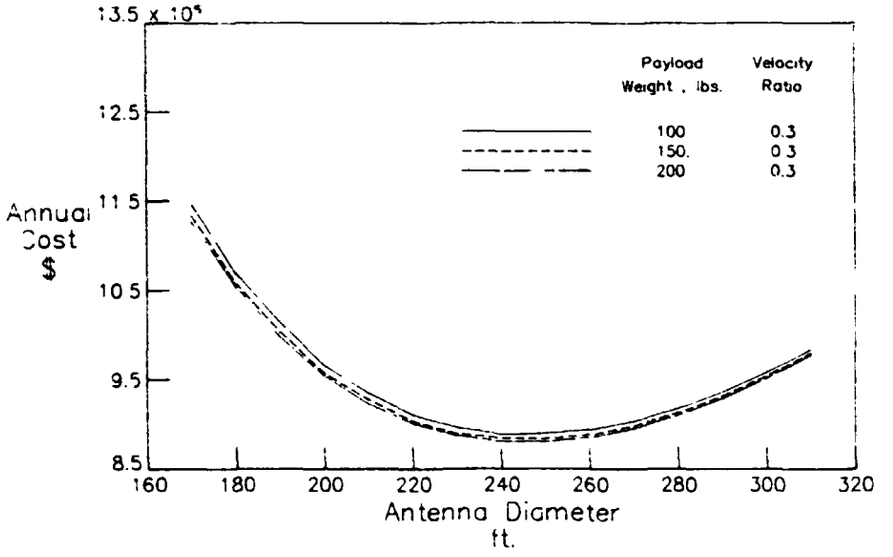

Figure 52.- The cost estimate as a function of the antenna diameter .

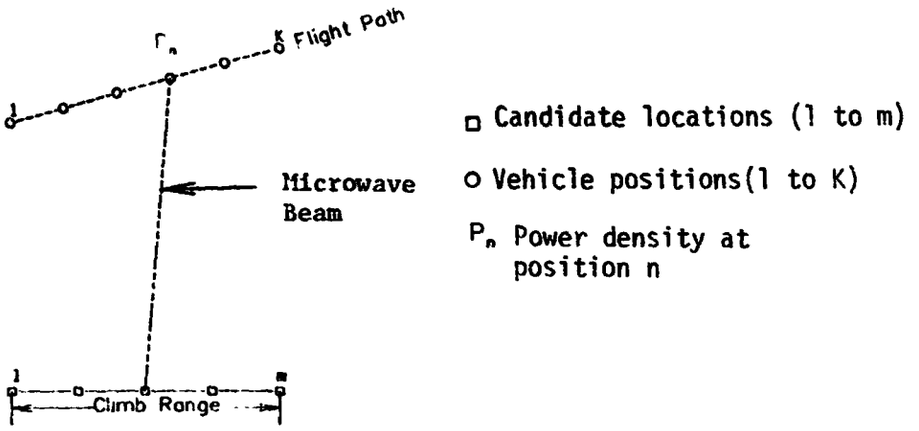

$$\text{Total power density generated by each station location} = \sum_{n=1}^{K} P_n$$

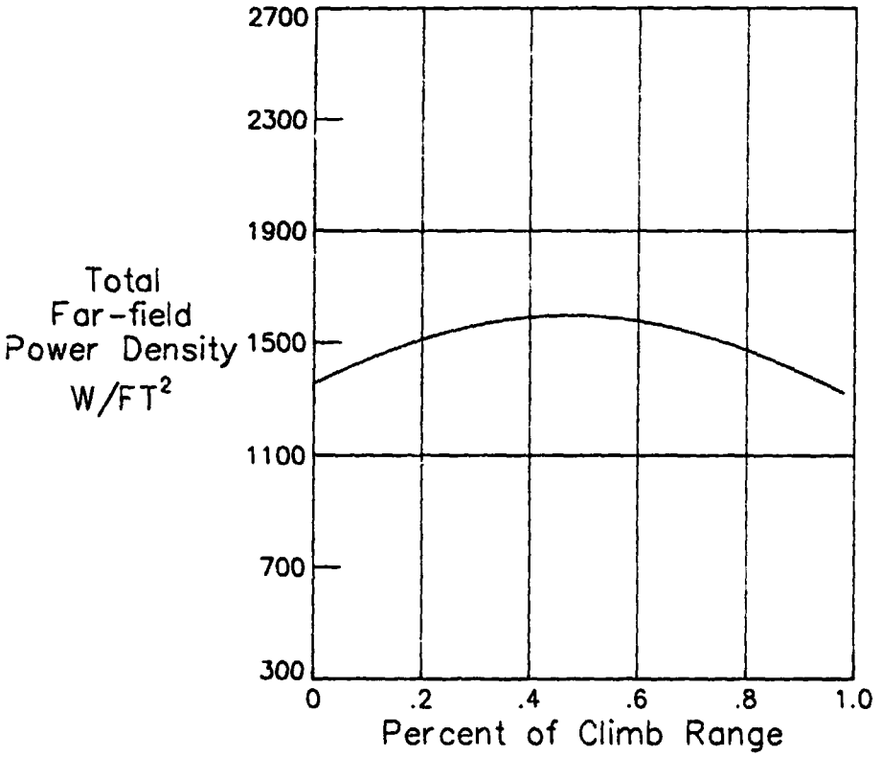

Figure 53.- Sum of power density as a function of the station location

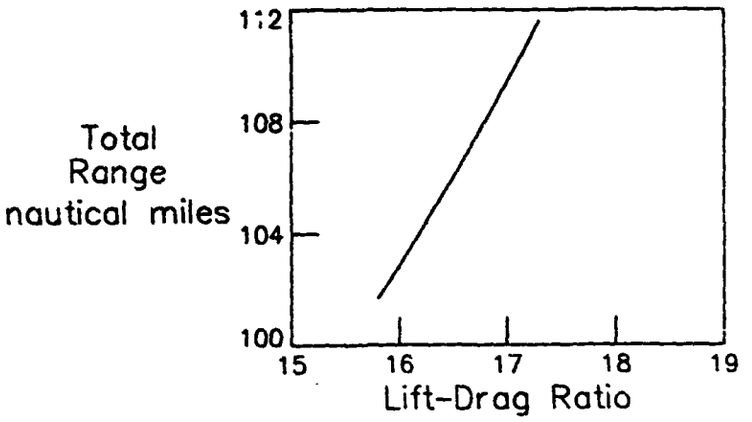

Figure 54.- Total range in zero wind speed.

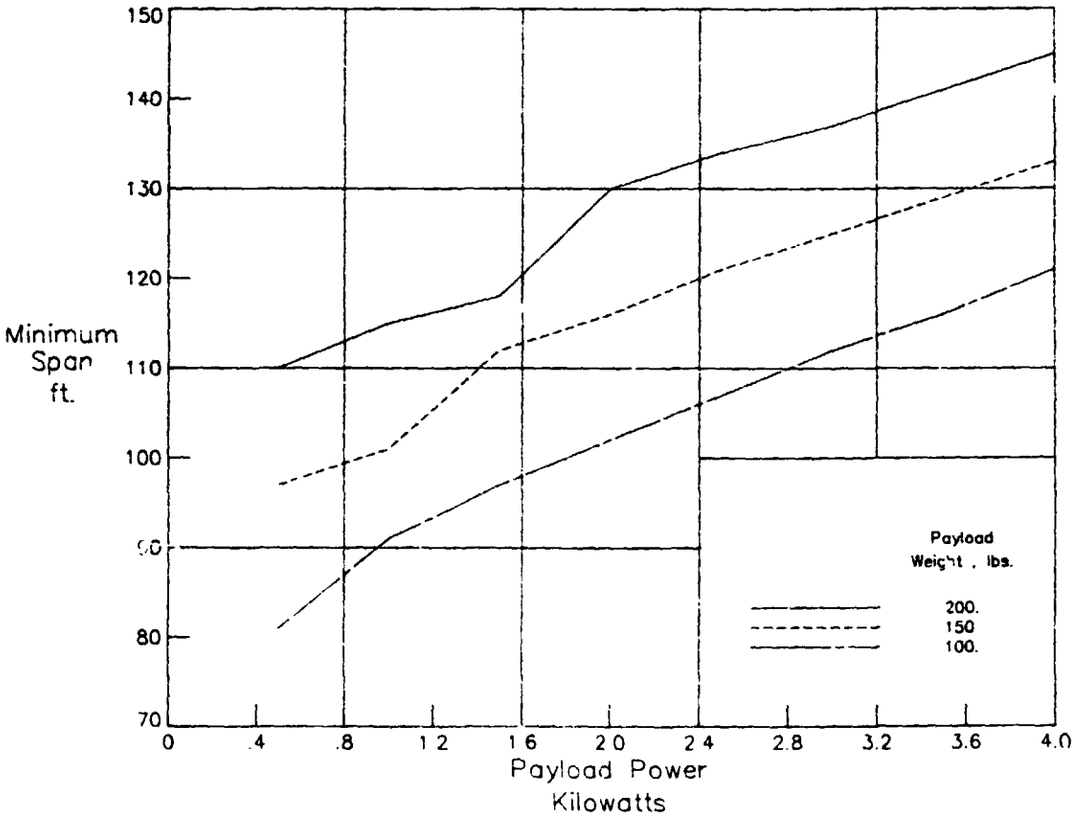

Figure 55.- Vehicle size in zero wind speed.

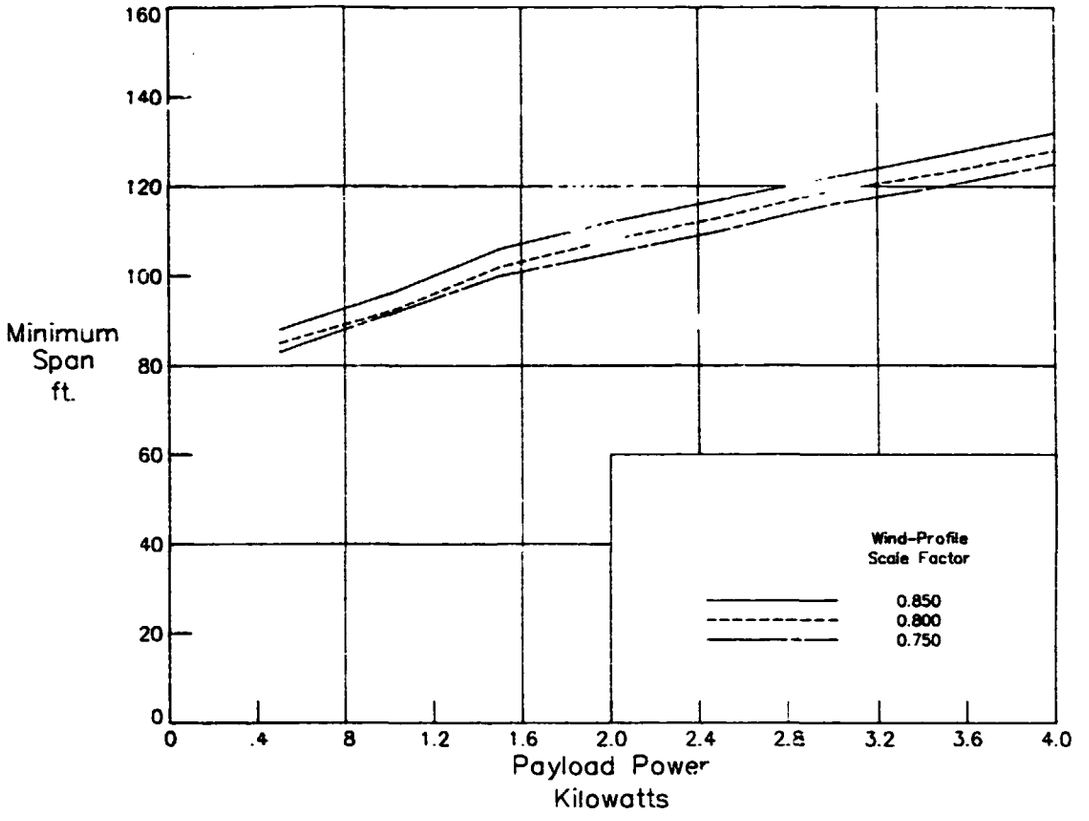

Figure 56.- Effect of wind magnitude on vehicle size.

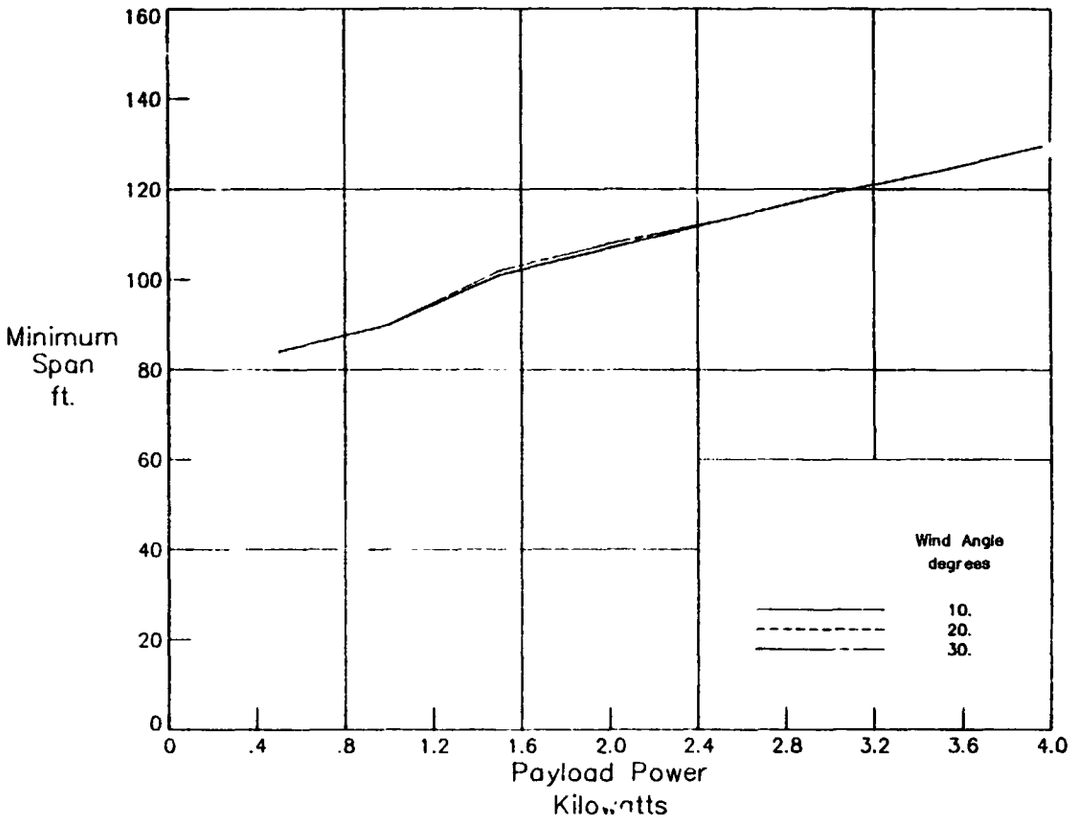

Figure 57.- Effect of wind direction on vehicle size.

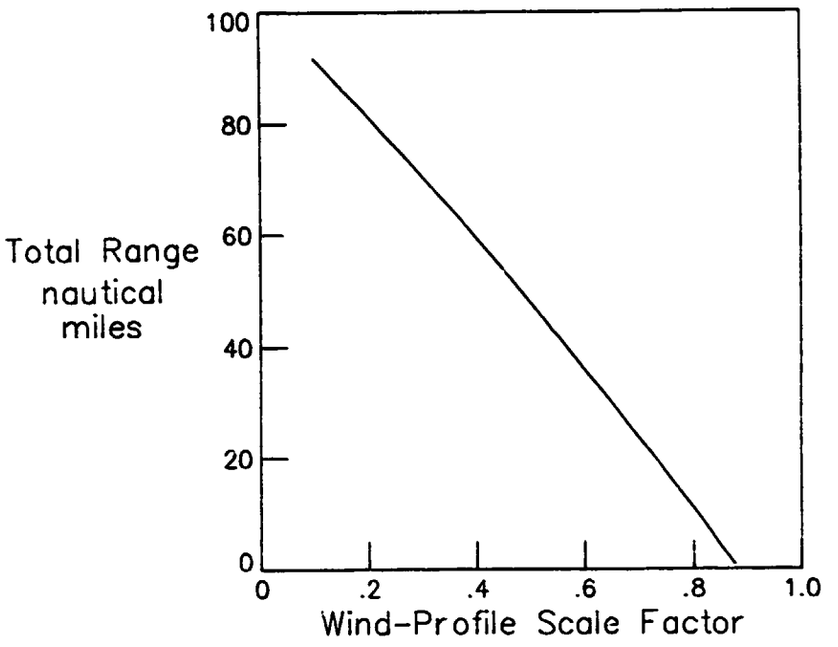

Figure 58.- Range as a function of wind magnitude.

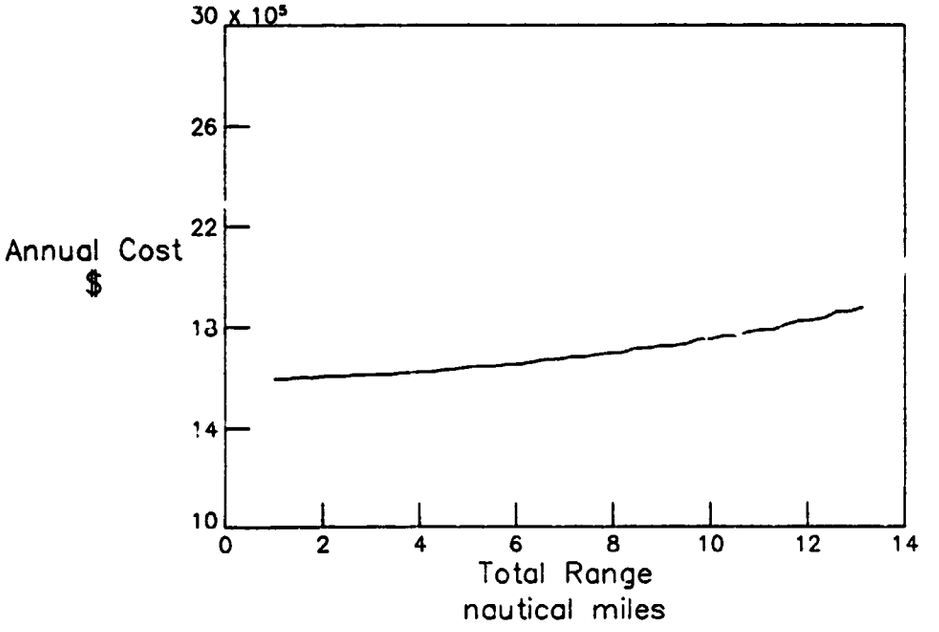

Figure 59.- Cost variation with total range.

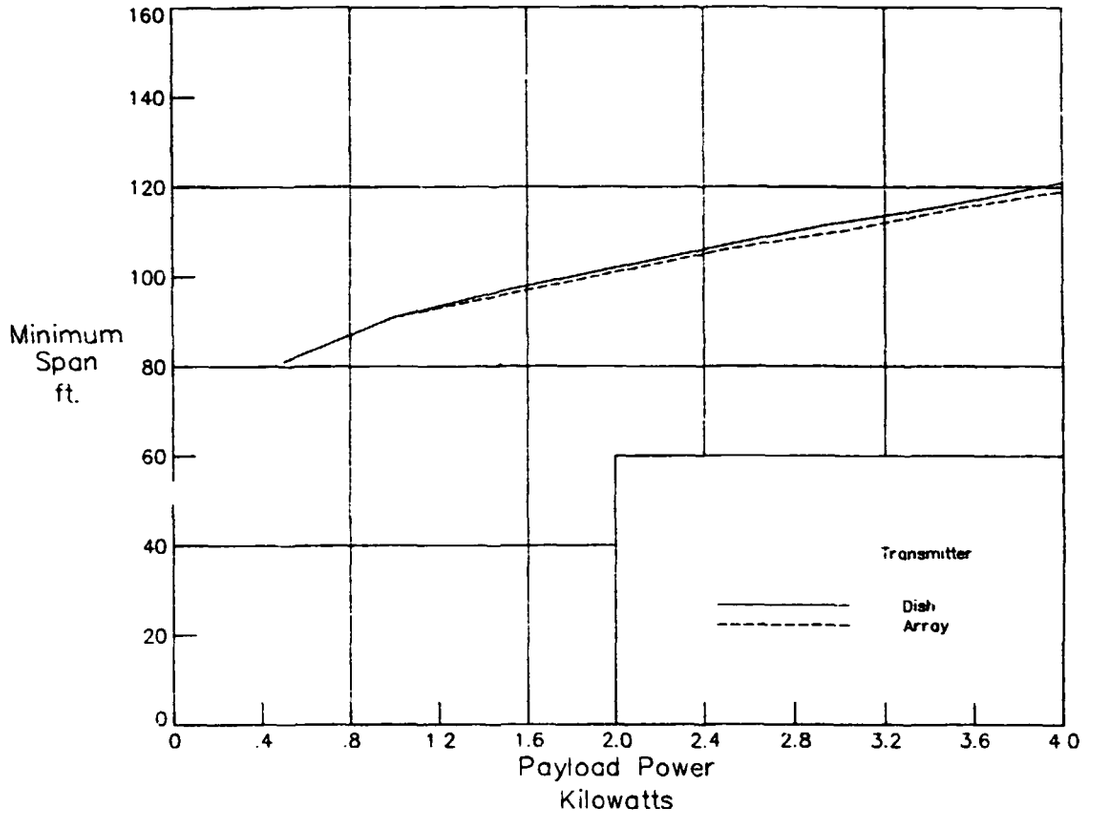

Figure 60.- Zero-wind vehicle size comparison for a 1-KW, 100-lb payload. Boost-glide and continuously powered modes use dish and array transmitters, respectively.

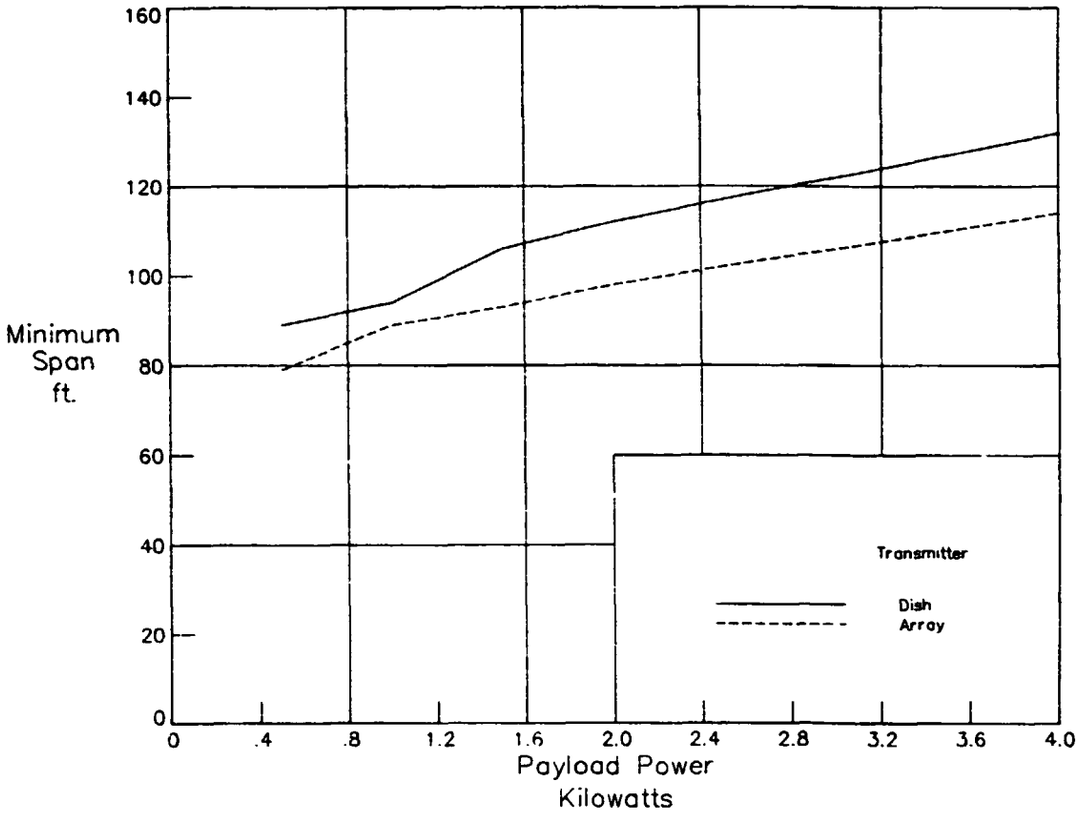

Figure 61.- Vehicle size comparison for a 1-KW, 100-lb payload (wind speed of 167 ft/sec). Boost-glide and continuously powered modes use dish and array transmitters, respectively.

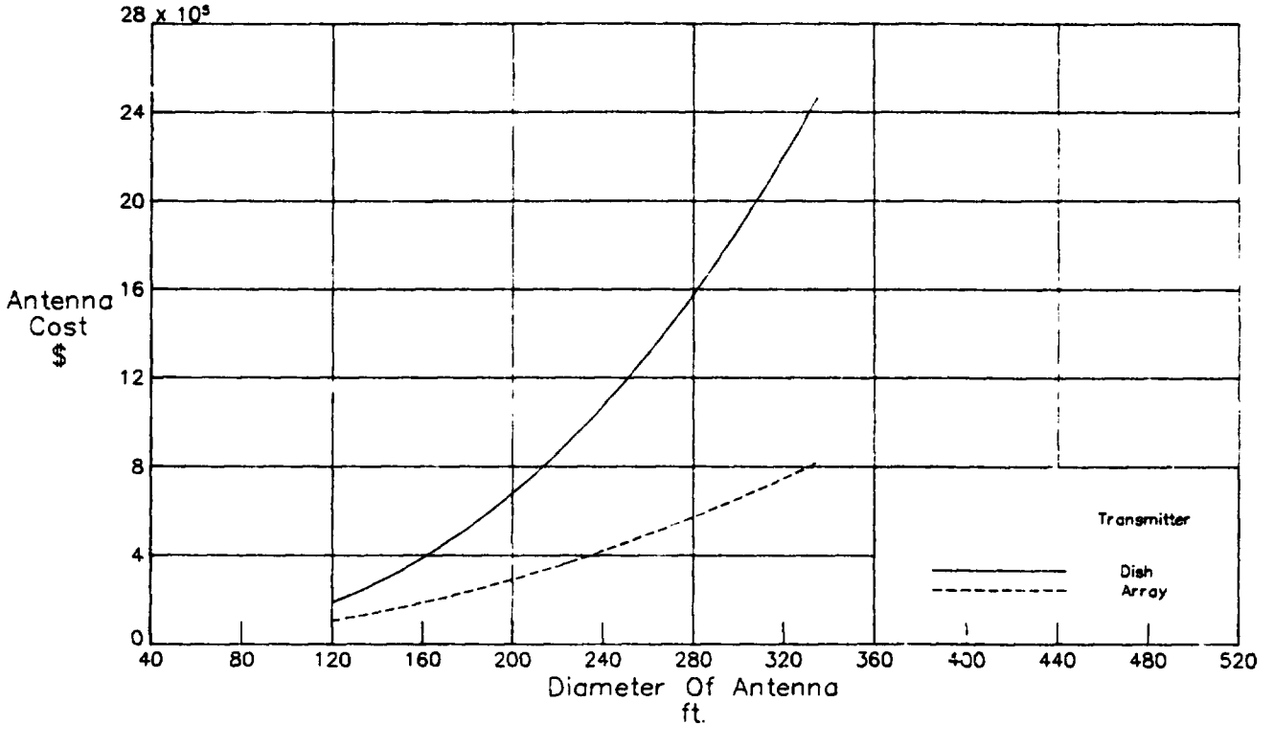

Figure 62.- Comparison of dish and array antenna cost.

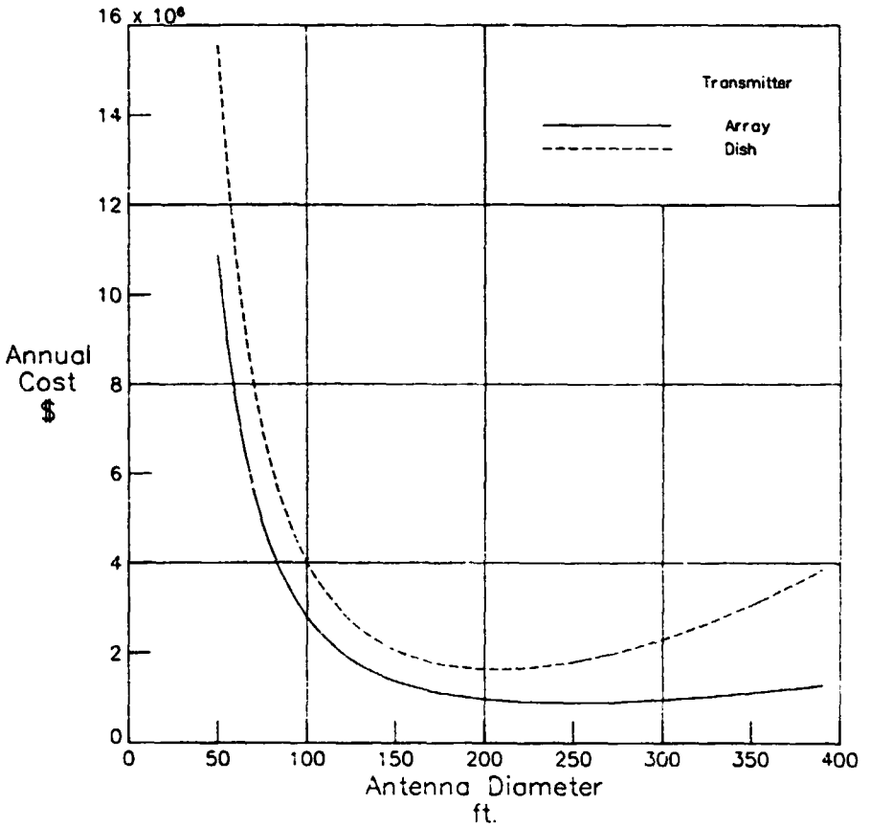

Figure 63.- Comparison of annual costs for dish and array transmitters. Boost-glide and continuously powered modes use dish and array transmitters, respectively.